Western█Graduate&PostdoctoralStudies

Electronic Thesis and Dissertation Repository

7-7-2022 2:00 PM

White Micas as a tool for tracking pegmatite evolution and its use in Li exploration. A case study of Wekusko Lake, Manitoba, Canada.

David N. Benn, *The University of Western Ontario*

Follow this and additional works at: https://ir.lib.uwo.ca/etd

🌀 Part of the Geochemistry Commons, and the Geology Commons

Recommended Citation

Abstract

The Wekusko Lake pegmatite field is part of the Green Bay Group of pegmatites located near Snow Lake, Manitoba, Canada. Within this field, there are at least 13 spodumene-bearing pegmatites of varying degrees of mineralization. The abundance of white micas and the chemical affinity to incorporate Li and other trace elements into its crystalline structure makes white micas an ideal indicator mineral. The evolution of a melt can be tracked using trace elements in white mica. The K/Rb ratio vs Cs is used to determine a link between increasing melt evolution and increased Li contents of both the white mica and the pegmatite. White mica compositions were examined using portable Raman and LIBS to evaluate whether Li contents can be determined in the field. The LIBS was able to identify the pegmatites dikes with the highest Li contents, which can be applied to real-time decision-making during exploration.

Keywords

Summary for Lay Audience

The Wekusko Lake pegmatite field is part of the Green Bay Group of pegmatites located near Snow Lake, Manitoba, Canada. Pegmatites are a key source for Li and rare metals (e.g., Sn, Cs, Ta, Nb), which are become increasingly more important in society. Spodumene is the primary mineral from which Li is obtained. The majority of pegmatites are barren and contain little Li. Distinguishing between Li-rich and Li-poor pegmatites can be challenging in the field without laboratory testing if spodumene is not visible.

As a pegmatite melt crystallizes the remaining melt becomes more enriched in rare metals, this process is called evolution. White micas are the third most abundant mineral in pegmatites and are able to incorporate trace elements (e.g., Li, Cs, Rb, Nb, Ta) into their crystal structure, relative to the concentration of those elements in the melt. Using the trace element concentration of the white mica, the evolution and therefore mineralization potential of the pegmatite can be estimated.

Laboratory testing to determine the chemical composition of rock is a time consuming and can bottle neck exploration projects trying to plan the next target. Portable LIBS is able to identify the Li contents of white micas and provide near instantaneous result. The white mica Li contents can be used to plan new targets for exploration.

Acknowledgements

Table of contents

List of Figures

List of Tables

Chapter 1

1 Introduction

The demand for lithium (Li) has led to a surge in exploration for new resources (Jaskula, 2016, 2020). Pegmatites are one of the major sources for Li. The majority of pegmatites are not sufficiently evolved to contain economic concentrations of rare metals such as Li, Cs, Ta, Nb, and Sn (Černý, 1991b), which become concentrated during the evolution of the pegmatitic melt through fractionation. White micas are an abundant mineral throughout the entire body of most pegmatite dikes and white micas incorporate the rare metals that are enriched during fractionation. This makes white micas an ideal mineral for tracking the evolution of pegmatite dikes and potentially white micas can be used in mineral exploration, particularly if the rare metals can be analysed by field portable instruments.

1.1 Lithium Resources

The widespread use of Li-ion batteries in portable electronic devices, electric vehicles and grid storage is largely responsible for a global surge in demand of Li. Li-ion batteries account for 65% of the annual use of Li (Jaskula, 2020). This is an increase from 35% of the annual Li use in 2014 (Jaskula, 2016). Other uses for Li are ceramics and glass (18%), lubricating greases (5%), polymers (3%), air treatment (1%), and others (9%) including pharmaceuticals, and aluminium production (Jaskula, 2020).

Lithium is currently being produced from two primary sources: brines and pegmatites. The largest global Li source is continental brines, which are enclosed basins where inflowing waters contain increased Li contains from weathering or alteration of the surrounding volcanic rocks (Ide and Kunasz, 1989; Kesler et al., 2012; Bowell et al., 2020). These brines have high volumes and low concentration (0.03-0.3 wt% Li) of Li. They also produce large amount of accessory B, K, Na, and Mg (Kavanagh, 2018).

Pegmatites are coarse-grained igneous rocks that have crystallized from highly evolved magmas. Pegmatites are common worldwide. However, fertile, Li-rich (rare metal) pegmatites are rare. It is estimated that rare metal pegmatites represent less than 2% of pegmatites worldwide (Černý, 1991b). Spodumene ($LiAlSi_2O_6$) is the most common Li-aluminosilicate mineral in pegmatites, followed by petalite ($LiAlSi_4O_{10}$) as well as less common Li minerals (Grew, 2020). The average ore grade for producing Li pegmatites is 1.4 wt% Li_2O (Evans, 2014) and fertile pegmatites commonly contain Be-, Cs-, F-, P-, Sn-, Ta- and/or Rb-bearing minerals (Kavanagh, 2018).

The worldwide Li resource is estimated to be 80Mt (Jaskula, 2020). Due to continuous exploration for Li the global resource has nearly doubled in the past decade (Evans 2014; Jaskula, 2020). Continental brines account for nearly 70% of the world Li resource, but only 30% of the global Li production. In contrast, pegmatites account for 25% of the worldwide Li resource and 70% of the global production (Jaskula, 2020). Other sources of Li are Li-rich clays, geothermal brines, and oilfield brines (Evans, 2014).

The global Li resource is as follows: Boliva 21Mt, Argentina 17Mt, Chile 9Mt, United States 6.7Mt, Australia 6.3Mt, China 4.5Mt, Congo 3Mt, Germany 2.5Mt, Canada/Mexico 1.7Mt, Czechia 1.3Mt, Mali/ Russia/ Serbia 1Mt, Zimbabwe 540kt, Brazil 400kt, Spain 300kt, Portugal 250kt, Peru 130kt, Austria/ Finland/ Kazakhstan 50kt, Namibia 9kt (Jaskula, 2020). The brine-based Li sources are from Argentina, Bolivia, Chile, China, and the United States, whereas the pegmatite-hosted sources are from Australia, Austria, Brazil, Canada, China, Congo, Czechia, Finland, Germany, Mali, Namibia, Portugal, Spain, and Zimbabwe (Jaskula, 2020). Currently the majority of production comes from Australia, Argentina, Chile and China. Overproduction in 2018 and decreased prices has caused many producing Li operations to postpone expansion plans and caused smaller projects to stop production (Jaskula, 2020). However, lithium exploration (in 2022) is currently extremely active in Canada and internationally.

Currently less than 1% of lithium is recycled (Kavanagh, 2018). It is possible to recover Li from Li-ion batteries because of its low melting point (180°C) and low solubility in fluoride, carbonate, and phosphate salt forms (Tarascon 2010; Kavanagh, 2018). Lithium

recycling will likely require a well-established electric vehicle market to become feasible (Martin et al., 2017; Kavanagh, 2018).

1.2 Pegmatites

Pegmatites are coarse-grained and are characterized by much greater textural variation compared to more common igneous rocks such as granite (London, 2008). Pegmatites have highly evolved compositions (enriched in incompatible elements) created by either extreme fractional crystallization or low degrees of partial melting (anatexis). Pegmatitic melts have a high viscosity which impedes the ionic diffusion necessary for the crystal nucleation and contain high concentrations of incompatible and fluxing elements (Cameron et al., 1949; London and Morgan, 2012). This results in a high degree of supersaturation in mineral components when crystallization does begin (London, 2018). As quartz and feldspar crystallize the melt becomes more enriched in incompatible melts (Ta, Nb), rare alkalis (Li, Cs, Rb) and fluxes such as B, F, Li, P and H_2O which lower the granite melt solidus, reduce the viscosity and increase the ionic diffusivity (Dingwell et al., 1996; Bartels et al., 2011).

Pegmatites commonly occur as dike swarms that emanate from the roof of the source granite pluton. Pegmatitic melts are unlikely to migrate beyond the thermal aureole of the plutonic source (Rubin, 1995). However, more evolved pegmatites can travel further from the pluton. Depending on the size of the pluton, it is possible for the migrations of these melts to be measured in kilometers (Baker, 1998). Host rock and structural features also influence the potential distance from source of a pegmatite dike (Rossovskiy and Konovalenko, 1979). The pegmatite dikes tend to become more fractionated with increased distance from the source (Figure 1.1; Černý et al., 1985).
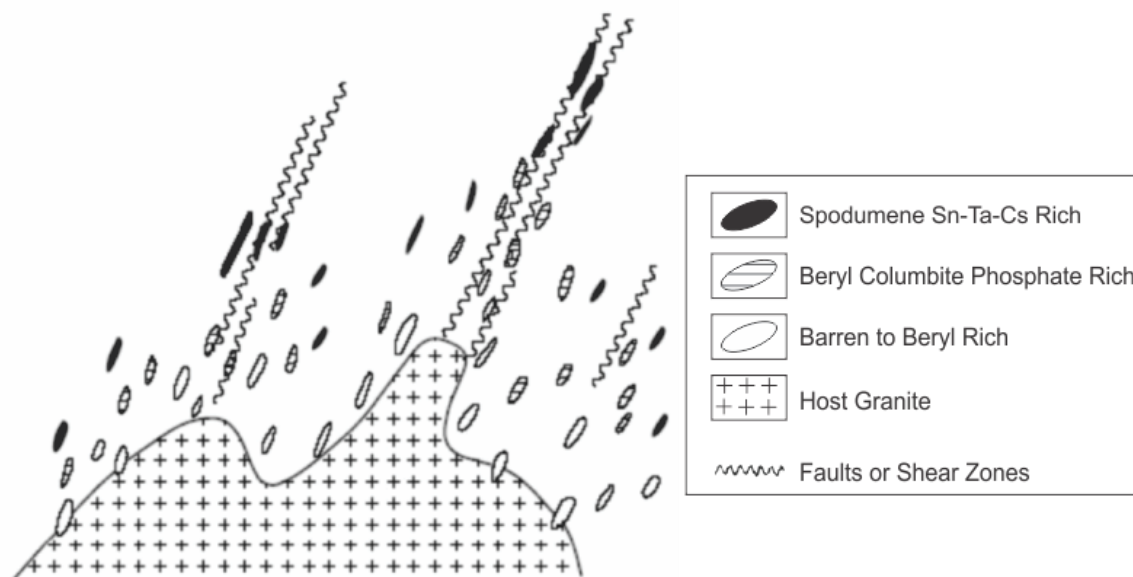
Figure 1.1: Regional zonation within a pegmatite swarm (modified from Černý, 1991b).

Rare metal pegmatites are divided into two families based on the trace element signatures LCT (Li-Cs-Ta) and NYF (Nb-Y-F) (Černý, 1991a). LCT pegmatites contain muscovite as their primary mica and are affiliated with S-type granites (Chappell and White, 2001; London, 2018). NYF pegmatite contain biotite as the primary mica and are associated with A-type and I-type granites (Černý and Ercit, 2005; London, 2018). Černý and Ercit (2005) expanded on the taxonomy adding class, sub-class, type, sub-type (Table 1.1).

Table 1.1.1: The class system of geological, paragenetic and geochemical classification of granitic pegmatites (From Černý and Ercit, 2005).

Class	Subclass	Type	Subtype
Abyssal (AB)	AB-HREE AB-LREE AB-U AB-BBe		
Muscovite (MS)			
Muscovite-Rare-element (MSREL)	MSREL-REE MSREL-Li		

Rare-element (REL)	REL-REE	Allanite-monazite Euxenite Gadolinite	
	REL-Li	Beryl	Beryl-Columbite Beryl-Columbite-Phosphate
		Complex	Spodumene Petalite Lepidolite Elbaite Amblygonite
		Albite-Spodume Albite	
Miarolitic (MI)	MI-REE	Topaz-Beryl Gadolinite-Fergusonite	
	MI-Li	Beryl-Topaz MI-Spodumene MI-petalite MI-Lepidolite	

Pegmatites are commonly zoned, segregated by grain size, texture, or mineralogy. Unzoned pegmatites are typically located in close proximity to the source granite and tend to be poorly evolved (London, 2008). The zonation within pegmatites is generally described as border zone, wall zone, intermediate zone, and core (Cameron et al., 1949; London, 2014). The border zone is the outer most layer, in contact with the host rocks. It is defined by a fine grain size and diverse mineralogy (Cameron et al., 1949). The wall zone is the next zone moving inward. It is differentiated by an increase in grain size and unidirectional solidification textures (Figure 1.2a) and graphic quartz-feldspar intergrowths (Figure 1.2b). It is common for the wall zone to have a similar mineralogy to the border zone (Cameron et al., 1949). Inside of the wall zone is the intermediate zone. The transition wall zone to intermediate zone is typically marked by an increase in grain size and decrease in graphic textures (Figure 1.2b; Jahns, 1953). Crystal sizes are

more uniform and crystal orientation is random. It is not uncommon for pegmatites to have multiple intermediate zones, based on mineralogical variation (Cameron et al., 1949; Norton 1983). In LCT pegmatites, it is common for Li-aluminosilicates (e.g., spodumene, petalite, eucryptite) to form in the inner intermediate zones (London, 2018). The core zone is the innermost zone of the pegmatite. Most core zones are pure quartz. Steeply-dipping pegmatites tend to display bilateral concentric zonation, with increased zonation and chemical evolution toward the top (Cameron et al., 1949, Jahns and Burnham, 1969). Shallow-dipping pegmatites often display asymmetric zonation in layers subparallel to the contacts (Norton, 1983).
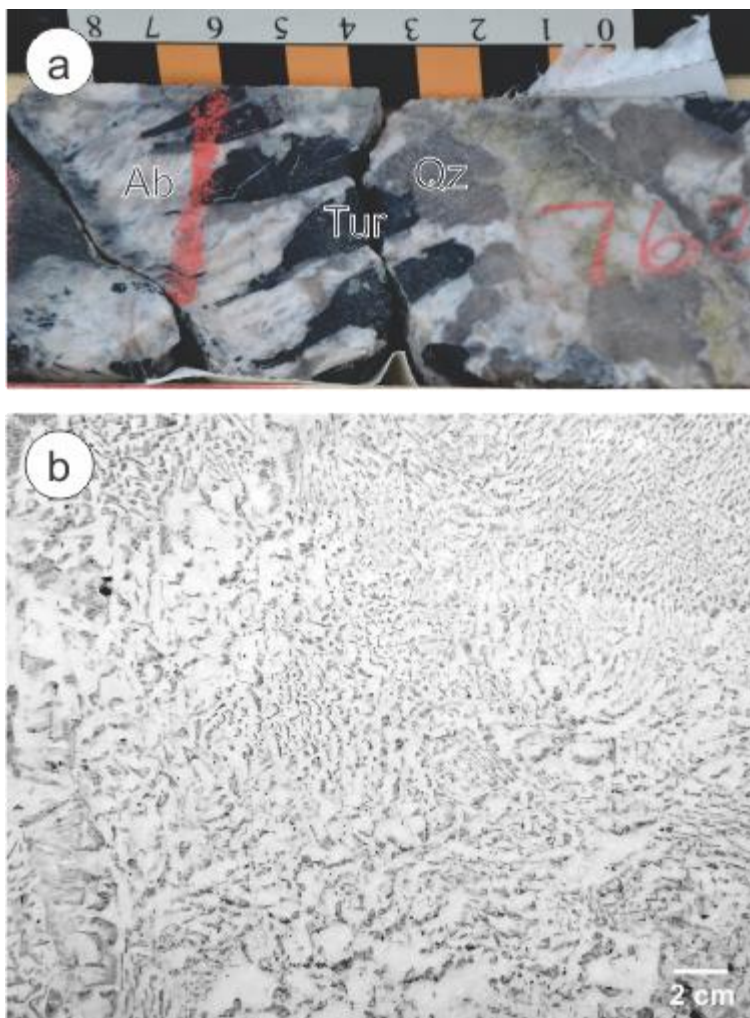
Figure 1.2: a) Unidirectional solidification texture (UST) of tourmaline (Tur-Tourmaline, Ab-Albite, Qz-Quartz), Wekusko Lake, Manitoba (this study) b) Graphic textures, intergrowth of quartz (grey) and K-feldspar (white), Hale quarry, Connecticut (From London, 2018).

Pegmatites are host to multiple potentially economic Li-bearing minerals. Spodumene ($LiAlSi_2O_6$) is the most common Li-aluminosilicate, theoretically containing 7.9 wt% Li_2O. Spodumene is a white-pale green/ pale yellow clinopyroxene, that forms elongate and tabular crystals with two cleavage planes parallel to the C-axis (Deer et al., 1977). The green colour in spodumene is often attributed to the replacement of Al^{3+} to Fe^{3+} (Schwartz and Leonard, 1926; Deer et al., 1977). Spodumene at some pegmatites is

altered to eucryptite ($LiAlSiO_4$) and albite ($NaAlSi_3O_8$). Petalite ($LiAlSi_4O_{10}$) is another common Li-aluminosilicate in pegmatites (most notably Bikita pegmatite, Zimbabwe) (Evans et al., 2014). Petalite is a white-grey phyllosilicate, that forms massive crystals with one strong cleavage plane. Petalite readily breaks downs to spodumene and quartz. Lepidolite and zinnwaldite are Li-micas that currently are of only minor economic importance. Lepidolite is the name given to micas within a solid-solution between the mineral endmembers polylithionite ($KLi_2Al[Si_4O_{10}][OH,F]_2$) and trilithionite ($K[Li_{1.5}Al_{1.5}][AlSi_3O_{10}][OH,F]_2$). Lepidolite is a purple to white mica, that forms hexagonal sheet-like crystals, with perfect cleavage perpendicular to the C-axis. It is difficult to identify these micas in the field, consequently the term 'white' mica is used to refer to light colored mica that includes muscovite, polylithionite, trilithioinite, and other micas such as paragonite (Na equivalent of muscovite) and phengite (Mg-Si substitution in muscovite). Zinnwaldite is the name given to micas within the solid-solution between endmembers polylithionite and siderophyllite ($KFe_2Al[Al_2Si_2O_{10}][OH]_2$). Zinnwaldite is typically brown but may also be green or pale violet and forms hexagonal sheet-like crystals with perfect cleavage perpendicular to the C-axis. Similar to the term 'white mica', the term 'dark mica' is commonly used since zinnwaldite cannot be distinguished from biotite in hand samples. Other Li-bearing minerals found in pegmatites include eucryptite, amblygonite ($[Li,Na]AlPO_4[F,OH]$), triphylite ($LiFePO_4$), and lithiophilite ($LiMnPO_4$).

It is long believed that metasomatism occurs in pegmatites (Schwartz, 1992). Albitization and greisenisation (white mica replacement) are commonly identified in LCT pegmatites (Černý, 1986;). Metasomatism in pegmatites continues to be a widely debated topic (Černý and Burt, 1984; Černý, 1991a; Linnen and Williams, 1993; Audétat and Pettke, 2003; Kontak, 2006; Zajacs et al., 2008; McNeil et al., 2020). Much of the metasomatism is attributed to post-emplacement alteration by fluids. However, McNeil et al. (2020) has shown it is possible to crystallize columbite-(Mn) and lithiophilite through aqueous fluid-melt interactions and theorizes that it would also be possible to crystallize rare metal oxides, other phosphates, and lepidolite by varying the composition of the aqueous fluids. Hydrothermal Li-micas are of particular interest, as micas are a commonly used to understand the magmatic evolution of pegmatites (Černý and Burt, 1984; Joliff et al.,

1987; Roda et al., 1995; Roda et al., 2005; Selway et al., 2005; Roda et al., 2007; Van Litchervelde et al., 2007; Martins et al., 2012; Kaeter et al., 2018; Xing et al., 2020). This means muscovite (or white micas), a mineral widely disperse throughout pegmatites, could be used to better understand both magmatic and hydrothermal processes occurring within the pegmatite body during crystallization.

Micas are the third most common mineral group in granitic pegmatites (Hawthorne and Černý, 1982). Micas are members of the phyllosilicates (i.e., sheet silicates, layered silicates), which references the plate-like and flaky crystal habit. Sheet silicates are constructed of two types of sheets: tetrahedral sheets (T) and octahedral sheets (M). Micas have a T-M-T+C structure, where C is a positively charged interlayer cation (Figure 1.3). There are two variations of the octahedral sheet, dioctahedral containing two trivalent cations and trioctahedral containing three divalent cations. Muscovite, the prevalent mica in LCT pegmatites, is a dioctahedral mica. Polylithionite, a Li-rich mica, is trioctahedral. As muscovite incorporates Li into its crystal structure Li^+ and a divalent cation (e.g., Mg^{2+}, Fe^{2+}, Mn^{2+}) replaces Al^{3+} in the octahedral site, transitioning muscovite from a dioctahedral to trioctahedral mica (Monier and Robert, 1986a,b; Brigatti et al., 2001). White micas are stable over a wide range of physiochemical environments and maintain chemical equilibrium with the melt through recrystallization (Tischendorf, 1997, London, 2005). The chemical behaviour of white mica is well understood and can be modelled with Rayleigh fractional crystallization (Hulsbosch et al., 2014). White micas can incorporate many incompatible elements (e.g., Li, Be, Rb, Cs, Sn, Ta, Nb) (Fleet, 2003). These elements can be used as indicators for chemical evolution with pegmatites. K/Rb ratios are commonly used to as an indicator of fractionation. A decreasing K/Rb ratio is typically coupled with increasing incompatible elements to indicate increasing fractionation/ evolution (Černý and Burt, 1984, Jolliff et al., 1987; Wise et al., 1995; Selway et al., 2005). When combined with the Rayleigh fractional crystallization model of Hulsbosch et al. (2014), it is possible to predict the percentage of crystallization required from a granitic melt to produce a rare-metal pegmatite. The Ta contents of white micas have long been used for tantalite exploration because of its ability to fractionate Ta from Nb (Kovalenko et al., 1996). However, less is known about using white mica compositions for lithium exploration.
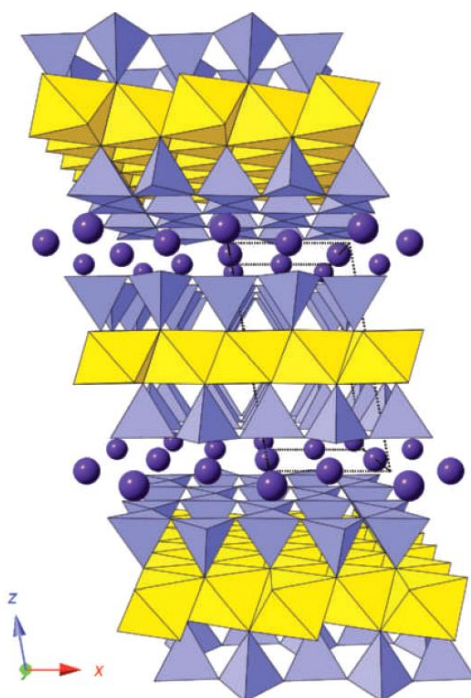
Figure 1.3: crystal structure of Mica (Phlogopite). Blue represents the tetrahedral sheet. Yellow represents the octahedral sheet. Purple circles represent the interlayer cations. (From Deer et al., 2013)

1.3   Pegmatite Exploration Techniques

Pegmatites are present on every continent, typically found in old cratons and younger mountain belts (London, 2018). However, most pegmatites do not contain the rare metals (e.g., Li, Cs, Ta, Nb, Sn) that are the target of pegmatite exploration. Exploration for pegmatite is further complicated by the fact that they are small targets and are typically buried by overburden or were emplaced at depth. Trueman and Černý (1982) have described pegmatites as geophysical non-responders. Although gravity-based surveys have some potential to identify Li pegmatites due to the high density of spodumene, and magnetics can show the contrast between the pegmatite and wallrocks. However, Steiner et al. (2019) was not able to distinguish pegmatites from metasedimentary and metavolcanic hosts using these techniques. Soil geochemistry and lithogeochemistry have been used to successfully identify pegmatites. Lithogeochemistry identifies the trace

element aureoles surrounding the pegmatite dike (Ovchkinnikov, 1976; Morgan and London, 1987). The size of these aureoles can be extended by targeting fracture mineralization (e.g., chlorite) in the surrounding rocks (Linnen et al., 2015). Soil surveys such as mobile metal ion (MMI) and enzyme leach method are able to produce aureoles around pegmatite dike as well (Clark, 1993; Mann et al., 1998). Remote sensing and light detection and ranging (LiDAR) have been successful in identifying pegmatites (Cardoso-Fernandes et al., 2021; Dart Mining NL, 2021). The incorporation of statistical analysis with a various exploration techniques has been able to identify at depth that would not have otherwise been identified (Deveaud et al., 2013; Fyzollahhi et al., 2018).

Once identified, a pegmatite dike must be evaluated for mineral potential. Traditionally this is done by mineralogical classification, e.g., an albite-spodumene pegmatite (Trueman and Černý, 1982). However, pegmatite fields are commonly zoned and display a progression of pegmatite types. This progression can be characterized by using fractionation trends of trace elements (e.g., Li, Cs, Rb, Ta, Nb) of various minerals (e.g., feldspar and mica; Gordiyenko, 1971; Jolliff et al., 1987; Selway et al., 2005). Mineral chemistry uses the fractionation trends of trace element (e.g., Li, Cs, Rb, Ta, Nb) contents in common minerals (e.g., feldspar and mica) to classify pegmatites (Gordiyenko, 1971; Jolliff et al., 1987; Selway et al., 2005). These fractionation trends potentially can also be used to identify high grade zones within pegmatites. White micas have been used to track Ta-Nb contents in pegmatites (Selway et al., 2005). However, the application of the evolution of white mica compositions to the understanding of lithium pegmatites is still poorly understood. Chapter 2 uses the fractionation of trace elements of the white micas to characterize the chemical evolution of pegmatite dikes and the role that fractionation plays in Li enrichment at the Wekusko Lake pegmatites.

Many of the current exploration techniques require expensive and time-consuming laboratory testing. Currently, minerals are analysed by laboratory techniques such as electron probe micro-analysis (EPMA) and inductively coupled plasma mass spectroscopy (ICP-MS). The analysis of Li is problematic because of its low atomic number. Instruments such as handheld X-ray fluorescence (XRF) are not able to identify light elements such as Li (Lemière, 2018). By contrast, it may be possible to identify and

quantify Li contents using the field portable techniques Raman spectroscopy, and laser induced breakdown spectroscopy (LIBS). Chapter 3 investigates the viability of field portable and handheld techniques that can provide fast result and allow for real-time decision making. These techniques are not meant to replace the current proven techniques but help supplement and provide more data for informed decision making.

Raman analysis uses a laser to excite electrons into a virtual state (Smith and Dent, 2005). The virtual state is short-lived, and the electron releases the excess energy as scattered radiation. Most of the electrons return to their original energy level, which is called Rayleigh scattering. However, a small number of electrons do not return to the original energy level, this is called Raman scattering (Smith and Dent, 2005). The rate at which Raman scatter occurs is a function of the vibrational potential of the molecule (Smith and Dent, 2005). As a result, every compound produces a unique Raman spectrum. Raman spectroscopy has been used for mineral identification elsewhere e.g., Haskin et al. (1997), but I am not aware of this technique having been applied to distinguish Li-free muscovite from Li-bearing micas such as polylithionite in the field.

Laser-induced breakdown spectroscopy uses atomic emission spectroscopy to detect the chemical composition of the sample. A high energy laser pulse ablates a small amount of the surface, generating a plasma which emits a characteristic spectrum. The emissions are detected by spectrometers, generating atomic emission lines corresponding to various elements (Lemière and Uvarova, 2019). The spectrum can be compared to a sample library or quantified using calibrated standards. An important consideration when using LIBS is the matrix effect (Connors et al., 2016). Chemical matrix effect occurs when the emission line from one element interferes with another, creating an overlap in the emission spectrum. Physical matrix effects occur based on the physical properties of the sample and location on the sample. Properties such as grain size, hardness, crystallinity roughness, moisture content etc. all effect the plasma generated and can cause variation in the results (Connors et al., 2016). This study uses the LIBS to obtain Li concentrations from white micas with the pegmatites for consideration while evaluating the mineral potential. Samples for this study were analysed by the GeoResources Laboratory, at the Université de Lorraine, France.

1.4   Thesis Objectives

This study aims to deepen the understanding of white mica geochemistry in evolution of Li-bearing pegmatites and the role of white mica in Li exploration. Chapter 2 aims to characterize the mineral chemistry of white mica in Li-bearing pegmatites and relate to the composition of pegmatitic melts with varying degrees of evolution. This can be used to compare multiple dikes and zones within a single dike. Chapter 3 builds on the premise that white mica geochemistry can be used as an indicator of pegmatite evolution and is applied to Li mineral exploration. This study evaluated handheld Raman and LIBS techniques and white mica geochemistry to gauge the potential Li mineralization of a dike in real time, without the need for assays.

1.5   Thesis Format

This thesis contains an introduction (this chapter), followed by two integrated papers to be published. Chapter 2 focuses on the geochemistry of white mica and how the geochemistry can be used to interpret pegmatite. A modified version of Chapter 2 has been submitted to The Canadian Mineralogist and is currently being revised. Chapter 3 focuses on the application of white mica compositions to exploration and includes and evaluation of field portable Raman spectroscopy and LIBS. Conclusions and recommendations for future studies are given in Chapter 4.

1.6   Contributions of Co-authors and Collection of Data

Field mapping and drill core logging was completed by D. Benn, with the assistance of R. Linnen, and T. Martins and A. Hutchins. Drill core was provided by Foremost Lithium Resource and Technology. Lithogeochemistry of host rocks was analysed by Activation Laboratories Ltd. (Actlabs) and paid for by the Manitoba Geological Survey (MGS). Sample and thin section preparation was completed by D. Benn and S. Woods at the University of Western Ontario. Reflected and transmitted light microscopy was completed by D. Benn at the University of Western Ontario. Electron microprobe analysis was completed by M. Beauchamp and D. Benn at the University of Western

Ontario. U-Pb isotope geochemistry and geochronology was completed by C. McFarlane at the University of New Brunswick and paid for by the MGS. Laser ablation inductively couple plasma mass spectrometry was completed by D. Benn under the supervision of I. Samson at the University of Windsor. Handheld Raman spectroscopy was completed by D. Benn at the University of Western Ontario. Handheld LIBS analyses were completed by N. Eddine and C. Fabre at the Université de Lorraine. All interpretations were made by D. Benn under the supervision of R. Linnen and T. Martins.

1.7   References:

Audetat, A., and Pettke, T. 2003. The magmatic-hydrothermal evolution of two barren granites: A melt and fluid inclusion study of the Rito del Medio and Cañada Pinabete plutons in northern New Mexico (USA). Geochimica et Cosmochimica. **67**: 97-121

Baker, D.R., 1998. The escape of pegmatite dikes from granitic plutons: constraints from new models of viscosity and dike propagation. Canadian Mineralogist. **36**: 255–263.

Bartels, A., Vetere, F., Holtz, F., Behrens, H., and Linnen, R.L. 2011. Viscosity of flux-rich pegmatitic melts. Contrib Mineral Petrol.**162**: 51-60

Brown, T.J., Wrighton, C.E., Idoine, N.E., Raycraft, E.R, Shaw, R.A., Deady, E.A., Rippingale, J., and Bide, T. 2016. World Mineral production 2010-2014. British Geological Survey, Keyworth, Nottingham, UK.: 81

Cameron, E.N., Jahns, R.H., McNair, A.H., and Page, L.R., 1949. Internal structure of granitic pegmatites. Econ. Geol. Mono. **2**: 115.

Canosa, F., Martin-Izard, A., and Fuertes-Fuente, M. 2012. Evolved granitic systems as a source of rare-element deposits: the Ponte Segade case (Galicia, NW Spain). Lithos **153**: 165–176.

15

Černý, P., Meintzer, R.E., and Anderson, A.J., 1985. Extreme fractionation in rare-element granitic pegmatites: selected examples of data and mechanisms. Can. Mineral. **23**: 381–421.

Černý, P., 1986. Characteristics of pegmatite deposits of tantalum. In P. Möller, P. Černý, and F. Saupe, Eds., Lanthanides, Tantalum and Niobium,: 195–239.

Černý, P., 1991a. Rare-element granite pegmatites. Part I: anatomy and internal evolution of pegmatite deposits. Geosci. Can. **18**: 49–67.

Černý, P., 1991b. Rare-element granite pegmatites. Part II: regional to global environments and petrogenesis. Geosci. Can. **18**: 68–81.

Černý, P., and Burt, D., 1984. Paragenesis, crystallochemical characteristics, and geochemical evolution of the micas in granite pegmatites. Bailey, S. (ed.) Reviews in Mineralogy, **13**: 257-297.

Černý, P., and Ercit, T.S., 2005. The classification of granitic pegmatites revisited. Can. Mineral. **43**: 2005–2026.

Clark, J.R., 1993. Enzyme-induced leaching of B-horizon soils for mineral exploration in areas of glacial overburden: Transactions of Institution of Mining and Metallurgy (Sect. B: Applied Earth Sciences), **102**: B19-29.

Connors, B. Somers, A. and Day, D., 2016. Application of handheld laser-induced breakdown spectroscopy (LIBS) to geochemical analysis. Appl. Spectrosc. **70**: 810–815.

Dart Mining NL, 2021. LiDAR Mapping of the Dorchap Dyke Swarm Points Towards Increase in Lithium Pegmatites. https://www.listcorp.com/asx/dtm/dart-mining/news/lidar-points-towards-increase-in-lithium-pegmatites-2619048.html. [Accessed March 2022]

Deer, W.A., Howie, R.A., and Zussman, J. 1977. Rock-Forming Minerals: Single-Chain Silicates. 2nd ed. The Geological Society.

Deveaud, S., Gumiaux, C., Gloaguen, E., and Branquet, Y. 2013. Spatial statistical analysis applied to rare-element LCT-type pegmatite fields: an original approach to constrain faults–pegmatites–granites relationships, Journal of Geosciences. **58**: 163-182.

Dingwell, D.B., Hess, K.-U., and Knoche, R. 1996. Granite and granitic pegmatite melts: volumes and viscosities. Trans. R. Soc. Edinburgh, Earth Sci. **87**, 65–72.

Evans, K. 2014. Lithium. In: Gunn G (ed) Critical Metals Handbook. American Geophysical Union.: 230-260

Fyzollahhi, N., Torshizian, H., Afzal, P., and Jafari, M.R. 2018. Determination of lithium prospects using fractal modeling and staged factor analysis in Torud region, NE Iran. Journal of geochemical Exploration. **189**: 2-10.

Fleet, M. E., Deer, W. A., Howie, R.A., and Zussman, J. 2003. Rock-Forming Minerals. Volume 3A. Mica, second ed. The Geological Society, London.

Grew, E.S., 2020. The Minerals of Lithium. Elements. **16**: 235-240.

Gordiyenko, V.V., 1971. Concentrations of Li, Rb, and Cs in potash feldspar and muscovite as criteria for assessing the rare-metal mineralization in granite pegmatites. Int. Geol. Rev. **13**:134–142.

Gruber, P.W., Medina, P.A., Keoleian, G.A., Kesler, S.E., Everson, M.P., and Wallington, T.J. 2011. Global lithium availability. J. Ind. Ecol. **15**: 760–775.

Haskin, L.A., Wang, A., Rockow, K.M., Jolliff, B.L., Korotev, R.L., and Viskupic, K.M., 1997. Raman spectroscopy for mineral identification and quantification for in situ planetary surface analysis: A point count method: Journal of Geophysical Research: Planets. **102**: 19293–19306.

Hawthorne, F.C., and Černý, P. 1982. The mica group. In Short Course in Granitic Pegmatites in Science and Industry (ed. P. Černý). Mineralogical Association of Canada, Winnipeg.: 63–98.

Hulsbosch, N., Hertogen, J., Dewaele, S., André, L., and Muchez, P. 2014. Alkali metal and rare earth element evolution of rock-forming minerals from the Gatumba area pegmatites (Rwanda): quantitative assessment of crystal-melt fractionation in the regional zonation of pegmatite groups. Geochim Cosmochim Acta **132**: 349–374

Ide, Y.F. and Kunasz, I.A. 1989. Origin of Lithium in the Salar de Atacama, Chile. In: Ericken, G.E., Cañas Pinochet, M.T. and Reinemund, J.A. (eds.) Geology of the Andes and its relation to hydrocarbon and mineral resources. Circum-Pacific Council for Energy and Mineral Resources. Earth Science Series **11**: 165–172.

Jahns, R.H., 1953. The genesis of pegmatites. I. Occurrence and origin of giant crystals. Am. Mineral. **38**: 563–598.

Jahns, R.H., and Burnham, C.W. 1969. Experimental studies of pegmatite genesis: I. A model for the derivation and crystallization of granitic pegmatites. Econ. Geol. **64**: 843–864.

Jaskula, B.W. 2016. Mineral Commodity Summaries: Lithium, U.S. Geological Survey.: 100-102.

Jaskula B.W, 2020. Mineral Commodity Summaries: Lithium, U.S. Geological Survey.: 98-99.

Jolliff, B., Papike, J., and Shearer, C., 1987. Fractionation trends in mica and tourmaline as indicators of pegmatite internal evolution: Bob Ingersoll pegmatite, Black Hills, South Dakota. Geochimica et Cosmochimica acta. **51**: 519-534.

Kaeter, D., Barros, R., Menuge, J. F., and Chew, D. M., 2018. The magmatic-hydrothermal transition in rare element pegmatites from southeast Ireland; LA-ICP-MS chemical mapping of muscovite and columbite-tantalite. Geochimica Et Cosmochimica Acta, **240**: 98-130.

Kavanagh, L., Keohane, J., Cabellos, G.G., Lloyd, A., and Cleary, J. 2018. Global Lithium Sources—Industrial Use and Future in the Electric Vehicle Industry: A Review. Resources, **7**: 57.

Kesler, S.E, Gruber, P.W., Medina, P.A., Keoleian, G.A., Everson, M.P., and Wallington, T.J. 2012. Global lithium resources: Relative importance of pegmatite, brine and other deposits. Ore Geology Reviews, **48**

Kontak, D., 2006. Nature and origin of an LCT-suite pegmatite with late-stage sodium enrichment, Brazil Lake, Yarmouth County, Nova Scotia. I. Geological setting and petrology. Can Mineral, **44**: 563–598.

Kovalenko, V.I., Tsaryeva, G.M., Naumov, V.B., Hervig, R.L., and Newman, S. 1996. Magma of pegmatites from Volhynia: composition and crystallization parameters determined by magmatic inclusion studies. Petrology **4**: 277–290.

Kunasz, I. 2007. Lithium Resources. In: Kogel, J. (ed.) Industrial Minerals and Rocks 7th Edition, Society for Mining, Metallurgy and Exploration Inc. (SME), Englewood, Colorado, USA,: 599–613.

Lemière, B. 2018. A review of applications of pXRF (field portable X-ray fluorescence) for applied geochemistry. Journal of Geochemical Exploration, **188**: 350–363.

Linnen, R.L., and Williams-Jones, A., 1993. Mineralogical constraints on magmatic and hydrothermal Sn-W-Ta-Nb mineralization at the Nong Sua aplite-pegmatite, Thailand. European Journal of Mineralogy, **5**: 721-736.

Linnen, R.L., Galeschuk, C. and Halden, N.M., 2015. The use of fracture minerals to define metasomatic aureoles around rare-metal pegmatites; 27th International Applied Geochemistry Symposium, Tucson, Arizona,

Liu, C., Wang, R.C., Wu, F.Y., Xie, L., Liu, X.C., Li, X.K., Yang, L., and Li, X.J. 2020. Spodumene pegmatites from the Pusila pluton in the higher Himalaya, South Tibet: Lithium mineralization in a highly fractionated leucogranite batholith. Lithos,: 358 -359.

London, D. 2005. Geochemistry of alkali and alkaline earth elements in ore-forming granites, pegmatites, and rhyolites. In Rare-element geochemistry and mineral

deposits. GAC Short Course Notes 17 (eds. L. R. Linnen, I. M. Samson). Geological Association of Canada, St. Catharines, Ontario,: 17–44.

London, D. 2008. Pegmatites. Canadian Mineralogist Special Publication, **10**: 368.

London, D. 2014. A petrologic assessment of internal zonation in granitic pegmatites. Lithos, **184-187**: 74–104.

London., D. 2018. Ore-forming processes within granitic pegmatites. Ore geology reviews. **101**: 349-383

London, D., and Morgan, G. 2012. The pegmatite puzzle. Elements, **8**: 263-268.

Mann, A.W., Birrell, R.D., Mann, A.T., Humphreys, D.B., and Perdix, J.L. 1998. Application of the mobile metal ion technique to routine geochemical exploration. Journal of Geochemical Exploration. **61**: 87-102

Martin, G., Rentsch, L., Hoeck, M., and Bertau, M., 2017. Lithium market research–global supply, future demand and price development. Energy Storage Mater., **6**: 171–179.

Martins, T., Roda-Robles, E., Lima, A., and De Parseval, P. 2012. Geochemistry and evolution of micas in the Barroso–Alvão pegmatite field, northern Portugal. The Canadian Mineralogist, **50**: 1117-1129.

McNeil, A., Linnen, R.L., Flemming, R., and Fayek, M., 2020. An experimental approach to examine fluid-melt interaction and mineralization in rare-metal pegmatites. American Mineralogist, **105**: 1078-1087.

Monier, G. and Robert, J.L. 1986a: Muscovite solid solutions in the system K_2O–MgO–FeO–Al_2O_3–SiO_2–H_2O: an experimental study at 2 kbar PH_2O and comparison with natural Li-free white micas. Mineral. Mag. **50**: 257-266.

Monier, G. and Robert, J.L. 1986b. Evolution of the miscibility gap between muscovite and biotite solid solutions with increasing lithium content: an experimental study in

the system K_2O–Li_2O–MgO–FeO–Al_2O_3–SiO_2–H_2O–HF at 600°C, 2 kbar PH_2O: comparison with natural lithium micas. Mineral. Mag. **50**: 641-651.

Morgan, G.B., London, D. 1987. Alteration of amphibolitic wallrocks around the Tanco rare-element pegmatite, Bernic Lake, Manitoba. Am. Mineral. **72**: 1097–1121.

Norton, J.J. 1983. Sequence of mineral assemblages in differentiated granitic pegmatites. Econ. Geol. **78**: 854–874

Ovchinnikov, L.N. 1976. Lithochemical methods of prospecting rare metal pegmatites: Academy of Science USSR, Dept. of Geology of USSR, Institute of Mineralogy, Geochemistry and Crystal Chemistry of Rare Elements, Moscow, USSR. (translated by the Department of the Secretary of State, Ottawa, Canada, 96 p.).

Roda, E., Pesquera Perez, A., Velasco Roldan, F., Černý, P., and Novak, M., 1995. Micas of the muscovite-lepidolite series from the fregeneda pegmatites (salamanca, spain). Mineralogy and Petrology, **55**: 145-157.

Roda, E., Pesquera, A., Gil-Crespo, P.P., Torres-Ruiz, J., and Fontan, F. 2005. Origin and internal evolution of the Li-F-Be-B-P-bearing Pinilla de Fermoselle pegmatite (Central Iberian Zone, Zamora, Spain). Am. Mineral., **90**: 1887-1899.

Roda, E., Keller, P., Pesquera, A., and Fontan, F. 2007. Micas of the muscovite-lepidolite series from karibib pegmatites, Namibia. Mineralogical Magazine, **71**: 41-62.

Rossovskiy, L.N., and Konovalenko, S.I. 1979. Features of the formation of the rare-metal pegmatites under conditions of compression and tension (as exemplified by the Hindu Kush region). Int. Geol. Rev. **21**: 755–764.

Rubin, A.M. 1995. Getting granite dikes out of the source region. J. Geophys. Res. **100B**, 5911–5929.

Schwartz, M.O. 1992. Geochemical criteria for distinguishing magmatic and metasomatic albite-enrichment in granitoids—examples from the Ta-Li granite Yichun (China) and the Sn-W deposit Tikus (Indonesia). Mineralium Deposita, **27**: 101–108.

Schwartz, G.M., and Leonard, R.J. 1926. Alteration of spodumene in the Etta mine, Black Hills, S.D. Amer. J. sci. 5th ser. **11**: 257-264

Selway, J., Breaks, F. and Tindle, A. 2005. A review of rare-element (Li-Cs-Ta) pegmatite exploration techniques for the Superior Province, Canada, and large worldwide tantalum deposits; Exploration and Mining Geology, **14**: 1–30.

Smith, E., and Dent, G. 2005. Modern Raman Spectroscopy – A Practical Approach. John Wiley and Sons Ltd, Chichester, 2005,.

Tarascon, J.M. 2010: Is lithium the new gold? Nat. Chem. **2**: 510.

Tischendorf G., Gottesmann B., Förster H.J., and Trumbull R.B. 1997. On Li-bearing micas; estimating Li from electron microprobe analyses and an improved diagram for graphical representation. Mineral. Mag. **61**: 809–834.

Van Lichtervelde, M., Salvi, S., Béziat, D., and Linnen, R.L. 2007. Textural features and chemical evolution in tantalum oxides: Magmatic versus hydrothermal origins for Ta mineralization in the Tanco Lower Pegmatite, Manitoba, Canada. Economic Geology, **102**: 257–276.

Xing, C., Wang, C., and Wang, H. 2020. Magmatic-hydrothermal processes recorded by muscovite and columbite-group minerals from the Bailongshan rare-element pegmatites in theWest Kunlun-Karakorum orogenic belt, NW China. Lithos. 364-365.

Yaksic, A., and Tilton, J. 2009. Using the Cumulative Availability Curve to Assess the Threat of Mineral Depletion: The Case for Lithium Policy,: 34.

Zajacz, Z., Halter, W.E., Pettke, T., and Guillong, M. 2008. Determination of fluid/melt partition coefficients by LA-ICPMS analysis of co-existing fluid and silicate melt inclusions: Controls on element partitioning. Geochimica et Cosmochimica Acta, **72**: 2169–2197.

2 Integrated Paper 1

2.1 Introduction

Pegmatites are host to economic deposits of certain elements that are part of the critical minerals list for Canada (NRCAN, 2021) and other countries (Bobba et al., 2020). Among them, Li is important for its use in battery technology. Lithium has other uses including the manufacture of ultra-low expansion glass and ceramics (e.g., glass stovetops), Li-based grease, which represent approximate 75% of lubricants, and its long-time use in medication of bipolar disorder (Bibienne et al., 2020). In pegmatites, spodumene (6-9 wt% Li_2O) is the main Li ore mineral, and to a lesser degree petalite (4-5 wt% Li_2O) and lepidolite (~4 wt% Li_2O) (Garret, 2004; London, 2008; Evans, 2014). Other ore minerals from the critical minerals list found in pegmatite minerals are pollucite (30-35 wt% Cs_2O), cassiterite (SnO_2) and columbite-tantalite $((Mn,Fe)(Ta,Nb)_2O_6)$. Due to the coarse grain size of pegmatites, whole rock chemistry has limited use, but the evolution of pegmatites can be quantified using the changes in concentrations of incompatible trace elements (Li, Be, B, Rb, Cs, Ba, Sn, Nb, and Ta) in minerals such as K-feldspar, white mica, garnet, and tourmaline (Kovalenko et al., 1980; Joliffe et al., 1987; Roda et al., 1995; Fleet et al., 2003; Brigatti et al., 2001; Groat et al., 2003; Selway et al., 2005; Roda et al., 2007; Van Lichtervelde et al., 2008; Potter et al., 2009; Martins et al., 2012; Hulsbosch et al., 2014; Dewaele et al., 2015; Maneta and Baker, 2019; Ballouard et al., 2020; Chakraborty and Upadhyay, 2020). White micas (a general term used for mica in a solid solution series with muscovite, phengite or paragonite) in particular are present in most peraluminous granitic pegmatites and because the Li and other trace element contents of white micas can range from tens of ppm to weight percent levels, this mineral provides a window to the magmatic and hydrothermal processes in pegmatites.

Micas are sheet silicates constructed of an octahedral sheet between two tetrahedral sheets. The octahedral sheet consists of two OH^- planes of either side of divalent (M^{2+})

cations or trivalent (M^{3+}) cations (Bailey, 1984). If the octahedral site is occupied by three divalent cations, it is trioctahedral, if the octahedral site is occupied by two trivalent cations it is known as dioctahedral, and one site is left vacant (Bailey, 1984). Muscovite is a dioctahedral mica, which can be in solid solution with trilithionite, a trioctahedral mica. Commonly, where Li substitutes into a dioctahedral mica, the trivalent cation is replaced with a divalent cation and Li fills the vacant site (Brigatti et al., 2001).

Parameters such as the K/Rb ratio in white micas are commonly used to evaluate the magmatic evolution of pegmatites (e.g., Černý and Burt 1984, Joliff et al., 1987). However, our understanding of how Li concentrations evolve in melts and fluids is less well understood. The influence of hydrothermal processes in pegmatites are not well understood (Linnen and Williams-Jones, 1993; Tindle et al., 1998; Kontak, 2006; Van Lichtervelde et al., 2008). It has been proposed that Nb-Ta mineralization, in LCT-pegmatites, crystallizes from late-stage Na-rich fluids (Kontak, 2006). Textures such as miarolitic cavities, fluid inclusion studies, and stable isotope fractionation provide evidence for fluid exsolution from during pegmatite formation (Thomas et al., 2012; London, 2014; Siegel et al., 2016). White mica compositions may help further the understanding of composition and timing of these fluids. Aside from being widely distributed in all zones of pegmatites, white mica maintains close equilibrium with the melt while under near-liquidus conditions (London, 2005). Kaeter et al., (2018) show three stages of white mica crystallization in pegmatites, pure magmatic, magmatic-metasomatic, and last melt-hydrothermal precipitation. However, it is not clear how applicable the interpretations of Kraeter et al., (2018) are to pegmatites in general, and Li pegmatites in particular.

The Zoro Lithium Project within the Wekusko Lake pegmatite field in Manitoba is the current focus of lithium exploration by Foremost Lithium (formerly FAR Resources Ltd.). This study focuses on Dike 1, the primary resource on this property with an NI43-101 inferred resource of 1.1 Mt of 0.91% Li_2O with a 0.3% Li_2O cut-off (Fedikow and Zelligan, 2018). Dike 1 is well characterized in three dimensions by 23 drill holes. This dike offers an excellent opportunity to examine the textural and chemical evolution of white micas in a Li-rich, spodumene-bearing pegmatite through field mapping, drill core

logging, petrography, and mineral chemistry. These data will be integrated to evaluate the use of white micas to interpreting the magmatic and hydrothermal evolution of Li pegmatites.

2.2 Geological Setting

The Wekusko Lake pegmatite field is located in the Snow Lake-Flin Flon area of west-central Manitoba, Canada and is part of the 1.91-1.83 Ga Flin Flon-Glennie complex (Snow Lake Block; Figure 2.1) of the Trans-Hudson Orogen (THO) (Connors et al., 2002). The THO is a Paleoproterozoic collisional belt between the Archean Superior province, the Rae-Hearne cratons and the Sask craton in Canada, and the Wyoming craton in the United States (Hoffman et al., 1989; Lewry et al., 1994; Connors et al., 2002; Schneider et al., 2007; Hammer et al., 2010; Darbyshire et al., 2017). It spans from central United States, through central and northern Canada and Greenland and may connect with orogenic belts in Scandinavia (Hoffman et al., 1988; Schneider et al., 2007; Eaton and Darbyshire, 2010). The THO is mainly comprised of accreted Proterozoic arc rocks, continental metasedimentary rocks and reworked parts of the Rae-Hearne and Superior cratons (Hoffman et al., 1989; Lewry et al., 1994). In the Saskatchewan-Manitoba segment, the THO is divided into four lithotectonic zones: 1) the Superior Boundary Zone to the east, comprised of supracrustal segments most notably the Thompson nickel belt and Fox River belt; 2) the Reindeer Zone, a collage of juvenile supracrustal belts and sedimentary basins that comprise the Rottenstone-Southern Indian domain; the La Rouge-Lynn Lake-Leaf Rapids domain; the Kisseynew domain and Flin Flon-Glennie Complex; 3) Chipewyan-Wathaman Batholith, an Andean-type continental magmatic arc; and, 4) the Cree Lake Zone, a reworked continental margin of the Hearne craton (Figure 2.1: Lewry et al., 1994; Corrigan et al., 2005; Schneider et al., 2007; Eaton and Darbyshire, 2010). The Sask craton is only exposed at surface in three windows. and underlies much of the Reindeer zone (Lucas et al., 1994; Lewry et al., 1994). The Flin Flon-Glennie Complex of the of Reindeer Zone is further divided into the Glennie Domain, the Hanson Lake Block, the Flin Flon Belt, and the Snow Lake Block (Kraus and Menard, 1997; Schneider et al., 2007). The Flin Flon-Glennie Complex, host to Wekusko Lake pegmatite field, has a metamorphic gradient that ranges from lower

greenschist facies in the south to upper amphibolite facies at the northern boundary with the Kisseynew domain (Černý et al., 1981; Lewry et al., 1994; Kraus and Menard, 1997).
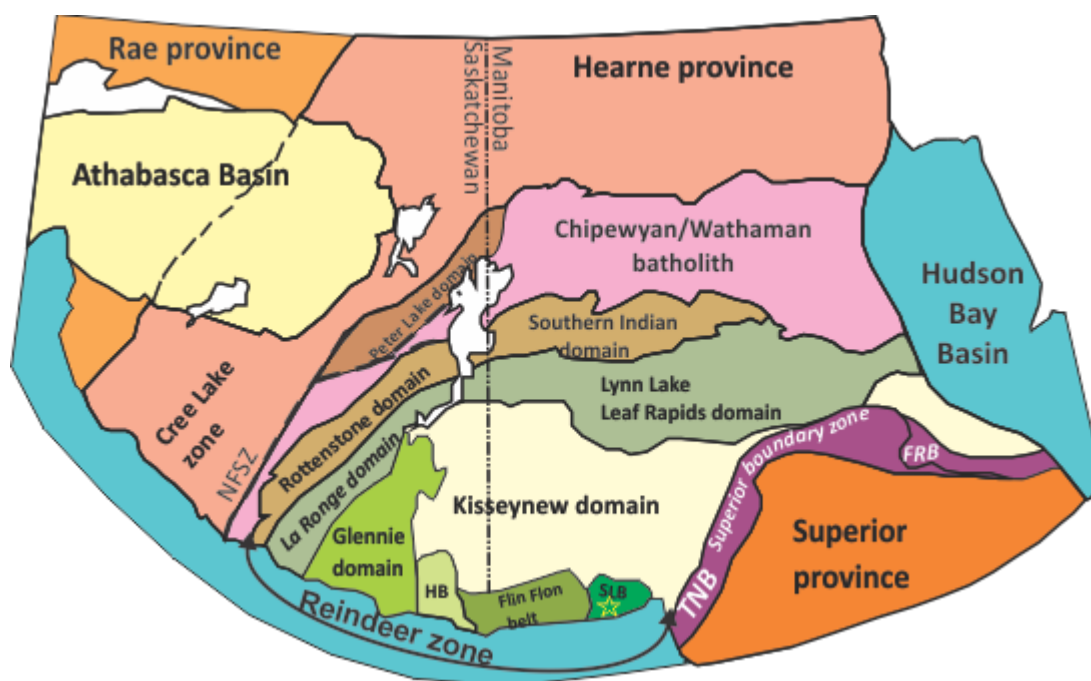
Figure 2.1: Simplified geological map of the Saskatchewan-Manitoba Segment of the THO, show the main lithotectonic subdivisions and major structural boundaries (after Hoffman et al., 1988). Abbreviations: NFSZ, Needle Falls Sheer Zone; HB, Hanson Lake Block; SLB, Sn.

2.2.1   Structural History

The Wekusko Lake area has undergone four deformational events (D1-D4) before craton stabilization at 1.70 – 1.65 Ga (Schneider et al., 2007). The first deformational event (D1) recorded folding associated with the accretion of the Flin Flon-Glennie arc (1.88-1.87 Ga; Connors et al., 1999). Plutonism and crustal shortening within the Chipewyan-Wathaman batholith led steepening of syn-accretionary fabrics in the Snow Lake Block (1.87-1.84 Ga; Lucas et al., 1996; Corrigan et al., 2005). The D2 deformational event

recorded south to southwest compression and the collision of the Kissynew domain and Flin Flon-Glennie arc with the Sask craton (1.84-1.81 Ga), which resulted in the inversion of the Kisseynew turbidite basin (Connors et al., 1999). The collision with the Sask craton led to regional peak metamorphism at 1.81 Ga (Gordon et al., 1990; David et al., 1996; Schneider et al., 2007) during which, the Snow Lake block reached temperatures between 500°C and 700°C and pressures between 0.4 and 0.6 GPa (Kraus and Menard, 1997). The D3 deformational event occurs shortly after peak metamorphism (Connors et al., 2002) at 1.81Ga and recorded transpressional northwest trending shortening and associated burial of the Sask craton at syn- to post-peak metamorphic conditions (Ryan and Williams, 1999; Corrigan et al., 2005). The D3 event is link to the formation of the Crowduck Bay fault and Roberts Lake fault (Connors et al., 2002). This event is also recorded by Northeast trending mineral extension lineations (Connors et al., 2002). The D4 deformational event recorded brittle to ductile deformation, caused by northwest trending compression (Černý et al., 1981; Lucas et al., 1994; Connors et al., 1999). It is possible that D4 is a continuation of D3 (Connors et al., 2002). The D3 and D4 events have not been dated. However, late-collisional metamorphism associated with southwest trending transpressional deformation is reported to have occurred at 1.77 Ga (Schneider et al., 2007), which may be linked to either the D3 or D4 events. The amalgamated craton is interpreted to have been stable between 1.70 and 1.65 Ga (Schneider et al., 2007; Hammer et al., 2010).

2.3   Wekusko Lake pegmatite field

The pegmatite dikes in this study are part of the Green Bay Group of the Wekusko Lake pegmatite field (Černý et al., 1981), located west of Roberts Lake within the Roberts Lake Fault Block of the Snow Lake Block (Figure 2.2). The field area of this study is host to at least thirteen pegmatite dikes (Grammatikopoulos et al., 2020), and exploration in the area is ongoing. The field area was mapped at a 1:4 000 scale in this study (Benn et al., 2018) with a focus on dike mineralogy, morphology, and deformation (Figure 2.2; Benn et al., 2018) of the eight dikes that were known of at the time. The pegmatites are hosted primarily by an amphibolite unit and to a lesser extent in the quartzofeldspathic gneiss of the Missi Group meta-sedimentary rocks (Bailes, 1980). These are the two main

units in the Roberts Lake fault block, which is bound by intersecting faults in the southwest (NATMAP Shield Margin Project Working Group, 1998; Connors et al., 1999; 2002).
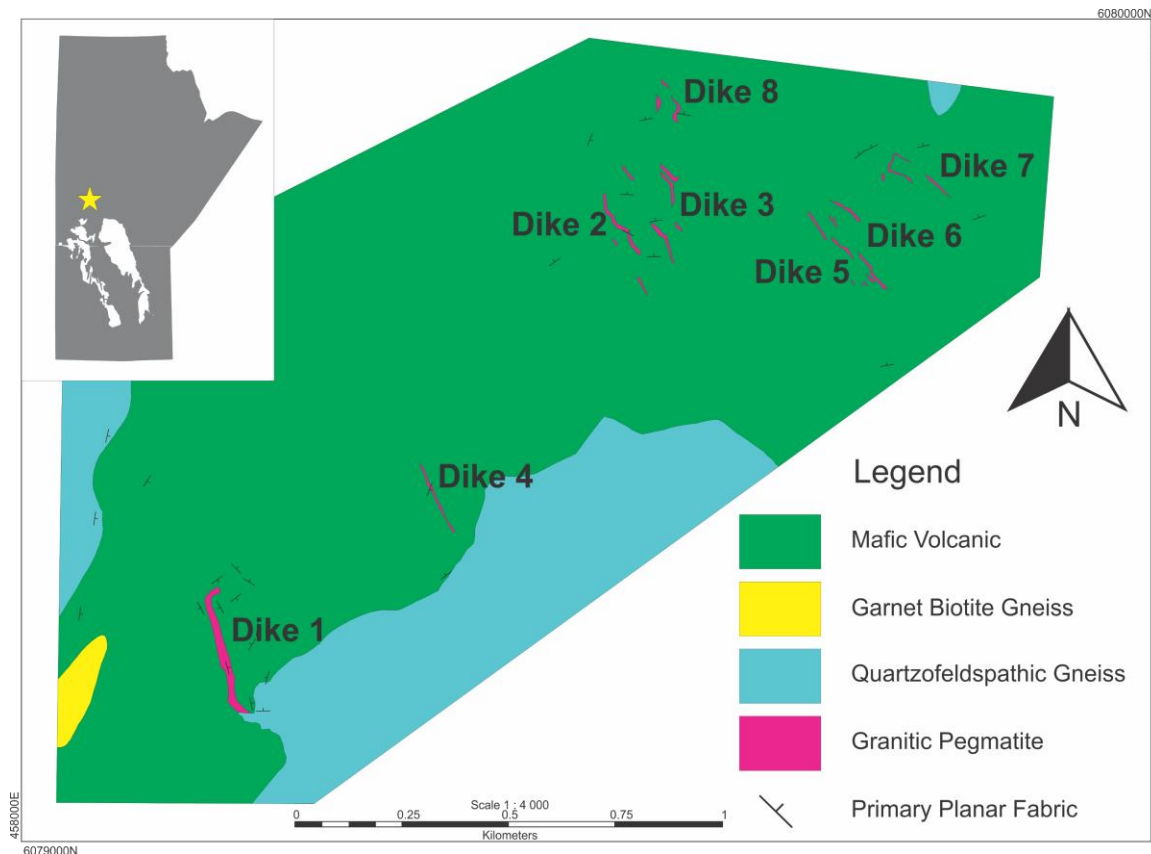
Figure 2.2: Simplified geological map of the Wekusko Lake pegmatite field (Manitoba, Canada), modified from Benn et al., 2018.

Dike 1 is approximately 300 m long and 15 m thick at surface, and 40 m thick at depth (Grammatikopoulos et al., 2020). Cross sections of Dike 1 can be found in the Foremost Lithium (FAR resources) 43-101 technical report (Fedikow and Zelligan, 2018). The other dikes are between 5-10 m thick and 50-180 m long at surface. All of the dikes are sub-vertical. Pegmatite dikes are podiform shaped, and the thickness of the dikes change locally as it pinches and swells. The largest dike, Dike 1, is mostly planar and deformation is mainly observed at ends where the dike is thinner. Evidence of deformation include elongated and stretched minerals as well as white mica with kink bands, similar to the observations made by Martins et al. (2017). The other dikes (Dike 2

- 8), which are thinner, display gentle S-shaped folds throughout the full length of the dike. Thin granitic dikes and dikelettes (<30cm thick) are present throughout the field area as well, but not significant enough in size to include on the map. These dikelettes display more extreme folding and are boudinaged than the mapped dikes. The timing of emplacement of the dikes is thought to be post-tectonic (Černý et al., 1981). However, the deformational features observed in this study indicate that emplacement was prior to the end of regional deformation, i.e., late D3 or early D4.

2.3.1   Host rocks

The amphibolite host of the pegmatite is a fine-grained mafic meta-volcanic rock consisting primarily of amphibole and lesser plagioclase, locally with accessory garnet. The foliations in the amphibolite generally trend northeast and display both gentle and tight folds. These foliations are deflected at boundaries with the pegmatite dikes in some locales. Remnants of pillow basalt are locally preserved, although the deformation of the pillows precludes determining a younging direction with absolute certainty. However, a limited number of persevered pillows suggest a younging direction to the east.

The quartzofeldspathic gneiss consists of feldspar, quartz, and biotite that is interpreted to be part of the Missi Group meta-sedimentary rocks (NATMAP Shield Margin Project Working Group, 1998). The gneiss does not host pegmatite dikes in the study area, except the southern most tip of Dike 1 (Figure 2.2), where the dike reduces in width from 10 m to 10 cm over approximately 10 m in the gneiss. Thus, this unit may act as a rheologic control on the emplacement of the dikes. A biotite-garnet gneiss is also present in the southwest edge of the field area and is interpreted as part of the Burntwood Group (NATMAP Shield Margin Project Working Group, 1998). No dikes in this study were observed to have intruded rocks from the Burntwood Group. For a complete description of the host rocks see Benn et al. (2018b; Appendix A).

2.3.2   Pegmatite dikes

Eight of the thirteen granitic pegmatite dikes were observed during this study. The studied dikes were drill tested by FAR Resources Ltd. (Foremost Lithium) and drill core

from the eight dikes was logged and sampled by cutting the core into quarters. All the dikes in the mapping area share similar mineralogy and vary mostly in grain size and mineral ratios. The dikes mostly consist of albite, quartz, white mica, K-feldspar, spodumene, and tourmaline with accessory apatite, Fe-Mn phosphate minerals, beryl, and garnet with traces of columbite group minerals (CGM), arsenopyrite and cassiterite (Benn et al., 2018b; Grammatikopoulos et al., 2020). These dikes can be classified as Li-Cs-Ta (LCT), Rare-element (REL) class, REL-Li subclass, complex type, spodumene sub-type (Černý and Ercit, 2005). The pegmatite dikes have undergone variable degrees of hematization and display a gradient of red in the wall to white in the center. Local aplitic patches are observed throughout the pegmatite that range from 5 cm to 30 cm across that are mineralogically similar to the surrounding pegmatite. No miarolitic cavities were observed in the dikes. Dikes crosscut foliations in host rocks and the foliation in the host rock is locally deflected. Dikes strike from 115° to 187° and dip sub-vertically (Benn et al., 2018b). Metallurgical work was conducted on a bulk sample of Dike 1 by Grammatikopoulos et al. (2020) and they reported a modal composition of 10.5% spodumene, 29% quartz, 29% plagioclase, 21% K-feldspars, 5% micas, 3% tourmaline and 0.1% Fe-Mn-phosphates.

2.3.2.1   Pegmatite Zones

The dikes consist of up to 5 zones (Figure 2.3) based on field observation of mineralogy, grain size, and degree of alteration. From the outer contact to the centre the zones are: border, wall, intermediate, central, and core. All zones are not present in all dikes and zonation can vary with depth in individual dikes, and the contacts between zones are gradational. The border and core zones are the least common and smallest zones and the core, central and border zone were not observed in all dikes. The distribution of zones is not necessarily in a concentric pattern and the presence of individual zones can be intermittent with depth in a drill hole.

Hematite alteration is prevalent throughout the border and wall zones, and to a lesser extent in the intermediate zone. This gives the rock a red to pink hue. Hematite alteration is concentrated at grain boundaries. Consequently, fine-grained masses are commonly

darker red, and the feldspars are more difficult to identify. This variation in colour between coarse- and fine-grained albite makes it difficult to distinguish albite from K-feldspar in some hand samples. By contrast, these minerals are easily distinguished in thin sections.
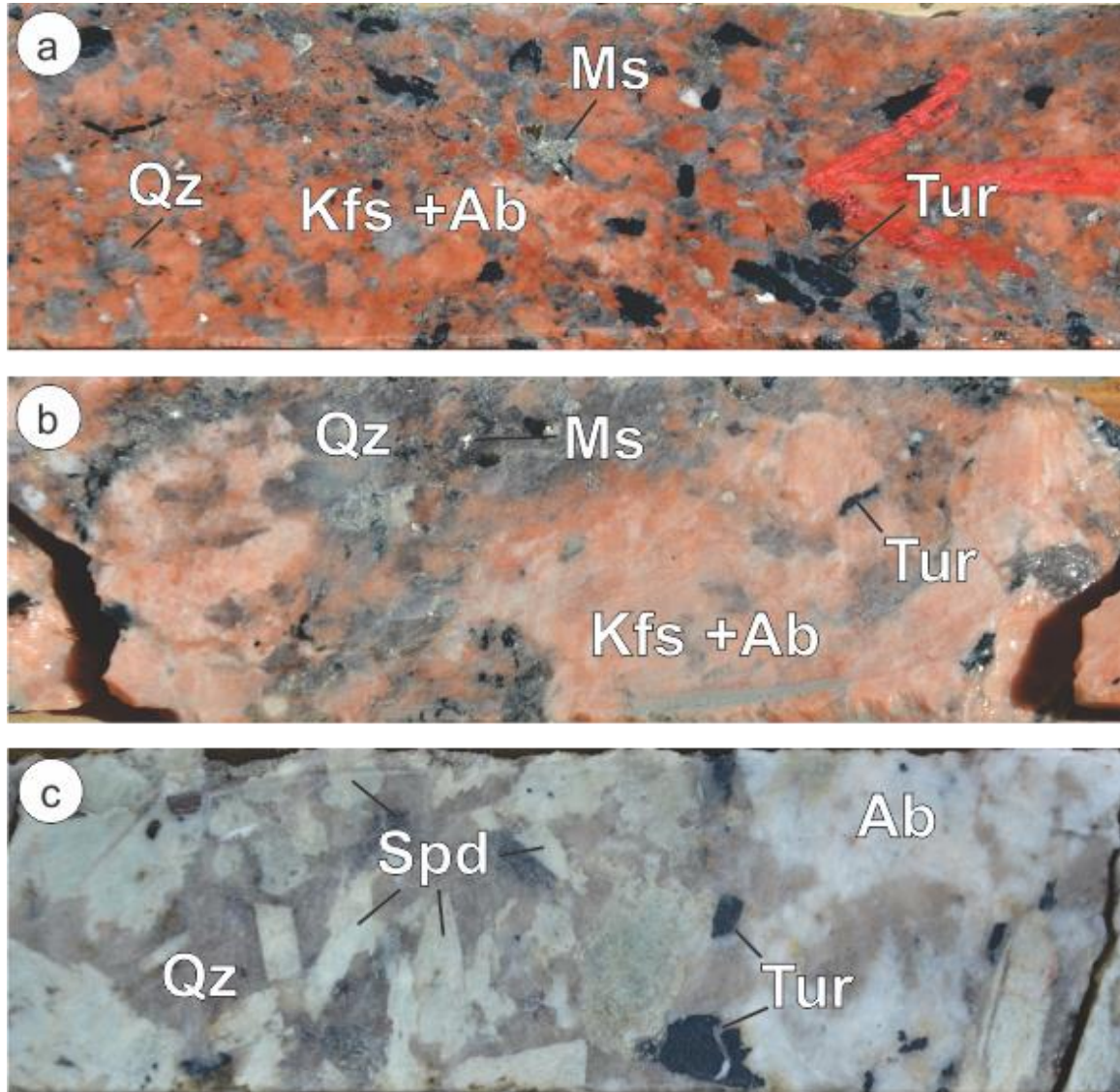
Figure 2.3: Photographs of halved NQ drill core displaying the transition from Wall zone to Central zone. A) Wall zone; b) Intermediate Zone; c) Central zone. Width of NQ drill is 47.66 mm.

The border zone is the thinnest zone, only 1 cm thick at the contacts of the dikes with the host rocks. It is composed of albite, quartz, K-feldspar, white mica, and tourmaline. Grain sizes vary between 0.5 and 2 mm. The minerals are generally oriented perpendicular to the contact, which is interpreted that the minerals grew inwards. This is readily observed in tourmaline comb textures.

The wall zone (Figure 2.3a) is the outer most zone in most dikes where the border zone is not present. The wall zone is comprised of albite, quartz, K-feldspar, white mica, and tourmaline with accessory spodumene, apatite, Fe-Mn phosphate minerals and beryl and trace CGM. Traces amounts of pyrite, chalcopyrite, cassiterite, zircon, xenotime, and uraninite were also identified during scanning electron microscope (SEM) analysis. The average grain size in the wall zone is between 0.25 and 2 cm. However, rare larger crystals up to 5 cm long are also present. Tourmaline crystals in this zone propagate outward from the host rock contact in comb structures. This zone is generally brick red due to a high degree of hematization.

The intermediate zone (Figure 2.3b) is the next outer-most zone and typically the thickest zone. The intermediate zone is composed of albite, quartz, white mica, and spodumene with accessory apatite, K-feldspar, Fe-Mn phosphate minerals, beryl, and trace CGM. Trace amounts of arsenopyrite, chalcopyrite, sphalerite, cassiterite, loellingite, xenotime and uraninite were also identified during SEM analysis. The average grain size is between 0.5 and 5 cm with larger crystals up to 10 cm in length. The intermediate zone consists of about 5% spodumene and a moderate to low amount of hematization gives the intermediate zone a salmon pink colour.

The central zone (Figure 2.3c) is the inner-most zone in the majority of dikes where the core zone is not present. This zone is composed of albite, spodumene, quartz, K-Feldspar and white mica with accessory tourmaline, apatite, CGM and Fe-Mn phosphate minerals. Traces of pyrite, arsenopyrite, monazite, zircon and uraninite were also identified during SEM analysis. The central zone is main host of lithium mineralization in the dikes and consists of 10 to 30% spodumene. The average grain size is between 3 and 10 cm, with

larger crystals up to 25 cm in length. There is little to no hematization observed in this zone, and its colour is a pale green to grey.

The core zone is rare, but where present is the inner-most zone of the dikes. It is composed of mainly quartz, with albite and minor spodumene. The average grain size is between 3 and 10 cm with larger crystals up to 25 cm long. Spodumene makes up less than 5% of this zone.

2.4   Analytical Methods

Whole rock analyses of the amphibolite host rock collected from drill core and outcrop samples were cleaned and weather surfaces removed, then samples were crushed to <5 mm using steel-jaw crusher. Samples were then pulverized in a vibratory-ring pulveriser and milled to <200 µm mesh. Sample preparation was completed at Manitoba Geological Survey Midland Sample and Core Library in Winnipeg, MB. Samples weighing 55 g were submitted to Actlabs, Ancaster, ON. For major, minor and trace element analyses using research grade lithogeochemistry package (4Lithoresearch). One internal standard from the Manitoba Geological Survey was also submitted. Samples were analysed using ICP-MS on the Perkin Elmer Sciex ELAN 6000, 6100, or 9000. Samples were submitted for major- (Si, Al, Fe, Mn, Mg, Ca, Na, K, Ti, and P), in oxide wt.%, and trace-element (Sc, Be, V, Cr, Co, Ni, Cu, Zn, Ga, Ge, As, Rb, Sr, Y, Zr, Nb, Mo, Ag, In, Sn, Sb, Cs, Ba, La, Ce, Pr, Nd, Sm, Eu, Gd, Tb, Dy, Ho, Er, Tm, Yb, Lu, Hf, Ta, W, Tl, Pb, Bi, Th, and U), in ppm, analysis using the research-grade lithogeochemistry package (4Litho-research). Appendix B.

The petrographic analysis of polished thin sections and thick sections cut from quartered drill core samples was completed using a transmitted and reflected light microscope at the Earth and Planetary Materials Analysis Laboratory at Western University. Additional petrographic observations were made using a JEOL JMC-600 NeoScope benchtop Scanning Electron Microscope equipped with the JEOL JED-2300 energy dispersive X-

ray analyser at Western University, London, ON. Petrographic descriptions of all thin section samples from this study are included in Appendix C.

Thin sections and thick sections were carbon-coated prior to single point analyses back-scatter electron (BSE) imagery and element maps were acquired using an energy dispersive spectrometer (EDS), on the JEOL JXA-8530F field-emission election probe microanalyser (EPMA) at Western University, London, ON, to determine whether individual grains were zoned. Subsequently, point analysis of major and minor elements were determined using wavelength dispersive (WDS) and EDS detectors. The microprobe operating conditions were an accelerated voltage of 15 kV and a beam current of 100 nA with a beam size of 10 µm. Analysis counting times were 60 seconds. Ten-point transects of electron microprobe analyses (EPMA) were taken from core to rim to measure intragrain variations. Mineral calibrations standards used for analysis were orthoclase (K, Al, Si), albite (Na), anorthite (Ca), olivine (Mg, Fe), pollucite (Cs), fluorite (F), rutile (Ti), and synthetic $RbTiOPO_4$ (Rb). Errors on analyses are reported on Appendix D. Laser Ablation Inductively Coupled Plasma Mass Spectroscopy (LA-ICP-MS) of white mica was conducted at the Element and Heavy Isotope Analytical Laboratories at the University of Windsor using the Photon Machine 193 nm short pulse width Analyte Excite excimer laser ablation system coupled with an Agilent 7900 quadrupole mass spectrometer to determine trace elements and, in particular, lithium contents. Transects were taken from core to rim, as close as possible to the EPMA transects. One hundred thirty-eight traverses were completed across 67 mica grains. The data was obtained using 1.07 to 1.2 kV acceleration potential, and 4.1 mJ energy, with a beam size of 25 µm and a repetition rate of 25 Hz. Background was collected for 30 seconds before an ablation time of 60 seconds. The grains were ablated with a laser fluency of ~2 J/cm^2. NIST-610 was used as the external standard. Silicon concentrations obtained from the EPMA were used as an internal standard for each grain. Errors on analyses are reported in Appendix E. Data reduction was completed using Iolite software, an add-on for Igor Pro by Wavemetrics (Paton et al., 2011). Columbite group minerals were element mapped, using the EPMA, to determine internal zonation of Fe, Mg, Mn, Nb, Ta, Sn, Ti, U, W, and Zr. The microprobe operating conditions were an accelerated voltage of 15kV, a beam current of 100 nA, and a dwell time of 10 s.

LA-ICP-MS data collected from white micas were processed as the whole length of a traverse to obtain average values that could be used to determine the composition of the grain as a whole. The same traverses were divided into subsections based on BSE imagery textures to obtain a higher resolution for the data and to characterize intragrain heterogeneity. Major and minor element (Si, Al, Ti, Fe, Mg, Na, K, Rb and F) data obtained from EPMA was paired to corresponding minor and trace element (Li, Ba, Mn, Cs, Be, Nb, Ta, Sn, and Tl) data obtained from LA-ICP-MS. Data points gathered from LA-ICP-MS traverses were paired with the closest EPMA spot analysis using BSE imagery.

The CGMs were analysed for U-Pb geochronology using LA-ICP-MS at the University of New Brunswick, Fredericton, NB using an Australian Scientific Instruments RESOlution Series M-50-LR 193 nm excimer-laser-ablation system coupled with an Agilent 7700x quadrupole ICP-MS. Reference material included NIST610 glasses, and well-characterized columbite-tantalite U-Pb age standards. These standards are the 1060 Ma Kragero pegmatite, southeastern Norway, the 500 Ma Ipe mine, Brazil, and the 270 Ma Amelia tantalite from the Morefield pegmatite, USA (Horn and von Blanckenburg., 2007; McFarlane and Luo, 2012). The data was obtained using a beam size of 24μm and a repetition rate of 3.5 Hz. Background was collected for 30 seconds before an ablation time of 30 seconds. The grains were ablated with a laser fluency of ~3 J/cm^2. Elements and isotopes analysed were Nb^{93}, Ta^{181}, Pb^{204}, Pb^{206}, Pb^{207}, Pb^{208}, Th^{232}, and U^{238}. Sixty-three measurements were made across 15 CGM grains.

2.5   Results

2.5.1   Mineralogy and Petrography

Two types of white mica were identified in hand samples. The first type of white mica is brown to light brown, coarse-grained, and occurs as subhedral books up to 5 cm in diameter that are in planar contact with other pegmatite minerals, indicating that they are primary magmatic in origin. This type of white mica is found in all zones of the pegmatite. Locally within the wall zone, this phase forms combs at the host rock contact,

similar to tourmaline. Figure 2.4a is an example of this type of white mica in a thin section in planar contact with primary albite. The second type of white mica is green-brown, fine-grained, subhedral to anhedral, and typically less than 1 mm across. This phase typically forms in masses intergrown with quartz, typically having filled around larger euhedral to subhedral grains of other minerals. In thin section (Figure 2.4b), these grains are observed to have grown on and around larger primary magmatic grains. The second type of white mica is only present in the central and intermediate zones.
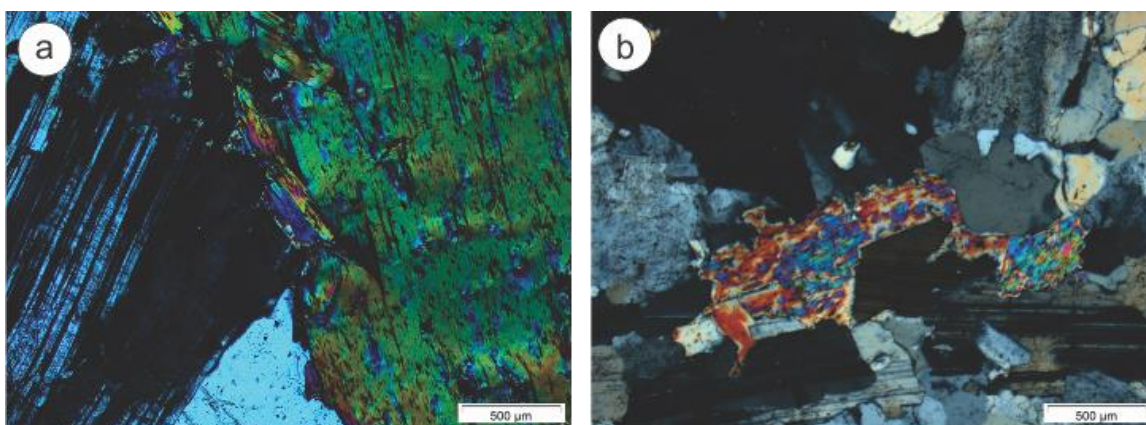
Figure 2.4: Cross-polarized optical microscope imagery at 2.5x magnification of muscovite interacting with albite a,) primary muscovite; b) late-stage muscovite.

Four textural types of white mica were identified using BSE imaging (Figure 2.5): poorly zoned, rimmed, patchy, and grains that host rod-shaped inclusions (RSI). Most of the variation in the BSE images is caused by differences in Cs concentrations, and to a lesser degree variation in Fe and Mg contents. The light colour variations in BSE images are linked with high Cs content occurs at grain boundaries, and secondary features such as fractures, and weaknesses in cleavage planes, particularly RSI. Lighter colour variations do not occur in patterns consistent with magmatic crystal growth, or metamorphism (i.e., concentric zonation due to primary crystal growth or diffusive re-equilibration). Due to the proximity to cleavage planes and fractures in the grain, the lighter-coloured textural variation is interpreted to be the result of post-crystallization metasomatism and the darker portion is interpreted as primary, magmatic, similar to the interpretation of

comparable textures by multiple authors (Kaeter et al., 2018; Wang et al., 2007; Xing et al., 2020).
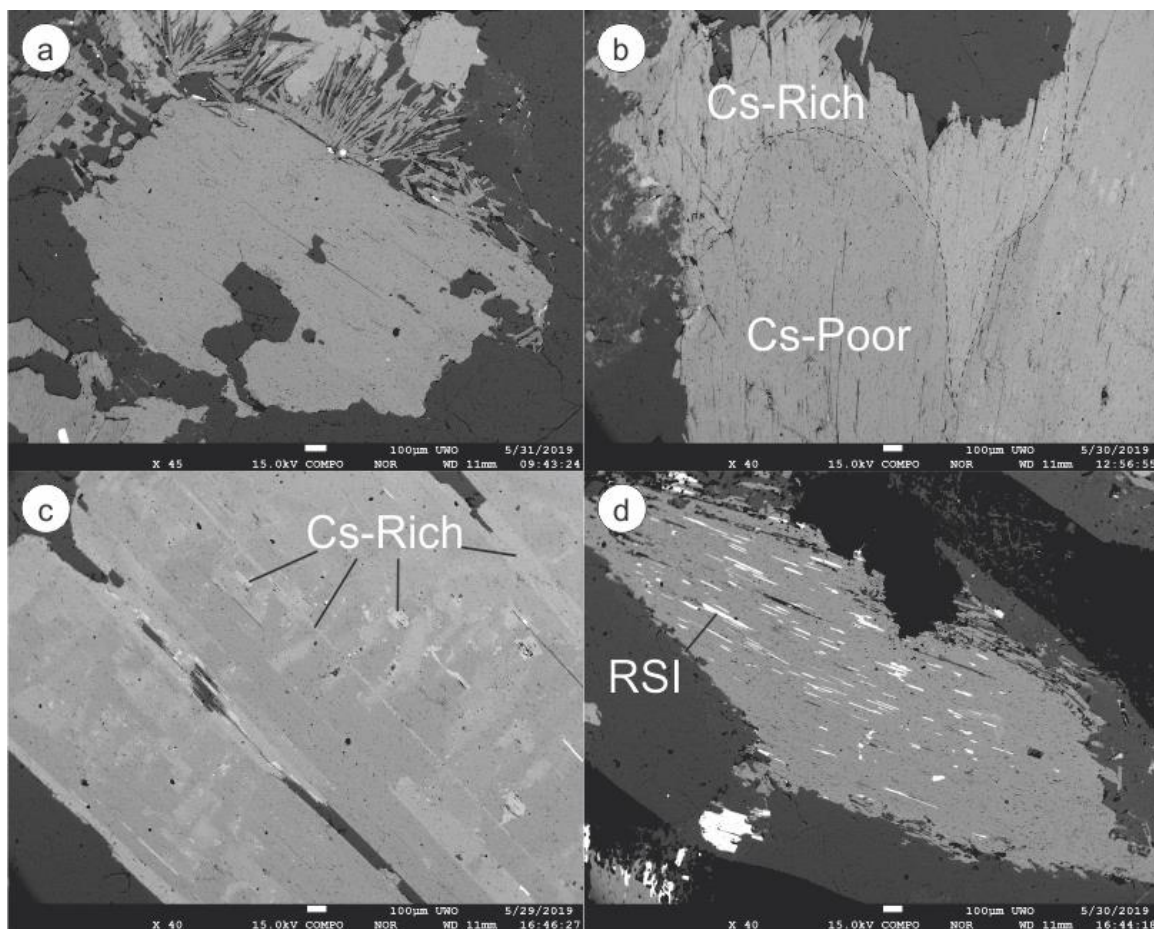
Figure 2.5: BSE imagery of muscovite with varying textures: a) poorly zoned; b) rimmed; c) patchy; d) Rod shaped inclusion (RSI) hosting muscovite

The poorly zoned white micas have limited chemical variation within the grain (Figure 2.5a), are in planar contact with other minerals (Figure 2.4a) and are interpreted to be primary magmatic. The rimmed white micas have two textural compositions: dark coloured Cs-poor cores, and lighter coloured Cs- and Fe-enriched rims (Figure 2.5b). The rims typically only envelope one or two of the edges, and rims extended into the core along fractures and cleavage planes. Consequently, the cores are interpreted to be magmatic and the rims metasomatic. The patchy white micas have the greatest variation in Cs. They can be subdivided into high Cs, moderate Cs, and low Cs (Figure 2.5c).

Patches are elongate and follow mineral cleavage and fractures, thus the darker (low Cs) is interpreted to be magmatic and the lighter (moderate to high Cs) are interpreted to be metasomatic. The white mica that hosts RSI are higher in Mg and lower in F than the other textures and the RSI are trioctahedral micas with compositions that range from Li-Cs-rich or zinnwaldite, siderophyllite to biotite. The RSI follow mineral cleavage planes and are heterogeneously distributed throughout the grain (Figure 2.5d). The darker matrix of these white micas are considered to be magmatic whereas the white RSI are metasomatic.

There are three types of spodumene identified in hand sample and thin sections, similar to those recognized by Martins et al. (2017). The most common type is euhedral to subhedral, coarse-grained crystals up to 15cm long (Figure 2.3c). The second type occurs as graphic spodumene-quartz intergrowths as medium-sized masses that average 2 to 3 cm across. The third type is interstitial spodumene, which forms in small masses interstitial to larger primary quartz and albite crystals. All three types are present in the wall, intermediate and central zone. The interstitial spodumene is more commonly found in the wall and is more rare in the central zone. Spodumene contains on average 0.84 wt% FeO, which likely explains their pale green color.

Two types of albite were identified in hand sample. The first type consists of large euhedral to subhedral crystals up to 25 cm across. These crystals are typically creamy white but can be stained salmon pink by hematization and are more common in the central zone. The second phase is finer-grained and forms anhedral masses. This type is generally hematized, particularly in the wall zone where it is commonly brick red, but locally is white. Both types are present in the intermediate zone in similar proportions and both types display polysynthetic twinning. Primary igneous grain boundaries of albite and quartz suggest cotectic crystallization.

K-feldspar is difficult to distinguish from albite in hand sample due to the hematization. However, some grains display minor perthitic textures. In thin section, K-feldspar displays tartan twinning and appears to have crystallized with albite and quartz.

The tourmaline is present as long black euhedral to subhedral crystals. Tourmaline is most common in the wall zone, with abundances decreasing towards the inner zones of the dike. In the wall zone tourmaline crystals propagate outwards from the host rock contact in comb-like structures. Tourmaline in thin section is blue and display zonation. The chemical composition of tourmaline was not determined in this study, however, owing to the black color in hand specimen it is likely schorl.

Beryl forms stubby, white, euhedral to subhedral crystal, averaging 1 to 2 cm in length. The white colour may be caused by Cs substitution (Černý and Simpson, 1978). However, beryl compositions were not determined in this study. Beryl are rarely stained by hematite, which makes beryl easier to identify in samples with strong hematization, as the surrounding feldspars are red, in contrast to the white beryl.

Apatite, Fe-Mn phosphate minerals, xenotime, and monazite are the phosphates present in minor amounts in the pegmatite dikes. Apatite is fine-grained, less than 1 mm in diameter, subhedral to anhedral and blue in hand specimen. Apatite grains are observed in the central, intermediate and wall zones. The Fe-Mn phosphate minerals (Martins et al., 2017; Benn et al., 2018b; Grammatikopoulos et al., 2020) is dark red to brown in hand specimen and occurs in fine-grain masses, less than 1cm in diameter. Fe-Mn phosphate minerals were observed in the central, intermediate and wall zones. The triphylite (Fe^{2+}) to lithiophilite (Mn^{2+}) Fe-Mn phosphate series is consistent with the described minerals and is often associated with Li-bearing pegmatites similar to the ones in this study (Černý, 2005; Černý et al., 2012). Xenotime and monazite were only identified in SEM analysis. Grains are subhedral and less than 30µm in diameter. They were observed in the central, intermediate and wall zones.

Zircon, CGM, cassiterite, and uraninite are present in trace amounts. Zircon grains are subhedral, non-zoned and less than 45 µm across. Zircon grains were observed in the central and intermediate zones. The CGM are black in hand sample, fine-grained, euhedral to subhedral as needle-shaped or anhedral crystals that are typically less than 1 mm long (Figure 2.6) and commonly cross the boundaries between quartz and feldspars grains, but not tourmaline. The concentration of CGM increase around tourmaline grains

larger than 5mm. Columbite group mineral grains are observed in all the central, intermediate, and wall zones. There are two textural types of CGM identified using BSE imaging: unzoned (Figure 2.6a-c) and zoned with Nb-rich cores and Ta-rich rims (Figure 2.6d-f). Cassiterite grains are euhedral- to subhedral, and less than 20µm in diameter. Cassiterite is observed in the central and intermediate zones. Uraninite grains are subhedral, and less than 75µm in diameter, with desiccation haloes surrounding the grains. Uraninite grains are observed in the central, intermediate and wall zones.
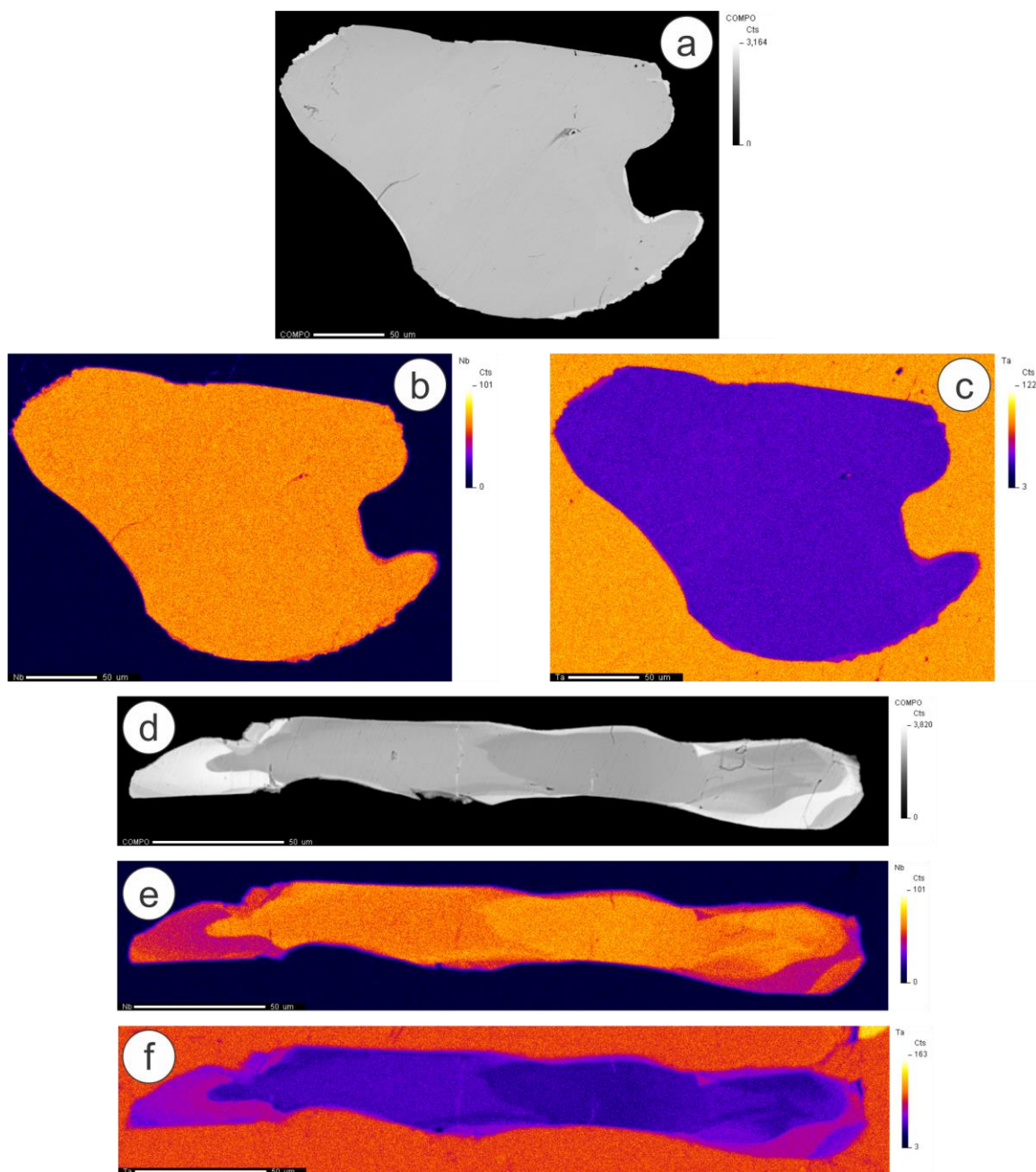
Figure 2.6: BSE and false-colouring element map of columbite-group minerals: a) BSE imagery of minimally zoned CGM b) Nb; c) Ta; d) BSE imagery of moderately zoned CGM e) Nd: f) Ta.

Arsenopyrite, chalcopyrite, pyrite, sphalerite and loellingite are trace sulphide minerals that were identified during SEM analysis. They occur as interstitial anhedral masses, less than 500 µm in length. Arsenopyrite grains are observed in the central and intermediate

zones. Chalcopyrite grains are observed in the wall zone. Pyrite grains are observed in the central and wall zone. Sphalerite and loellingite grains are observed in the intermediate zone.

2.5.2   Host Rock Lithogeochemistry

The major-, minor- and trace-element compositions of the amphibolite host rock was obtained from drill core and grab samples. This data was first reported in Benn et al. (2018b). The SiO_2 content ranges between 45.98 and 51.78 wt.% and the MgO contents range between 4.61 and 7.93 wt.% with an average Mg# (Mg/[Mg/Fe2+]x100) of 43.73 using wt% ratios. Samples plot between basalt and basaltic-andesite of a total alkalis vs silica (TAS) diagram (Figure 2.7a) and similar results on Winchester and Floyd (1977) trace-element volcanic rock classification (Figure 2.7b). The chondrite-normalized rare-earth element (REE) profiles are relatively flat, typical of the normal mid-ocean ridge basalts (N-MORB) (Figure 2.7c). A similar interpretation can be made plotting samples on a Pearce and Cann (1973) Ti-Zr-Sr Basalt classification ternary plot (Figure 2.7d). These data support previous interpretations (NATMAP Shield Margin Working Group, 1988; Syme et al., 1999) that the amphibolite host rock is metamorphosed MORB.

Two samples of amphibolite have εNd values of +3.8 and +2.8 at 1900 Ma (Manitoba Geological Survey, 2020), indicative of juvenile-mantle derivation. These results are in agreement to what has previously been measured in basalt in the Snow Lake area (Manitoba Geological Survey, 2021).
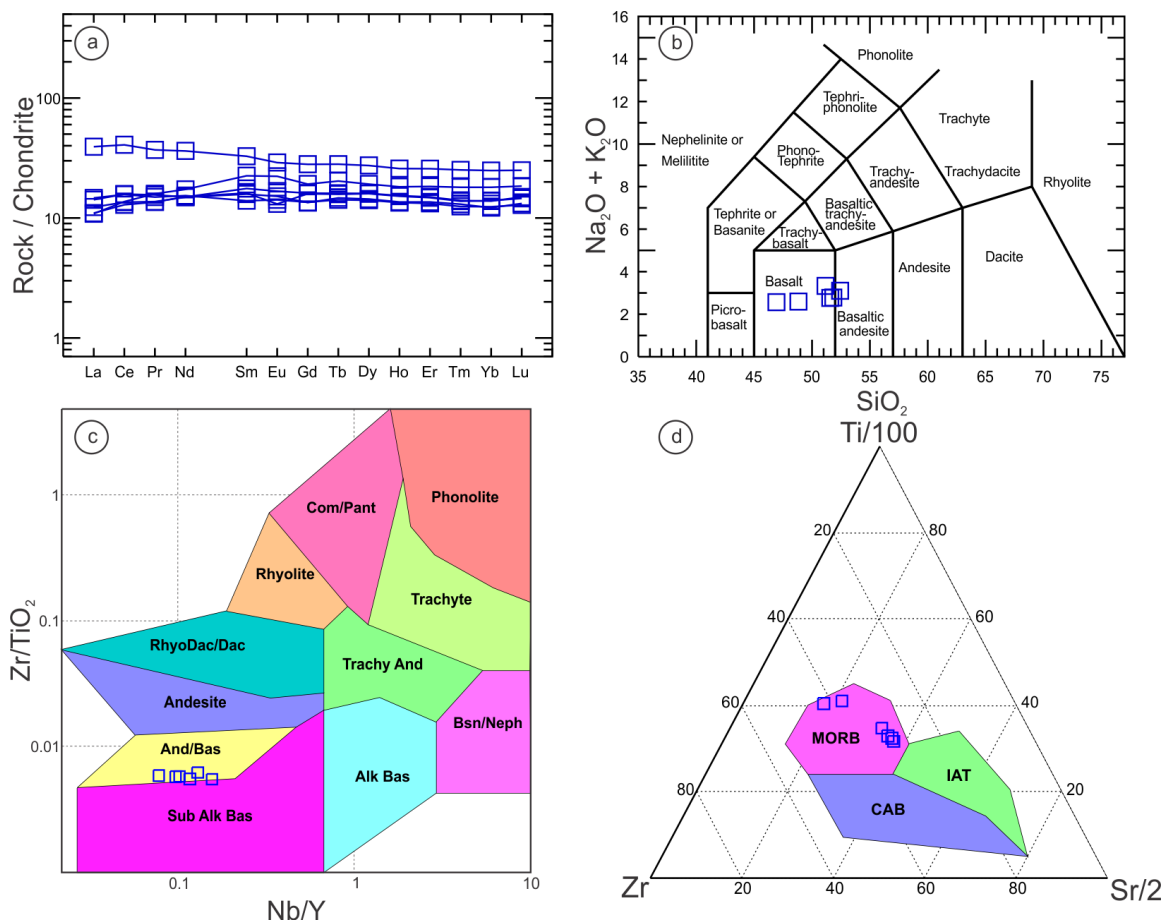
Figure 2.7: Major- and trace-element diagrams for the mafic volcanic host rocks a) total alkalis versus silica (TAS) diagram; b) Volcanic rock classification from Winchester and Floyd, 1977; c: chondrite normalized REE spider diagram (Chondrite normalized to McDonough and Sun, 1995); d) Basalt Ti-Zr-Sr classification from Pearce and Cann, 1973.

2.5.3   Geochronology

The pegmatite dikes were dated using in-situ isotopic U-Pb analyses of CGM. Samples from Dike 1 produced a concordia date of 1793 ±14Ma with a mean square of weight deviates (MSWD) of 0.049 and samples from Dike 8 produced a concordia date of 1764 ±9.3Ma with a MSWD of 2. Combined results gave a concordia date of 1780 ±8.1Ma with a MSWD of 1.6 (Figure 2.8; Martins et al., 2019). All dates obtained are within the

error ranges of each other, therefore the combined age of 1780 Ma is considered the date of emplacement for the Wekusko Lake pegmatites. These ages dates are also reported in Benn et al. (2019).
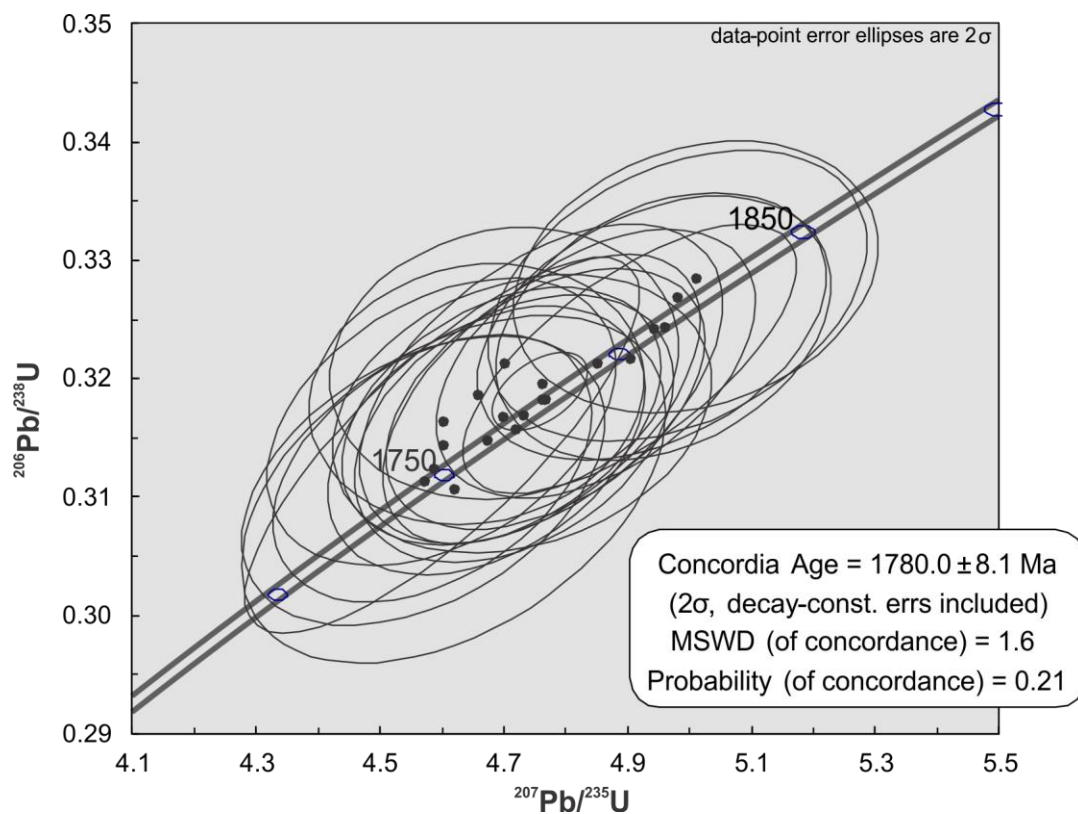
Figure 2.8: Concordia diagram for all data combined from CGM of pegmatites in the Wekusko Lake pegmatite field.

Table 2.1: High Resolution Integrates EMPA (SiO$_2$, Al$_2$O$_3$, TiO$_2$, FeO, MgO, Na$_2$O, K$_2$O, F) and LA-ICP-MS (Mn, Ba, Li, Rb, Cs, Be, Nb, Sn, Ta, Tl) analysis results from Dike 1. Structural Formulae of white micas (APFU) calculated based on 44 cation charges and 22 oxygen charges

Sample	16-5-21 c2g1a	16-5-43 c1g1c	16-6-22 c1g1b	16-4-86 c2g1a	17-10-180 c2g1b	17-10-192 c1g1b	16-7-188 c1g1a	18-20-157 c1g1c
Dike	1	1	1	1	1	1	1	1
Zone	Wall	Wall	Intermediate	Intermediate	Intermediate	Central	Central	Central
Texture	Poorly Zoned	Rimmed	Poorly Zoned	Rimmed	Patchy	Poorly Zoned	Patchy	RSI
SiO2	44.62	44.26	44.64	44.50	43.77	44.34	44.26	45.14
Al2O3	35.23	33.02	34.52	36.18	35.08	35.05	35.01	35.86
TiO2	0.10	0.09	0.10	0.11	0.20	0.03	0.07	0.11
FeO	3.42	5.11	4.00	2.92	3.73	3.49	3.31	3.35
MnO	0.12	0.33	0.21	0.16	0.15	0.17	0.38	0.04
MgO	0.20	0.15	0.11	0.17	0.12	0.10	0.12	0.30
BaO	0.00	0.00	0.00	0.00	0.00	0.00	0.00	0.00
Li2O	0.79	1.46	0.82	0.86	0.60	0.73	0.53	0.47
Na2O	0.46	0.27	0.33	0.52	0.36	0.39	0.34	0.43
K2O	10.64	10.58	10.59	10.37	10.43	10.44	9.96	10.35
Rb2O	1.07	1.40	1.29	0.90	1.70	1.82	1.53	1.12
Cs2O	0.06	0.06	0.07	0.04	0.15	0.12	0.06	0.04
F	0.602	1.255	0.62	0.942	0.399	0.753	0.55	0.285
subtotal	97.30	97.98	97.29	97.66	96.71	97.45	96.11	97.50
O=F	-0.25	-0.53	-0.26	-0.40	-0.17	-0.32	-0.23	-0.12
Total	97.05	97.45	97.03	97.26	96.54	97.13	95.88	97.38
Structural Formula on the basis of 22 oxygen atoms								
Si	5.99	6.00	6.01	5.93	5.94	5.98	6.01	6.00
Ti	0.01	0.01	0.01	0.01	0.02	0.00	0.01	0.01
Al	5.53	5.28	5.48	5.68	5.61	5.58	5.60	5.62
AlIV	2.00	1.99	1.98	2.06	2.04	2.01	1.98	1.99
AlVI	3.53	3.29	3.51	3.62	3.57	3.56	3.62	3.63
Fe	0.44	0.58	0.45	0.33	0.42	0.39	0.38	0.37
Mn	0.02	0.04	0.02	0.02	0.02	0.02	0.04	0.01
Mg	0.04	0.03	0.02	0.03	0.02	0.02	0.02	0.06
Ba	0.00	0.00	0.00	0.00	0.00	0.00	0.00	0.00
Rb	0.10	0.12	0.11	0.08	0.15	0.16	0.13	0.10
Cs	0.00	0.00	0.00	0.00	0.01	0.01	0.00	0.00
Li	0.38	0.79	0.44	0.46	0.33	0.39	0.29	0.25
Na	0.11	0.07	0.09	0.14	0.10	0.10	0.09	0.11
K	1.81	1.83	1.82	1.76	1.81	1.80	1.73	1.76
F	0.28	0.54	0.26	0.40	0.17	0.32	0.24	0.12
Sum	20.25	20.57	20.21	20.51	20.21	20.35	20.14	20.02
X total	2.02	2.03	2.02	1.98	2.06	2.06	1.95	1.97
Y total	4.42	4.74	4.45	4.47	4.39	4.39	4.36	4.33
Rare metal elements (ppm)								
Li	3660	6760	3787	3989	2809	3376	2483	2181
Be	25.6	40.3	35.9	46.8	109.3	123	56.3	38.9
Nb	821	1128	919	957	951	744	862	910
Sn	783	767	965	598	1009	1099	1122	776
Ta	75.5	110.5	132.5	88.2	283.8	287	136.3	92.4
Tl	50.7	66.1	60.9	39	67.9	71.6	70	45.6
Rb	9800	12830	11820	8190	15530	16610	13970	10280
Cs	521	598	634	373	1460	1175	532	357.2

2.5.4   White mica chemistry

Result from EPMA and LA-ICP-MS are reported in Table 2.1. Average white mica grain stoichiometry was calculated based on a 44 cation charges (Table 2.1). The single grain

averages from all dikes were plotted on the Tischendorf et al. (2007) mica classification atoms per formula unit (apfu) diagram, FeAl vs. MgLi (Figure 2.9a, b). All Fe (apfu) is assumed to Fe^{2+}. All grains plot in the white mica field and show a trend of increasing Li and Fe+Mn+Ti and the trend for the magmatic grains is steeper, more towards the zinnwaldite end member than the metasomatic micas, which trend more toward the polylithionite end member (Figure 2.9a, b); Tischendorf et al., 2007).
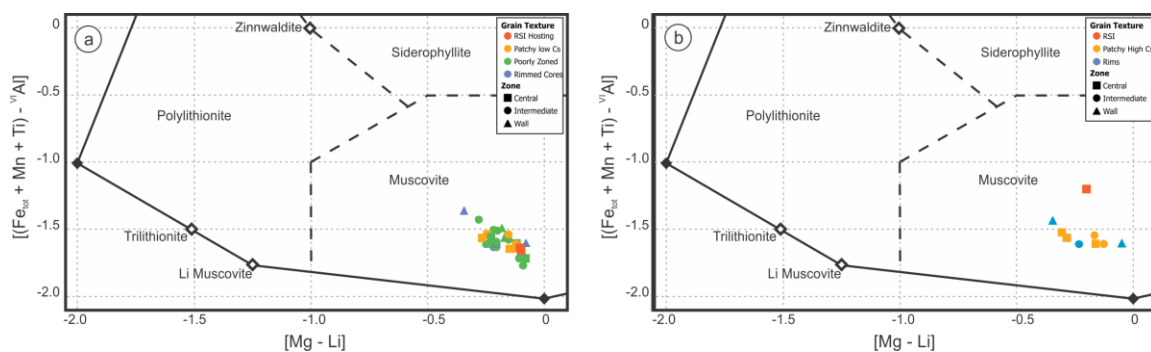
Figure 2.9: Classification scheme for micas Fe-Al vs Mg-Li in apfu (after Tischendorf et al., 2007). Calculated apfu values were halved to fit the classification scheme calculated at 10 oxygens and 2 (OH, F) apfu. Filled diamonds represent endmember composition; Hollow diamonds represent ideal member composition; a) average composition of magmatic components of muscovite grain; b) average composition of metasomatic components of muscovite grains.

Figure 2.10a shows that there is a negative correlation between Li and octahedral Al (^{IV}Al) for all mica types, and that magmatic white micas (slope = -0.53) have a different trend from metasomatic white micas (slope = -0.32). Figure 2.10b shows a weak positive correlation between apfu Li and tetrahedral Al (^{VI}Al), with no apparent differences between magmatic and metasomatic white mica trends. There is no correlation between Fe and Ti and Li, but there is a positive relationship between Mn and Li (Table 2.1), suggesting that both have substituted for Al in the octahedral sites of white mica.
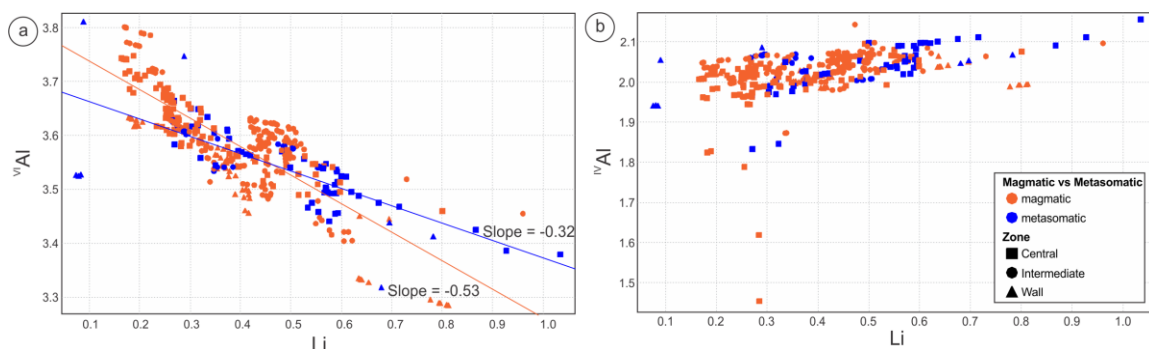
Figure 2.10: Lithium and Al substitutions in muscovite: A) Li vs. ^{VI}Al; B) Li vs. ^{IV}Al. All values in apfu. Red: magmatic analyses; Blue: metasomatic analyses. Squares: central zone; Circles: intermediate zone; Triangles: wall zone.
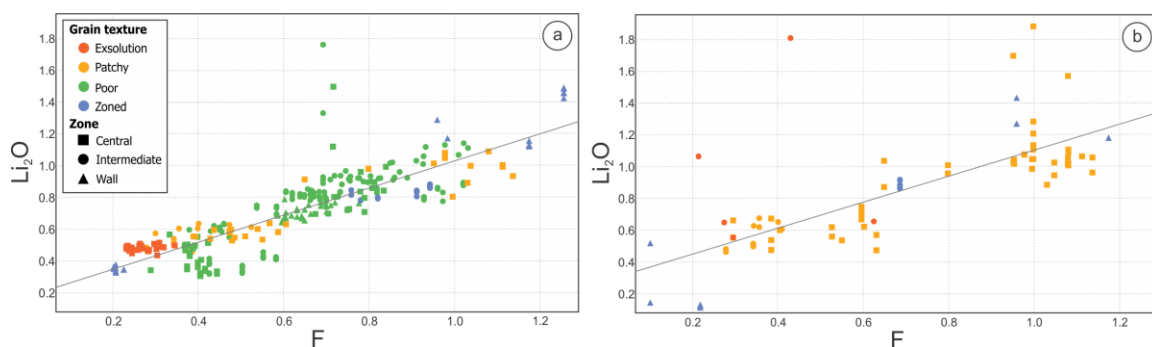
Figure 2.11: Muscovite chemistry result of Li_2O vs. F (wt%) comparison of Dike 1 by: a) magmatic analyses b) metasomatic analyses., Grey line is linear regression of all data. Magmatic line $Li_2O = 0.85*F+0.17$ ($R^2=0.71$). Metasomatic Line $Li_2O = 0.82*F+0.31$ ($R^2=0.55$).

There is a clear positive correlation between Li_2O and F (Figure 2.11a, b). This relationship is expected as F is typically used to estimate the Li content of micas when Li is not measured (Tindle and Webb, 1990; Linnen and Williams-Jones, 1995). For the white mica in Dike 1 the Li_2O content can be estimated with the equations below, a similar estimation to those made in previous literature (Tindle and Webb, 1990; Tischendorf et al., 1997; Van Litchervelde et al., 2008).

1) Magmatic: $Li_2O = 0.85F + 0.17$ ($R^2=0.71$) (Figure 2.11a)
2) Metasomatic: $Li_2O = 0.82F + 0.31$ ($R^2=0.55$) (Figure 2.11b)

There is no clear correlation between Li enrichment of the white mica and pegmatite zones (Figure 2.12a). The average values of white mica grains by zone are: Wall 0.75 ($\pm$0.6 2σ) wt% Li_2O; Intermediate 0.76 ($\pm$0.5 2σ) wt% Li_2O; Central 0.72 ($\pm$0.6 2σ) wt% Li_2O. Rimmed white mica grains have the highest average Li_2O (0.82 wt%) content with cores being more Li_2O rich, followed by patchy (0.79 wt%), poorly zoned grains (0.72 wt%), and grains that host RSI have the lowest Li_2O (0.57 wt%) content (Figure 2.12b). The lower Li content of these micas is potentially explained by partitioning of Li into the trioctahedral inclusions, which have an average Li_2O concentration of 0.97 wt%. Whereas there are differences in the Li contents of different textural locations in single grains, i.e., cores versus rims, matrix versus RSI, the Li content within a textural domain of an individual white mica grain varies little. White mica grains taken from drill core samples containing spodumene tend to have a higher Li_2O content (Figure 2.12c). White mica grains from samples with spodumene have an average Li_2O of 0.82$\pm$0.52 wt% and white mica grains from samples without spodumene have an average Li_2O of 0.64$\pm$0.50 wt%. However, there is a significant overlap between the two populations. This overlap is likely caused by sample bias where spodumene is not present within the 2D representation provided by drill core but is present within the 3D space surrounding the analysed grain. There are minimal differences in the range and averages of Li_2O contents of magmatic versus metasomatic white mica grains (Figure 2.11a, b).
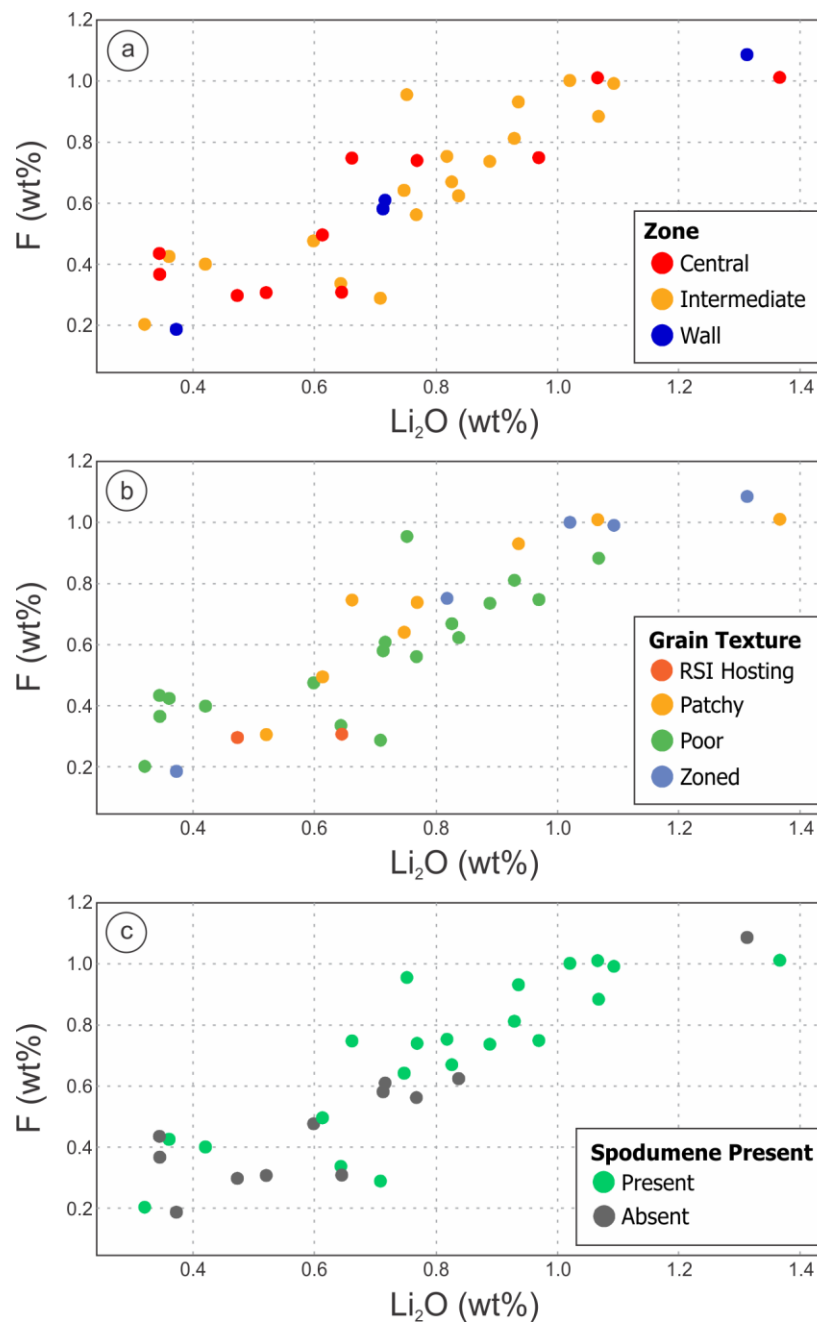
Figure 2.12: Averaged muscovite grain chemistry results Li_2O Vs. F (wt%) by a) Pegmatite zone: Wall (red), Intermediate (yellow), Central (blue); b) Muscovite backscatter imager texture: Poorly zoned (green), RSI-hosting (red), Patchy (yellow), Rimmed (cyan); c) Spodumene present in core sample: Spodumene present (green), No spodumene present (grey).

The K/Rb ratio vs Cs ppm (K from EPMA; Rb, Cs from LA-ICP-MS) compositions of micas are plotted on Figure 2.13 a, b. The spot analyses of all white mica range from 291 ppm to 11500 ppm Cs and the K/Rb ratio ranges from 13.7 to 3.8. White mica grains that are more heterogeneous, such as the metasomatic portions of patchy grains, show a much greater variation in Cs content than in K/Rb (Figure 2.13b). Magmatic white mica analyses range from 308 ppm to 6270 ppm Cs and 13.7 to 4.2 K/Rb ratio. Metasomatic white mica analyses range from 291 ppm to 11500 ppm Cs and from 10.3 to 3.8 K/Rb ratio. With decreasing K/Rb there is an increase in Cs, Tl, and Ta (Figure 2. 14a-d) and a decrease in the Nb content of white micas (Figure 2.14e, f). Clusters which fall outside the trend to the right of the curve (Figures 2.13 & 2.14) are from one sample (16-4-86 C1). It has elevated Mn, Mg, and Li content and lower ^{VI}Al. There are no petrographic abnormalities within this grain that explain the anomalous behaviour.
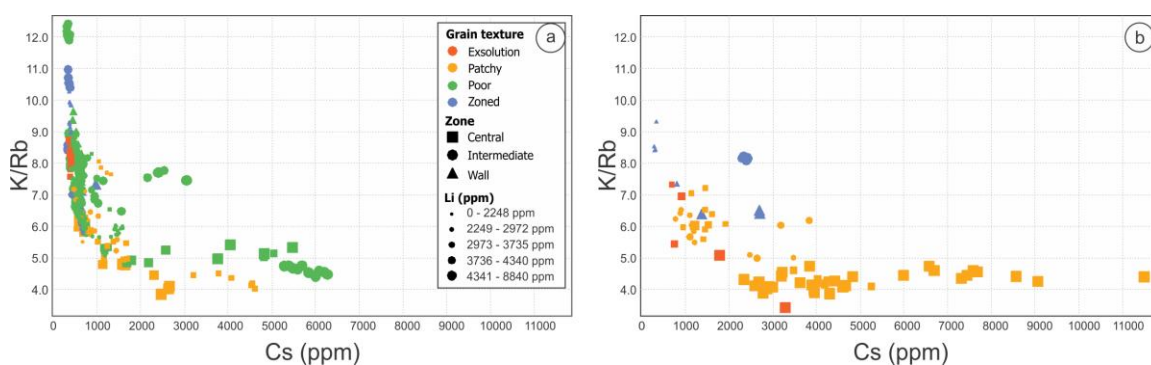
Figure 2.13: Muscovite chemistry results K/Rb vs Cs (ppm) a) all data, dot size increases with Li_2O concentrations in grain; b) magmatic analysis.
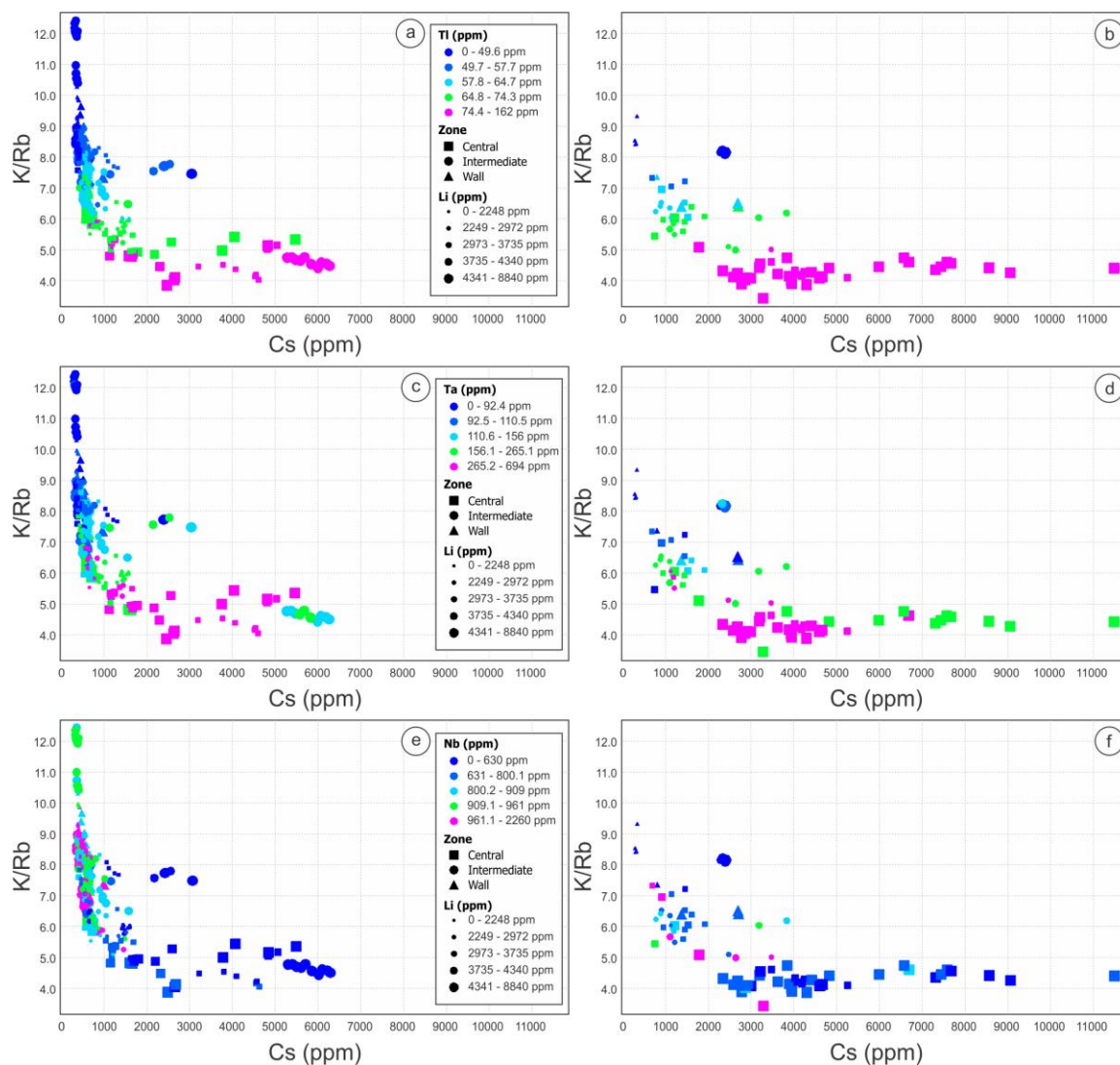
Figure 2.14: Muscovite chemistry results K/Rb vs Cs (ppm) with element concentration heat map. Heat map shows lowest concentrations in blue and highest concentrations in pink a) Tl magmatic; b) Tl metasomatic; c) Ta magmatic; d) Ta metasomatic; e) Nb magmatic; f) Nb metasomatic. Symbol size is increases with Li$_2$O content.

Most of the white mica grains have elevated Nb and Ta contents (Figure 2.15a, b). The Nb content ranges from 111 ppm to 2260 ppm, with an average of 796 ppm Nb (Figure 2.15a). The micas from the wall zone are the most enriched in Nb, and the average Nb contents decrease slightly towards the central zone. The wall zone micas have an average of 860 ppm and the central zone has an average of 743 ppm Nb. The Ta contents range from 8 ppm to 694 ppm, with an average of 178 ppm Ta (Figure 2.15b). The central zone

is the most enriched in Ta, and the Ta contents decrease towards the wall zone (the distribution of Sn, not shown, is very similar to Ta). The central zone has an average of 236 ppm and the wall zone has an average of 95 ppm Ta. The relative change of Ta is greater than that of Nb, thus the Nb/Ta ratio ranges from 9.6 in the wall zone to 6.6 in the intermediate zone and 4.8 in the central zone. It should be noted that the presences of CGM can influence the Nb/Ta concentrations of the micas. White mica grains in samples that also contain CGM have on average a higher Nb and lower Ta contents. These white mica grains have an average of 832 ppm Nb, 148 ppm Ta and a Nb/Ta ratio of 7.3. White mica grains in samples without CGM have an average of 655 ppm Nb, 292 ppm Ta and a Nb/Ta ratio of 2.7. There are no significant variations in Ta, Nb, Sn, and Tl with relation to magmatic or metasomatic white mica grains.
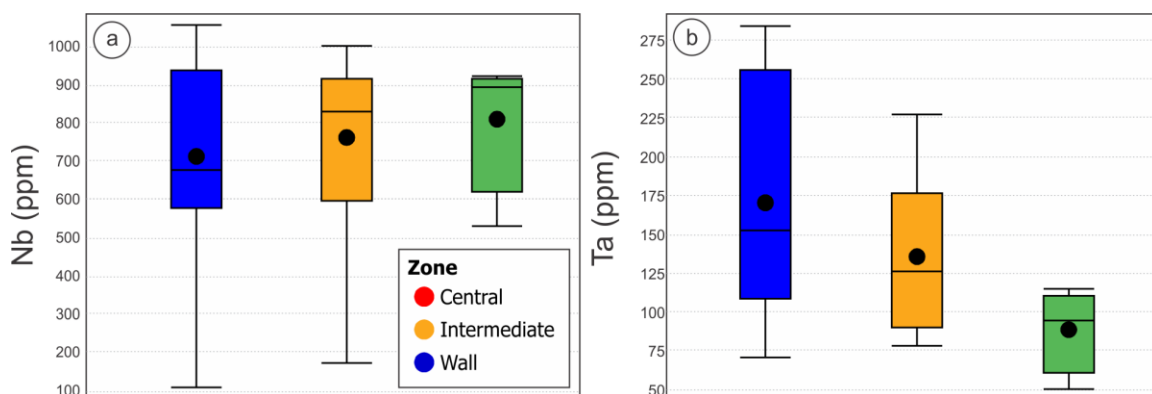
Figure 2.15: a) Nb, and b) Ta variation between pegmatite zones in Dike 1.

2.6   Discussion

2.6.1   Controls on emplacement of dikes and implications on the tectonic setting

It is commonly assumed that pegmatites and related granitic intrusions are emplaced during extension where the crust opens up to make space (Gay, 1980; Zobach and Zobach, 1980). However, this is rarely the case (Brisbin, 1986). The dominate state of stress in the crust is overall compressional, but these forces are commonly misaligned

leading to transpressional regimes and consequently extension occurs (Gay, 1980; Zoback and Zoback, 1980). Pegmatite dikes are formed where the pressure of the intruding magma overcomes the compressional stress and tensile strength of the rock. Transpressional zones of extension or shearing provide planes of lower compressional forces for dikes to intrude. The host rock and the rheological state of the host rock also have an important role in emplacement of the pegmatite dike. The effect of host rock tensile strength can be observed in Wekusko Lake where the host of Dike 1is 10 m thick in amphibolite, but rapidly decreases to 10 cm at the contact with gneiss.

The Wekusko Lake pegmatite dikes have a podiform and lens-shaped morphology, which is common in dikes emplaced in brittle to ductile transition zones (Brisbin, 1986). The dikes in Wekusko Lake crosscut foliation and gneissosity of host rocks, and do not occur in faults or shear zones. Therefore, the orientation is interpreted to have been caused by an anisotropic force parallel-subparallel to the trend of the dikes. D4 is the only deformation event in Wekusko Lake considered to be brittle-ductile (Černý et al., 1981; Lucas et al., 1994; Connors et al., 1999) (D3 is Northwest trending transpressional shortening) and the orientation of the dikes was controlled by planes of weakness and anisotropic forces.

The emplacement age of 1.78 Ga constrains the formation of the dikes to be after D2, peak metamorphism dated at 1.81Ga and before craton stabilization at 1.70 Ga (Schneider et al., 2007; Hammer et al., 2010). Neither D3 or D4 have been dated but both events occur between 1.81 Ga and 1.70 Ga. Based on the conditions above, it is suggested that the pegmatite dikes in Wekusko Lake are linked to the D4 northwest trending brittle-ductile deformational phase. If the folding present in the dikes is caused by late D4 compression, then the age of the pegmatites also represents a maximum age for late stage D4 deformation.

A thermal peak at 1.77 Ga with associated mid-crustal melting has been interpreted by Schneider et al. (2007). These authors believe that it is related to rapid crustal extension and unroofing rather than having been linked to slow cooling following peak metamorphism. This could have led to white mica dehydration and decompression

melting (Kraus and Menard, 1997). Although there is no formal connection between the crustal extension and decompression melting events the similarity of the ages and nature of events suggest a link.

2.6.2   White Mica Geochemistry

The white mica in this study shows a trend of increasing Li with decreasing Al^{VI} (Figure 2.10a). This trend suggests white mica has undergone Li fixation (Munoz, 1968; Monier and Robert, 1986): $Al^{VI},\square^{VI}\leftrightarrow(M^{2+})^{VI},Li^{VI}$, where M^{2+} is an octahedral divalent cation, most commonly Fe, Mg, and Mn and $\square$ is an octahedral vacancy. This results in an increase in octahedral cations and leaves the tetrahedral layer unchanged. As a result, M^{2+} cations and Li can be plotted against the number of trioctahedral cations (Figure 2.16a-c). This is used to determine which M^{2+} cations are fixed to the octahedral site with Li. The substitution of Fe into the M^{2+} cation with Li does not correlate 1:1 with the trioctahedral cations (Figure 2.16a) and there is no variation in the trends in relation to magmatic and metasomatic grains. This suggests Fe enrichment cannot be completely explained via Li fixation. Both Mn and Mg with Li (Figure 2.16b; c) have a nearly 1:1 correlation with trioctahedral cations in the magmatic grains. This correlation is maintained when both are plotted with Li against trioctahedral cations (Figure 2.16d). Magmatic grains follow closer to the 1:1 correlation than the metasomatic grains when plotting Mn and Mg (Figure 2.16b-d). This suggests an alternate enrichment substitution for Fe. An alternate method for enriching Fe within a mica is phengitic substitution, $Al^{VI},Al^{IV}\leftrightarrow Mg^{VI},Si^{VI}$, coupled with Fe$\leftrightarrow$Mg substitution (Foster, 1956; Monier and Robert, 1986; Brigatti et al., 1998; Schmidt et al., 2001). This does not affect the total number of trioctahedral cations. When plotting $Al^{IV}+Al^{VI}$ against Si+Fe (Figure 2.16e), the slope is near -1, which supports this as a substitution mechanism for enriching Fe in white mica. The two proposed substitutions can be combined into a single larger equation $Al^{IV}+(Al^{VI})_2\leftrightarrow Li+Si+Fe+(Mn,Mg)$ (Figure 2.16f). Micas plotted on this a graph using this equation also have a slope near -1.
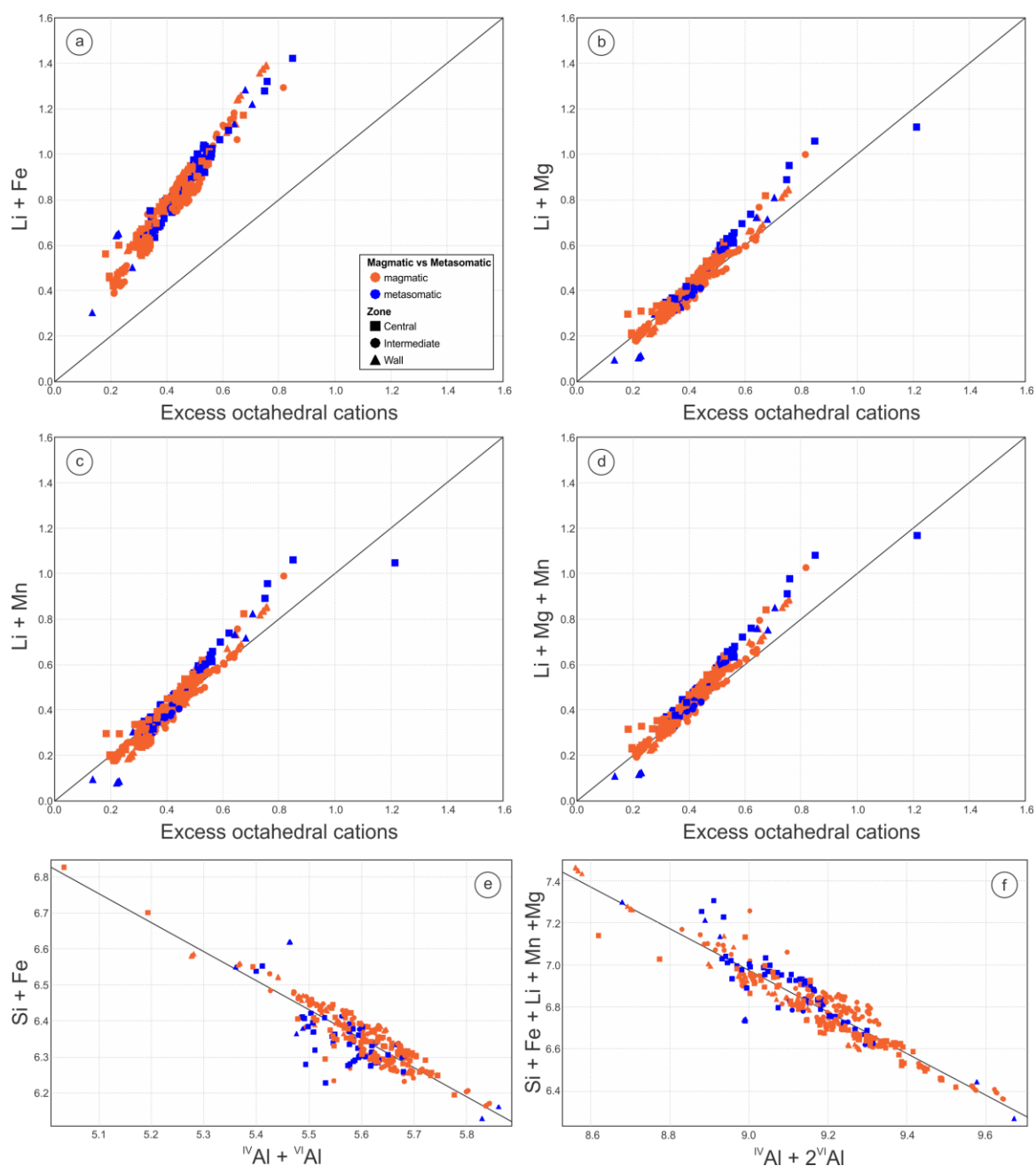
Figure 2.16: Potential substitution mechanisms in muscovite. A) Li+Fe vs trioctahedral cations; b) Li+Mg vs trioctahedral cations; c) Li+Mn vs trioctahedral cations; d) Li+Mn+Mg vs trioctahedral cations; e) Si+Fe vs $^{IV}Al+^{VI}Al$ Line of regression slope = -0.8, R^2=0.88; f) Li+Si+Fe+(Mn+Mg) vs $^{IV}Al+2^{VI}Al$. Line of regression slope = -0.99.

$R^2 = 0.91$. Grey lines show linear regression of all data. Black lines show a slope of 1 through the origin.

This substitution mechanism does not fully explain the varying slopes between magmatic and metasomatic grains observed when plotting excess octahedral cations vs $Li+M^{2+}$ (Figure 2.16). A similar observation from a plot of Li vs Al^{VI} (Figure 2.10). There are three apparent trends, two magmatic parallel trends which plot close to the ideal slope of -1, and a metasomatic trend which does not (Figure 2.17a). The two magmatic trends are distinguished between high and low F. A similar observation is made when Li is plotted vs octahedral M^{2+} cations (Figure 2.17b). Both magmatic trends follow a close to ideal slope of -1, whereas metasomatic grains trend has a shallower slope. This suggests a method of Li-enrichment without M^{2+} enrichment in metasomatic white mica grains.
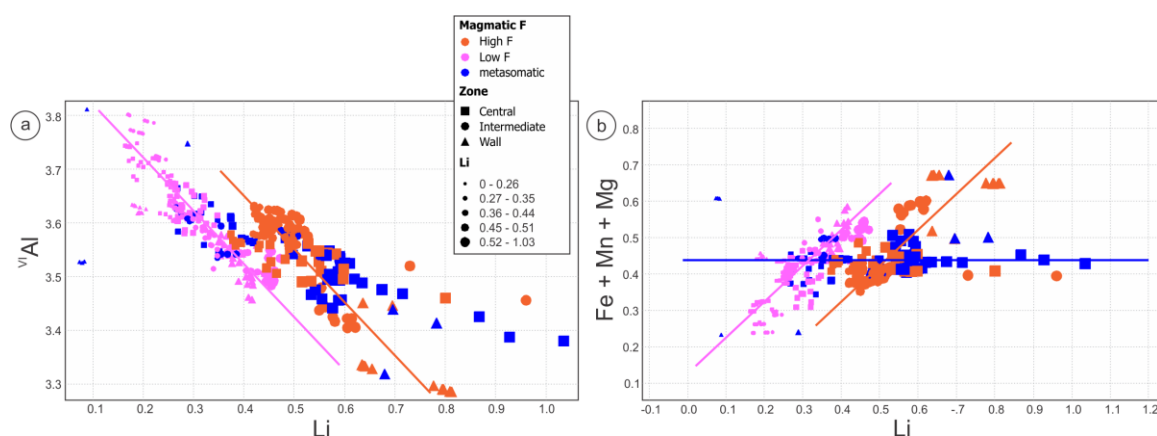
Figure 2.17: a) ^{VI}Al vs Li (APFU) low F (pink) micas plot close to slope of -1 (pink line), which differs from High F and metasomatic analyses; b) divalent cations vs Li (APFU) shows 3 trends: Low F (Pink) and High F (Red) with slopes close to 1 and Metasomatic (blue) with slope close to 0.

Icenhower and London (1997) investigated F partitioning between biotite and silicate melt and suggested that a F-O exchange may occur during deprotonation reactions: $[Fe^{2+}OH]^+_{bt} \leftrightarrow [Fe^{3+}O]^+_{bt} + 0.5H_{2\ melt}$. The data in this study suggest a similar reaction involving deprotonation and F substitution may take place in metasomatic white mica.

$$[^{VI}Fe^{2+}OH]^+ + {}^{VI}\square = [^{VI}Fe^{3+}O]^+ + {}^{VI}Li^+ + {}^{OH}F^-$$

Charge balance is maintained during deprotonation adding Li to the vacant octahedral site is balanced by adding F to an OH site. This would explain the horizontal trend on Figure 2.17b, where the total Fe+Mg+Mn is constant but the amounts of Li (and by inference F) increase. Testing this hypothesis would require in situ Fe^{2+}/Fe^{3+} analysis of the micas, which outside the scope of this study. However, it is interesting to note that in a micro-XANES study of white micas in metapelites, white micas have the highest Fe^{3+}/Fe^{2+} ratios (Dyar et al., 2002) of any mineral in the metamorphic assemblage, thus Fe^{3+} in white mica is a reasonable interpretation. The hematization observed indicates that oxidation did occur, and if this event was synchronous with the metasomatic crystallization of the white mica the above equation could explain the geochemical differences between the magmatic and metasomatic analyses.

2.6.3   Mica evolution and pegmatite fractional crystallization modeling

The evolution of granitic melts is commonly tracked using the contents of incompatible elements in rocks and minerals during fractional crystallization (Joliff et al., 1987; Roda et al., 1995; Wise, 1995). White mica is particularly well suited to record increases of the contents of Cs, Rb, Tl, Ta, Nb and Li during crystallization (Joliff et al., 1987; Roda et al., 1995; Wise, 1995). Figure 2.13 shows that Cs concentrations increase with decreasing K/Rb, which is interpreted to reflect increasing evolution (Černý et al., 1981; Roda et al., 1995). Other incompatible elements such as Tl, Li, and Ta have been used to show similar evolution trends (Roda et al., 1995; Wise, 1995; Wise and Brown, 2010). Within the context of Dike 1, grains from the wall zone are, on average, are least evolved and range from primitive to moderately evolved (Figure 2.13). Grains from the intermediate zone also range from primitive to evolved. Grains from the central zone are on average evolved and range from primitive to evolved (Figure 2.13). This suggests the dike crystallized from the wall zone inward. Texturally, the poorly zoned white mica grains range from primitive to evolved. Whereas white mica grains that host RSI are generally less evolved and the patchy zoned grains are more evolved. When compared to white

mica from other LCT pegmatites (Figure 2.18), Wekusko Lake white mica grains are moderately evolved. Dike 1 plots slightly less evolved than the Tanco pegmatite, Canada (Van Lichtervelde et al., 2007) and more evolved than the Bailongshan LCT pegmatite, China (Xing et al., 2020).
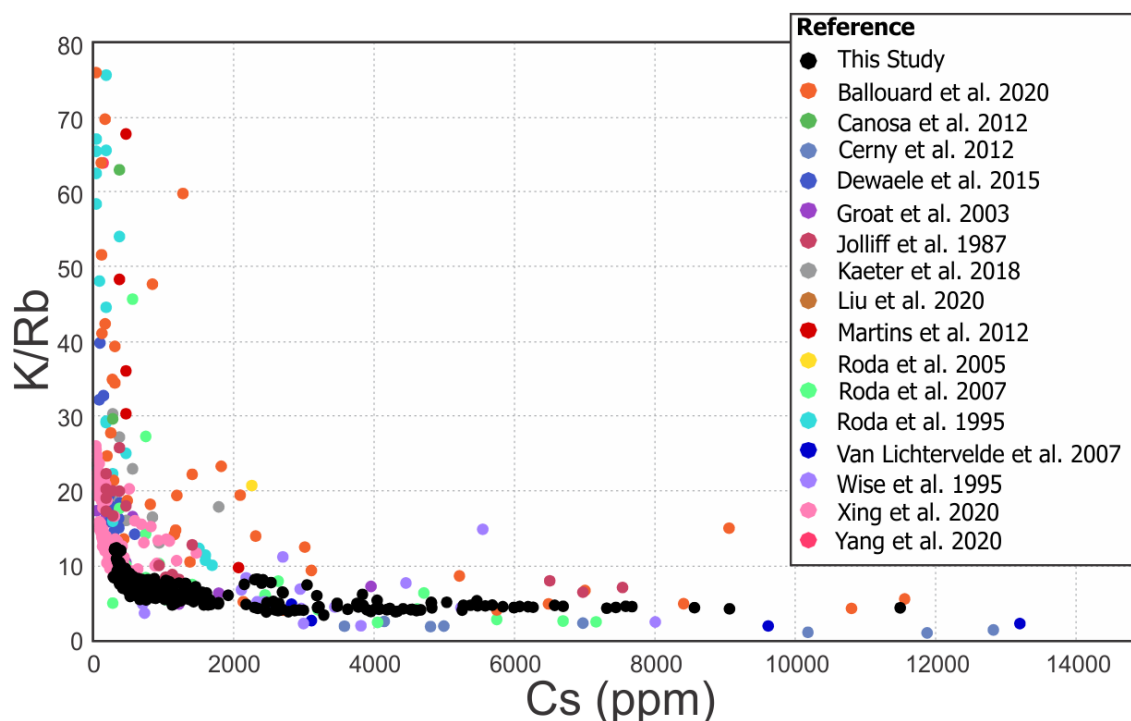
Figure 2.18: Muscovite chemistry results of Dike 1 (Black) plotted with a compilation of mica found in pegmatites around the world (Ballouard et al., 2020; Canosa et al., 2012; Černý et al., 2012; Dewaele et al., 2015; Groat et al., 2003; Joliff et al., 1987; Kaeter et al., 2018; Liu et al., 2020 (Tibet); Martins et al., 2012 (Portugal); Roda et al., 1995; Roda et al., 2005; Roda et al., 2007; Van Litchervelde et al., 2007 (Canada); Wise et al., 1995; Xing et al., 2020; Yang et al., 2020). Outliers outside of plotted area are: 3 points from Roda et al., 1995 (<90 K/RB and >100ppm Cs); 1 point from Roda et at., 2007 (<190 K/Rb and >600ppm Cs); 4 points from Černý et al., 2012 (>0.3 K/Rb and <20000ppm Cs).

Table 2.2: Mineral mass fraction of S-type granite (Chakraborty and Upadhyay, 2020) and Dike #1 pegmatite; Kd values for muscovite (Ms): Philpotts and Schetzler (1970), and Icenhower and London (1995) (K, Rb, Cs);Kd values for tourmaline (Tur): Van Hinsberg (2011) (K, Rb, Cs); Kd values for K-feldspar (Kfs): Philpotts and Schetzler (1970) (K), Long (1978) (Rb), and Icenhower and London (1995) (Cs);Kd values for garnet (Grt): Philpotts and Schetzler (1970) (K, Rb, Cs); Kd values for biotite (Bt): Higuchi and Nagasawa (1969) (K), Philpotts and Schetzler (1970) (Rb), Icenhower and London (1995) (Cs); Kd values for quartz (qz): Nash and Crecraft (1985) (K, Rb, Cs); Kd values for plagioclase (Pl): Philpotts and Schetzler (1970) (K), and Nash and Crecraft (1985) (Rb, Cs).

Mineral	S-type granite		Ms	Tur	Kfs	Grt	Bt	Qz	Pl	Benn	Ms	Tur	Kfs	Grt	Bt	Qz	Pl
zone								X (mineral mass fraction)									
wall			0.07	0.13	0.18	0.06	0.17	0.25	0.14		0.05	0.04	0.2	0.001	0.008	0.37	0.38
intermediate			0.17	0.11	0.18	0.05	0.1	0.25	0.14		0.1	0.03	0.15	0.001	0.0075	0.37	0.38
Central			0.18	0.07	0.19	0.055	0.1	0.27	0.14		0.15	0.2	0.1	0.001	0.007	0.37	0.38
elements	Co S-type granite (ppm)	Co Pegmatite (ppm)				Kd (partition coefficient)											
K	35000	34334	2.54	0.19	1.49	0.01	2.5	0.01	0.26								
Rb	220	4015	1.75	0.3	1.1	0.01	0.94	0.04	0.13								
Cs	16	2111	0.16	0.06	0.13	0.01	0.28	0.03	0.18								

Table 2: parameters for Rayleigh fractionation modelling

The white mica grain analyses were compared to a Rayleigh-type fractional crystallization model of a theoretical typical S-type granite (Table 2.2) to determine the degree of crystallization required to obtain the concentrations of trace elements observed in the white mica. The quantitative "finite-step" approach was used to account for changes in the mineral-melt partition coefficients and mineral proportions during different stage of crystallization (Hertogen and Gijebels, 1976; Hulsbosch et al., 2014). It should be noted that partitioning coefficients are dependent on the physicochemical conditions of the geological system, which are rarely known (Pan, 1977). It is assumed that the partition coefficients do not change throughout crystallization. The basic mathematic formulation of Rayleigh Fractionation is:

$$(1)\ \frac{C_i^{Liq}}{C_{0,i}^{Liq}} = (1 - F)^{(D_i - 1)}$$

Where $C_{0,i}^{Liq}$= initial concentration of element 'i' in parent melt, C_i^{Liq}= concentration of element 'i' in the residual melt, F = fraction of crystallization, D_i= bulk distribution coefficient of element 'i', $D_i = \sum_j X_j * K_{d,i,j}$, X_j= the mass fraction of mineral 'j' in the crystallizing assemblage, and $K_{d,j,i}$= crystal/melt portioning coefficient of element 'i' in mineral 'j'. The corresponding equation for the composition of element 'i' in mineral 'j':

$$(2)\ C_{i,j}^{Sol} = K_{d,i,j} C_{0,i}^{Liq} (1 - F)^{(D_i - 1)}$$

This equation can be rewritten in logarithmic form as:

$$(3)\ Log\left(C_{i,j}^{Sol}\right) - Log\left(C_{0,i}^{Liq}\right) = Log\left(K_{d,i,j}\right) + (D_i - 1) * Log(1 - F)$$

The equation for the expected chemical trend for mineral 'j' in a three-element graph (e.g. Log(K/Rb) vs. Log(Cs) in white mica) is as follows:

$$(4)\ Log\left(\frac{C_K^{Sol}}{C_{Rb}^{Sol}}\right) = A * Log\left(C_{Cs}^{Sol}\right) + [Log\left(C_{0,K}^{Liq} K_{d,K} / C_{0,Rb}^{Liq} K_{d,Rb}\right) - (1 + A) *$$

$$Log\left(C_{0,Cs}^{Liq} K_{d,Cs}\right)]$$

Where:

$$(5)\ A = \frac{D_K - D_{Rb}}{D_{Cs} - 1}$$

A comparable relationship can be derived for two-element graphs (e.g. Log(K/Rb) vs. Log(Rb) and Log(K/Cs) vs. Log(Cs) in white mica):

$$(6)\ Log\left(\frac{C_K^{Sol}}{C_{Rb}^{Sol}}\right) = A * Log\left(C_{Rb}^{Sol}\right) + [Log\left(C_{0,K}^{Liq} K_{d,K}\right) - (1 + A) *$$

$$Log\left(C_{0,Rb}^{Liq} K_{d,Rb}\right)]$$

Where:

$$(7)\ A = \frac{D_K - D_{Rb}}{D_{Rb} - 1}$$

And:

$$(8)\ Log\left(\frac{C_K^{Sol}}{C_{Cs}^{Sol}}\right) = A * Log\left(C_{Cs}^{Sol}\right) + [Log\left(C_{0,K}^{Liq} K_{d,K}\right) - (1 + A) * Log\left(C_{0,Cs}^{Liq} K_{d,Cs}\right)]$$

Where:

$$(9)\ A = \frac{D_K - D_{Cs}}{D_{Cs} - 1}$$

For the full derivations of the above equations, refer to Hulsbosch et al. (2014).

A strong case for a Rayleigh fractionation can be made if three elements in a mineral, plotted in a Log(E1/E2) vs. Log(E3) graph meet the following requirements (Hanson, 1978; Hulsbosch et al., 2014): (1) the data define a linear array, (2) the slope of the trendline depends on the values of the bulk distribution coefficients, (3) the y-intercept is a function of the bulk distribution coefficients, the partition coefficients and the initial concentrations of the elements in the partial melt.

It is noted by Taylor (1965) that the K₂O content of granites remain nearly constant during the differentiation. This implies that the bulk distribution coefficient of K remains

close to unity during fractional crystallization. If so, variable A can be simplified to -1 in equations (6) – (9) and can be reduced to the following:

$$(10)\ Log\left(\frac{C_K^{Sol}}{C_{Rb}^{Sol}}\right) = -Log\left(C_{Rb}^{Sol}\right) + Log\left(C_{0,K}^{Liq} K_{d,K}\right)$$

And:

$$(11)\ Log\left(\frac{C_K^{Sol}}{C_{Cs}^{Sol}}\right) = -Log\left(C_{Cs}^{Sol}\right) + Log\left(C_{0,K}^{Liq} K_{d,K}\right)$$

An analogous expression of Equation (10) is:

$$(12)\ \left(\frac{C_K^{Sol}}{C_{Rb}^{Sol}}\right) = \left(C_{0,K}^{Liq} * K_{d,K}\right)\left(\frac{1}{C_{Rb}^{Sol}}\right)$$

This equation is a hyperbola asymptotic to the x- and y- axes (Figure 2.19a,c). If K is kept constant during fractional crystallization, Rb or Cs will be enriched in relative to K, and a hyperbolic relationship is to be expected (Hulsbosch et al., 2014). The initial concentrations and mineral mass fraction of the theoretical S-type granite are listed in Table 2.2. A linear fit through a Log(K/Rb) vs Log(Rb) plot (Figure 2.19b) of the white mica (R^2=0.99) produces a slope of -1.02 and a y-intercept of 5.03. There is little to no variation in this line between the high F magmatic, low F magmatic and metasomatic analyses. This compares closely to the modelled slope of -1 and y-intercept of 4.95. A linear fit through a Log(K/Cs) vs Log(Cs) plot (Figure 2.19d) of the white mica (R^2=0.99) produces a slope of -1.01 and a y-intercept of 4.97. There is little variation in this line between the high F magmatic, low F magmatic and metasomatic analyses. This compares closely to the expected model slope of -1 and y-intercept of 4.95. A linear fit through a Log(K/Rb) vs Log (Cs) plot (Figure 2.19f) of the white mica produces three different slopes for high F, low F, metasomatic analyses of -0.25, -0.29, and -0.23 respectively and a y-intercept of 0.64, 0.71, and 0.54. This compares to the modelled slope of -0.42 and y-intercept of 2.13. The linear trends observed in the white mica data, and the deviation of some white mica grains from the theoretical model data, makes the case that Rayleigh fractional crystallization is not the only factor controlling the trace element variation throughout the pegmatite. The models presented in Figure 2.19a

through Figure 2.19d provide insight into the degree of crystallization required to achieve these trace element values. However, the models do a poor job distinguishing the previously observed trends in the data such as high F and low F magmatic grains or grains recrystallized by metasomatic fluid interactions, nor can it distinguish between the high F magmatic grains and the low F magmatic grains. Figure 2.19e and Figure 2.19f show that trace element value observed in this pegmatite cannot be achieved through only the fractional crystallization of a S-type granite.

All white mica grains analysed range between 99% and 99.99% crystallization of a typical S-type granite (Figure 2.19e). Fractional crystallization of 99.99% may not be reasonable but similar, and even higher concentrations of incompatible elements in melts can be attained through constitutional zone refining (CZR) London (2014). It is difficult to model constitutional zone refining without knowledge of the diffusivities of the incompatible elements and crystal growth rates, but the results of CZR are comparable to Raleigh fractionation (London, 2008).
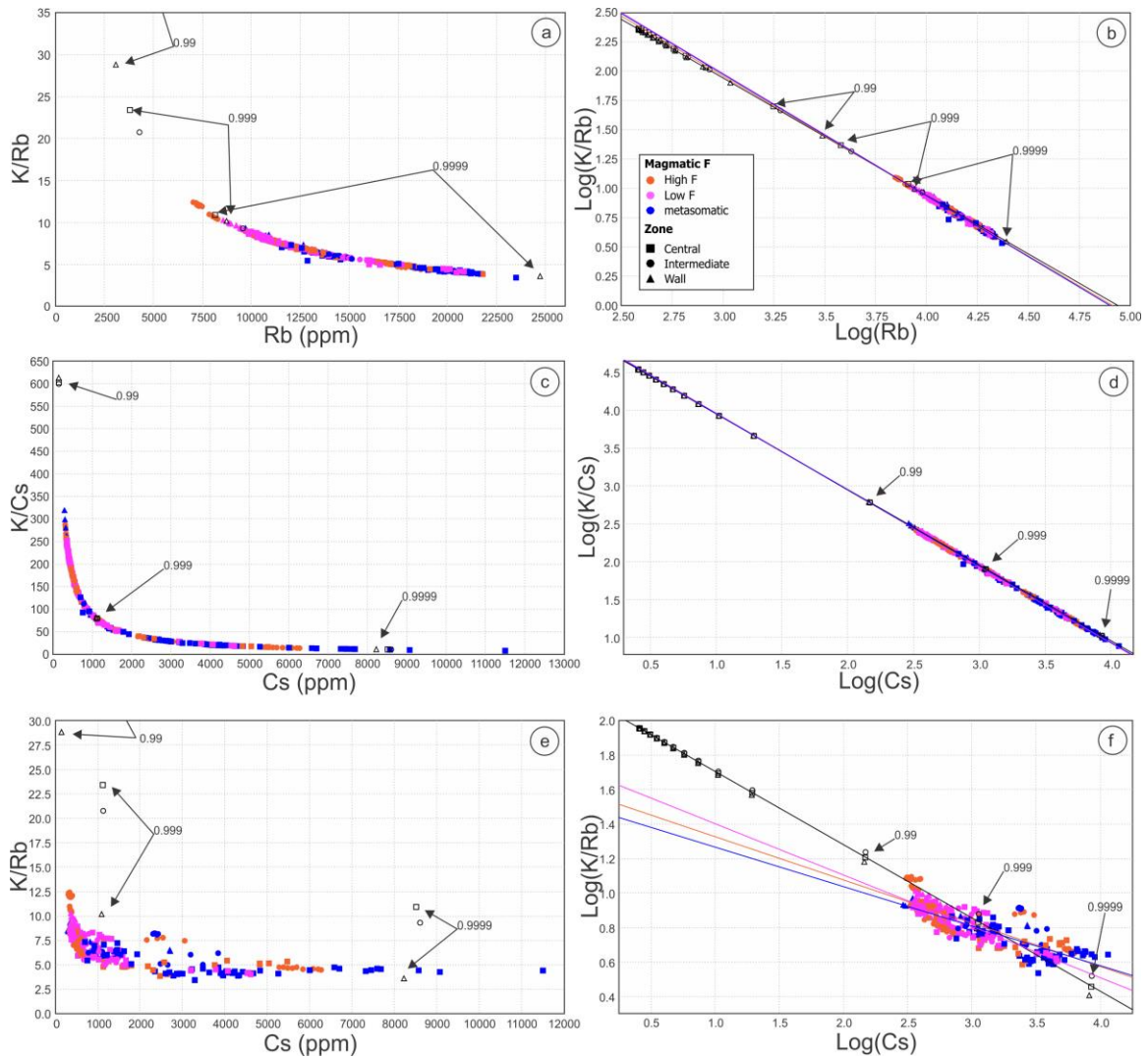
Figure 2.19: a,c,e) Modelled Rayleigh fractionation (F values shown) for alkali element trends in muscovite. b,d,f) corresponding log plots to a,c,e. Open symbols represent the modelled values from an initial granitic magma. Triangles represent the Wall zone, Circles represent the Intermediate zone and Squares represent the Central zone. Red symbols represent analyses from portions of the mica interpreted as high F magmatic, Pink symbols represent analyses from portions of the mica interpreted as low F magmatic and Blue symbols represent analyses from portions of the mica interpreted as metasomatics. A line of best fit was plotted through magmatic and metasomatic analyses.

The fractional crystallization of a pegmatitic melt (Table 2.2; Appendix F) was also modelled and is shown in Figure 2.20. The initial composition of the pegmatitic melt is a

theoretical composition based on the melt required to crystallization the most primitive mica analysis at 0.1% crystallization. This model shows the analysed mica grains ranging from 0.1% to 99% crystallization. The magmatic grains range from 0.1% to 99% crystallization. The metasomatic grains range from 30% to 99% crystallization. This supports a fractional crystallization origin for the pegmatite dikes at Wekusko Lake and shows how fractional crystallization can account for some of the chemical variations between the wall, intermediate and central zones. However, there are many points (both magmatic and metasomatic) that lie off the fractional crystallization curve. This is particularly true for the intermediate and central zones.

During fractional crystallization in white mica, Rb has a partition coefficient of 1.75 and Cs has a partition coefficient of 0.16. Therefore, it is expected to observe a larger increase in Rb compared to Cs. However, the metasomatic population has a larger variation in Cs relative to Rb than the magmatic population (Figure 2.13a, b) and have a greater K/Rb ratio than the modelled values (Figure 2.20). For Cs to increase without a proportional increase in Rb, there would have need to be a secondary Cs-rich fluid interacting with the white mica. This is supported by textural evidence such as zonation of the white mica grains near fractures, cleavage planes and grain boundaries (Figure 2.5). Our petrographic observations and fractional crystallization modelling suggest that textural variation within the white mica grain is not a primary magmatic feature, rather, a secondary metasomatic one similar to Xing et al. (2020). The Cs enrichment indicates that the late fluids are magmatic although their exact timing is unknown.
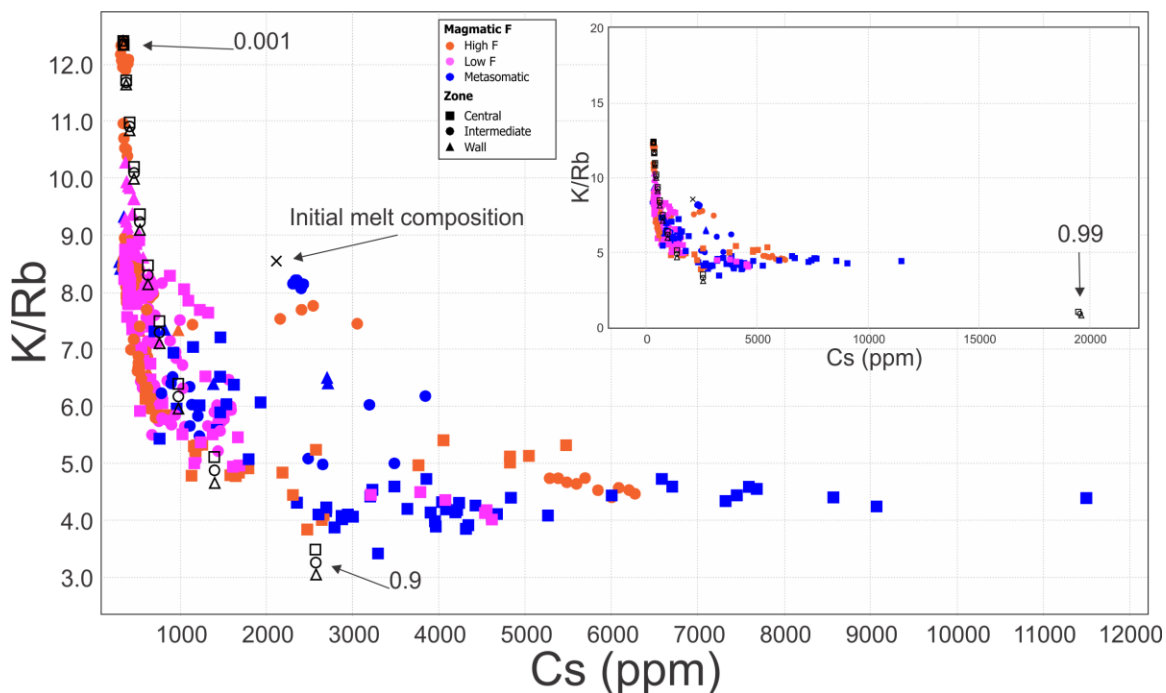
Figure 2.20: Modelled Rayleigh fractionation for K/Rb vs Cs for an initial melt composition (X) such that muscovite crystallized at F=0.001 has the same composition as the most primitive muscovite observed in Dike 1. Open symbols represent the modelled values crystallized from a magma with a composition marked with X such that the first micas formed are of similar compositions to the most primitive micas in Dike 1. Triangles represent the Wall zone, Circles represent the Intermediate zone and Squares represent the Central zone. Red symbols represent analyses from portions of the mica interpreted as magmatic and blue symbols represent analyses from portions of the mica interpreted as metasomatics. A line of best fit was plotted through magmatic and metasomatic analyses. Green arrow outlines pathway of increasing evolution in white mica.

Modelling mica crystallizing from fluids is currently a challenging task as limited experimental data is available. However, some fluid-melt partition coefficients have been determined (Zajacs, 2008; Iverson et al., 2019; Schmidt, 2018), making it possible to derive a fluid-mica partition coefficient (Antipin, 1980; Kovalenko, 1980):

$$Kd_{mica/fluid} = Kd_{mica/melt}/Kd_{fluid/melt}$$

However, this equation only works to estimate a mica crystallized from a fluid in equilibrium with fractional crystallization, rather than a mica crystallized during a secondary metasomatic event. Therefore, this mica composition is not different from the one that previous modelled above.

2.7   Conclusion

The 1.78 Ga Wekusko Lake pegmatites were emplaced early during the D4 brittle-ductile deformational event and subsequently folded during late D4 deformation. This places a maximum age of 1.78 Ga on the previously undated D4 deformational event.

The increased Li, Fe, Mn, and Mg in the white mica is a combination of phengitic substitution and octahedral Li-fixation. Rayleigh fractional crystallization could be controlling the trace element variation in micas throughout the pegmatite. Based on our theoretical modelling, the micas from the pegmatite dikes are a result of 99% to 99.99% fractional crystallization of granitic melt. This model does not account for the Cs enrichment observed in some of the studied micas. Together with textural evidence, we suggested that a post magmatic event, possible a Cs-rich secondary fluid caused metasomatism in the white mica grains.

Understanding the evolution of pegmatites are important steps in exploring the economic potential of the pegmatite. There are strong correlations between increased evolution and concentration of elements such as Li, Ta, Cs, and Tl. The K/Rb vs Cs in white mica is strong tool when analysing evolution and economic potential of pegmatite dikes, not just for Li potential but also other critical metals. This suggests that white mica is an indicator mineral for evaluating evolution in LCT-pegmatites.

2.8   References

Antipin, V. 1980. Partition coefficients of lead and zinc in acid rocks (as in ongonites) and their geochemical significance. Int. Geol. Rev. 22 **4**, 413–425.

Audetat, A., and Pettke, T. 2003. The magmatic-hydrothermal evolution of two barren granites: A melt and fluid inclusion study of the Rito del Medio and Cañada Pinabete plutons in northern New Mexico (USA). Geochimica et Cosmochimica Acta, **67**: 97-121.

Bailes, A. 1980. Origin of Early Proterozoic Volcaniclastic Turbidites, South Margin of The Kisseynew Sedimentary Gneiss Belt, File Lake, Manitoba. Precambrian Research, **12**: 197-225.

Bailey, S. W. 1984. Micas. Reviews in Mineralogy, **13**: 584.

Ballouard, C., Elburg, M., Tappe, S., Reinke, C., Ueckermann, H., and Doggart, S. 2020. Magmatic-hydrothermal evolution of rare metal pegmatites from the Mesoproterozoic Orange River pegmatite belt (Namaqualand, South Africa), Ore Geology Reviews, **116**: 103252

Benn, D., Martins, T., Linnen, R.L., Ziehlke, J. and Singh, J. 2018. Bedrock geology of the Wekusko pegmatite field (northeastern block), central Manitoba (parts of NTS 63J13); Manitoba Growth, Enterprise, and Trade, Preliminary Map PMAP2018-2, scale 1:4000.

Bibienne, T., Magnan, J-F., Rupp, A., and Laroche, N. 2020. From mine to mind and mobiles: society's increasing dependence on lithium. Elements, **16**: 265-270.

Bobba, S., Carrara, S., Huisman, J., Mathieux, F. and Pavel, C. 2020. European Commission, Critical materials for strategic technologies and sectors in the EU – a foresight study. Publications Office of the European Union, 2020.: 100.

Bowell, R., Lagos L, de los Hoyos, C., and Declercq, J. 2020. Classification and characteristics of natural lithium resources. Elements. **16**, 259-264.

Brigatti, M., Frigieri, P., and Poppi, L. 1998. Crystal chemistry of Mg-, Fe-bearing muscovites-2M1. Am. Mineral. **83**: 775–785.

Brigatti, M., Kile, D., and Poppi, M. 2001. Crystal structure and crystal chemistry of lithium-bearing muscovite-2M$_1$. The Canadian Mineralogist. **39**: 1171-1180.

Brisbin, W. 1986. Mechanics of pegmatite intrusion; American Mineralogist, **71**: 644–651.

Canosa, F., Martin-Izard, A., and Fuertes-Fuente, M. 2012. Evolved granitic systems as a source of rare-element deposits: the Ponte Segade case (Galicia, NW Spain). Lithos **153**:165–176.

Černý, P. 1986. Characteristics of pegmatite deposits of tantalum. In P. Möller, P. Černý, and F. Saupe, Eds., Lanthanides, Tantalum and Niobium,: 195–239. Springer-Verlag, Berlin

Černý, P. 1991. Rare-element granite pegmatites. Part I: anatomy and internal evolution

of pegmatite deposits. Geosci. Can. **18**: 49–67.

Černý, P. 2005. The Tanco rare-element pegmatite deposit, Manitoba: regional context, internal anatomy, and global comparisons. In: Rare-element geochemistry and mineral deposits, Geological Association of Canada Short Course Notes, **17**:127–158

Černý, P., and Burt, D. 1984. Paragenesis, crystallochemical characteristics, and geochemical evolution of the micas in granite pegmatites. Bailey, S. (ed.) Reviews in Mineralogy, **13**: 257-297.

Černý, P. and Ercit, T. 2005: The classification of granitic pegmatites revisited; The Canadian Mineralogist, **43**: 2005–2026.

Černý, P., London, D., and Novák, M. 2012. Granitic Pegmatites as Reflections of Their Rources. Elements, **8**: 289-294.

Černý, P., and Simpson, F.M. 1978. The Tanco Pegmatite at Bernic Lake, Manitoba: X. Pollucite. Canadian Mineralogist. **16**: 325–333.

Černý, P., Trueman, D., Zeihlke, D., Goad, B. and Paul, B. 1981. The Cat Lake-Winnipeg River and the Wekusko Lake pegmatite fields, Manitoba; Manitoba Department of Energy and Mines, Mineral Resources Division, Economic Geology Report ER80-1, 216 p. plus 5 maps.

Chakraborty, T., and Upadhyay, D. 2020. The geochemical differentiation of S-type pegmatites: constraints from major–trace element and Li–B isotopic composition of muscovite and tourmaline. Contrib Mineral Petrol. **175**: 60.

Connors, K., Ansdell, K. and Lucas, S. 1999. Coeval sedimentation, magmatism, and fold-thrust development in the Trans-Hudson Orogen: propagation of deformation into an active continental arc setting, Wekusko Lake area, Manitoba; Canadian Journal of Earth Sciences, **36**: p. 275–291.

Connors, K., Ansdell, K. and Lucas, S.B. 2002. Development of a transverse to orogen parallel extension lineation in a complex collisional setting, Trans-Hudson Orogen, Manitoba, Canada; Journal of Structural Geology, **24**: 89–106.

Corrigan, D., Hajnal, Z., Németh, B., and Lucas, S.B. 2005. Tectonic framework of a Paleoprotoerozoic arc–continent to continent–continent collisional zone, Trans-Hudson Orogen, from geological and seismic reflection studies. Canadian Journal of Earth Sciences, **42**: 421–434.

Darbyshire, F., Bastow, I., Petrescu, L., Gilligan, A., and Thompson, D. 2017. A tale of two orogens: Crustal processes in the Proterozoic Trans-Hudson and Grenville Orogens, eastern Canada. Tectonics, **36**: 1633–1659.

David, J., Bailes, A. and Machado, N. 1996. Evolution of the Snow Lake portion of the Palaeoproterozoic Flin Flon and Kisseynew belts, Trans-Hudson Orogen, Manitoba, Canada; Precambrian Research, **80**: 107–124.

Dewaele, S., Hulsbosch, N., Cryns, Y., Boyce, A., Burgess, R., and Muchez, P. 2015. Geological setting and timing of the world-class Sn, Nb-Ta and Li mineralization of

Manono-Kitotolo (Katanga, Democratic Republic of Congo). Ore Geology Reviews, **72**: 373-390.

Dingwell, D., Hess, K., and Knoche, R. 1996. Granite and granitic pegmatite melts: volumes and viscosities. Trans. R. Soc. Edinburgh, Earth Sci. **87**: 65–72.

Dyar, M., Lowe, E., Guidotti, C., and Delaney, J. 2000. Ferric and ferrous iron partitioning among silicates in metapelites; a synchrotron micro-XANES (SmX) study. American Mineralogist, **87**: 514-522.

Eaton, D., and Darbyshire, F. 2010. Lithospheric architecture and tectonic evolution of the Hudson Bay region. Tectonophysics, **480**: 1-22

Evans, K. 2014. Lithium. Gunn, G., (ed.) Critical Metals Handbook. American Geophysical Union,: 230-260.

Fedikow, M., and Zelligan, S. 2018. Ni 43-101 Technical Report On The Zoro Lithium Project, Snow Lake, Manitoba, Far Resources Inc.

Fleet, M. E., Deer, W. A., Howie, R. A., and Zussman, J. 2003. Rock-Forming Minerals. Volume 3A. Mica, second ed. The Geological Society, London.

Foster, M. 1956. Correlation of dioctahedral potassium micas on the basis of their charge relations. U.S. Geol. Surv. Bull., **1036-D**, 57–67.

Garrett, D. 2004. Handbook of Lithium and Natural Calcium Chloride: Their Deposits, Processing, Uses and Properties. Academic Press,: 488.

Gay, N. 1980. The state of stress in the plates. Bally, A., Bender, P., McGetchin, T., and Walcott, R. (ed.); Geodynamics Series, **1**: 145-153.

Gordon, T., Hunt, P., Bailes, A. and Syme, E. 1990. U-pb ages from the Flin Flon and Kisseynew belts, Manitoba; chronology of crust formation at an early Proterozoic accretionary margin; *in* The Early Proterozoic Trans-Hudson Orogen of North

America, Lewry, J., and Stauffer, M., (ed.); Geological Association of Canada, Special Paper **37**: 177–199.

Grammatikopoulos, T., Aghamirian, M., Fedikow, M. and Mayo, T. 2020. Mineralogical Characterization and Preliminary Beneficiation of the Zoro Lithium Project, Manitoba, Canada. Mining, Metallurgy & Exploration, **38**: 329–346.

Groat, L., Mulja, T., Mauthner, M., Ercit, T., Raudsepp, M., Gault, R., and Rolle, H. 2003. Geology and mineralogy of the Little Nahanni rare-element granitic pegmatites, Northwest Territories. The Canadian Mineralogist, **41**: 139-160.

Hammer, P., Clowes, R., Cook, F., Van Der Velden, A., and Vasudevan, K. 2010. The Lithoprobe trans-continental lithospheric cross sections: imaging the internal structure of the North American continent. Can. J. Earth Sci., **47**: 821-857.

Hertogen, J., and Gijbels, R. 1976. Calculation of trace element fractionation during partial melting. Geochim. Cosmochim. Acta., **40**: 313–322.

Higuchi, H., and Nagasawa, H. 1969. Partition of trace elements between rock-forming minerals and the host volcanic rocks. Earth and Planetary Science Letters., **7**: 281-287.

Hoffman, P. 1988. United Plates of America, the birth of a craton: Early Proterozoic assembly and growth of Laurentia; Annual Review of Earth and Planetary Sciences, **16**: 543–603.

Hoffman, P. 1989. Precambrian geology and tectonic history of North America; *in* The Geology of North America—an overview, A.W. Bally and A.R. Palmer (ed.); Geological Society of America, The Geology of North America, **A**: 447–512.

Horn, I., and von Blanckenburg, F. 2007. Investigation on elemental and isotopic fractionation during 196 nm femtosecond laser ablation multiple collector inductively coupled plasma mass spectrometry. Spectrochimica Acta Part B-Atomic Spectroscopy, **62**: 410–422.

Hulsbosch, N., Hertogen, J., Dewaele, S., André, L., and Muchez, P. 2014. Alkali metal and rare earth element evolution of rock-forming minerals from the Gatumba area pegmatites (Rwanda): quantitative assessment of crystal-melt fractionation in the regional zonation of pegmatite groups. Geochim Cosmochim Acta, **132**: 349–374.

Icenhower, J., and London, D. 1997. Partitioning of fluorine and chlorine between biotite and granitic melt; experimental calibration at 200 MPa H_2O. Contributions to Mineralogy and Petrology, **127**: 17-29.

Iveson, A., Webster, J., Rowe, M., and Neill, O. 2019. Fluid-melt trace element partitioning behaviour between evolved melts and aqueous fluids: experimental constraints on the magmatic-hydrothermal transport of metals. Chem. Geol., **516**: 18–41.

Jolliff, B., Papike, J., and Shearer, C. 1987. Fractionation trends in mica and tourmaline as indicators of pegmatite internal evolution: Bob Ingersoll pegmatite, Black Hills, South Dakota. Geochimica et Cosmochimica acta. **51**: 519-534.

Kaeter, D., Barros, R., Menuge, J. F., and Chew, D. M. 2018. The magmatic-hydrothermal transition in rare element pegmatites from southeast Ireland; LA-ICP-MS chemical mapping of muscovite and columbite-tantalite. Geochimica Et Cosmochimica Acta, **240**: 98-130.

Kontak, D. 2006. Nature and origin of an LCT-suite pegmatite with late-stage sodium enrichment, Brazil Lake, Yarmouth County, Nova Scotia. I. Geological setting and petrology. Can. Mineral., **44**: 563–598.

Kovalenko, V. 1980. Distribution ratios of lithium, rubidium, and cesium in ongonites. Int. Geol. Rev. **22**: 718–730.

Kraus, J., and Menard, T. 1997. A thermal gradient at constant P: implications for low- to medium-P metamorphism in a compressional tectonic setting, Flin Flon and Kisseynew domains, Trans-Hudson orogen, central Canada. Can. Mineral., **35**: 1117–1136.

Lewry, J., Hajnal, Z., Green, A., Lucas, S., White, D., Stauffer, M., Aston, K., Weber, W., and Clowes, R. 1994. Structure of Paleoproterozoic continent-continent collision zone: LITHOPROBE seismic reflection profiles across the Trans-Hudson orogen. Tectonophysics, **232**: 143–160.

Linnen, R., and Williams-Jones, A. 1993. Mineralogical constraints on magmatic and hydrothermal Sn-W-Ta-Nb mineralization at the Nong Sua aplite-pegmatite, Thailand. European Journal of Mineralogy, **5**: 721-736.

Linnen, R., Williams-Jones, A. 1995. Genesis of a magmatic metamorphic hydrothermal system; the Sn-W polymetallic deposits at Pilok, Thailand. Econ. Geol., **90**: 1148–1166.

Liu, C., Wang, R.C., Wu, F.Y., Xie, L., Liu, X.C., Li, X.K., Yang, L., and Li, X.J. 2020. Spodumene pegmatites from the Pusila pluton in the higher Himalaya, South Tibet: Lithium mineralization in a highly fractionated leucogranite batholith. Lithos, **358-359**: 105421.

London, D. 1989. Lithophile rare element concentration in silicic rocks: the alkaline trend in granitic systems. Geol. Mineral. Assoc. Canada, Program with Abstracts, **14**: A21.

London, D. 2005. Geochemistry of alkali and alkaline earth elements in ore-forming granites, pegmatites, and rhyolites. In Rare-element geochemistry and mineral deposits. GAC Short Course Notes 17 (eds. L. R. Linnen, I. M. Samson). Geological Association of Canada, St. Catharines, Ontario,: 17–44.

London, D. 2008. Pegmatites. The Canadian Mineralogist, Special Publication, **10**: 347.

London, D. 2014. A petrologic assessment of internal zonation in granitic pegmatites. Lithos, **184-187**: 74-104.

London, D. 2017. Reading Pegmatites: Part 3—What Lithium Minerals Say. Rocks & Minerals, **92**: 144-157.

Lucas, S., Green, A., Hajnal, Z., White, D., Lewry, J., Ashton, K., Weber, W., and Clowes, R. 1994. Deep seismic profile across a Proterozoic collision zone: Surprises at depth. Nature, **363**: 339–342.

Lucas, S., Stern, R., Syme, E., Reilly, B., and Thomas, D. 1996. Intraoceanic tectonics and the development of continental crust: 1.92–1.84 Ga evolution of the Flin Flon Belt, Canada; Geological Society of America Bulletin, **108**: 602.

Manitoba Geological Survey, 2020. Compilation of Sm-Nd isotope results from the Manitoba Geological Survey 2018/2019 season. Manitoba Agriculture and Resource Development, Manitoba Geological Survey, Data Repository Item DRI2020012, Microsoft® Excel® file.

Manitoba Geological Survey, 2021. Compilation of Sm-Nd isotope results and accompanying whole-rock geochemistry (to 2017) for the Trans-Hudson orogen, Manitoba (parts of NTS 63F, J, K, 63N–P, 64A–C, 64F–H); Manitoba Agriculture and Resource Development, Manitoba Geological Survey, Data Repository Item DRI2021008, Microsoft® Excel® file.

Martins, T., Benn, D. and McFarlane, C. 2019. Laser-ablation inductively coupled plasma–mass spectrometry (LA-ICP-MS) analyses of columbite grains from Li-bearing pegmatites, Wekusko Lake pegmatite field (northeastern block), central Manitoba (part of NTS 63J13); Manitoba Agriculture and Resource Development, Manitoba Geological Survey, Data Repository Item DRI2019003, Microsoft® Excel® file.

Martins, T., Linnen, R., Fedikow, M. and Singh, J. 2017. Whole-rock and mineral geochemistry as exploration tools for rare-element pegmatite in Manitoba: examples from the Cat Lake–Winnipeg River and Wekusko Lake pegmatite fields (parts of NTS 52L6, 63J13); in Report of Activities 2017, Manitoba Growth, Enterprise and Trade, Manitoba Geological Survey,: 42–51.

Martins, T., Roda-Robles, E., Lima, A., and De Parseval, P. 2012. Geochemistry and evolution of micas in the Barroso–Alvão pegmatite field, northern Portugal. The Canadian Mineralogist, **50**: 1117-1129.

McFarlane, C., and Luo, Y. 2012. U-Pb geochronology using 193 nm excimer LA-ICP-MS optimized for in situ accessory mineral dating in thin sections. Geosci. Can., **39**: 158-172.

McNeil, A., Linnen, R., Flemming, R., and Fayek, M. 2020. An experimental approach to examine fluid-melt interaction and mineralization in rare-metal pegmatites. American Mineralogist, **105**: 1078-1087.

Maneta, V., Baker, D., and Minarik, W. 2015. Evidence for lithium-aluminosilicate supersaturation of pegmatite-forming melts. Contrib. Mineral. Petrol., **170**: 4.

Maneta, V., and Baker, D. R. 2019. The potential of lithium in alkali feldspars, quartz, and muscovite as a geochemical indicator in the exploration for lithium-rich granitic pegmatites; a case study from the spodumene-rich Moblan pegmatite, Quebec, Canada. Journal of Geochemical Exploration, **205**: 106336.

Monier, G., and Robert, J. 1986. Evolution of the miscibility gap between muscovite and biotite solid solutions with increasing lithium content: an experimental study in the system K_2O-Li_2O-MgO-FeO-Al_2O_3-SiO_2-H_2O-HF at 600 ∘C, 2 kbar PH_2O: comparison with natural lithium micas. Mineral. Mag., **50**: 641–651.

Munoz, J. 1968. Physical properties of synthetic lepidolites. American Mineralogist, **53**: 1490-1512.

NATMAP Shield Margin Project Working Group, 1998. Geology, NATMAP shield margin project area (Flin Flon Belt), Manitoba/Saskatchewan; Geological Survey of Canada, Map 1968A, scale 1:100 000.

Natural Resources Canada, 2021. Canada's Critical Minerals List 2021. Government of Canada. https://www.nrcan.gc.ca/our-natural-resources/minerals-mining/critical-minerals/23414

Pan Y. 1997. Controls on the fractionation of isovalent trace elements in magmatic and aqueous systems: evidence from Y/Ho, Zr/Hf, and lanthanide tetrad effect—a discussion of the article by M. Bau (1996). Contrib. Mineral. Petrol., **128**: 405–408.

Paton, C., Hellstrom, J., Paul, B., Woodhead, J., and Hergt, J. 2011. Iolite: Freeware for the visualisation and processing of mass spectrometric data. Journal of Analytical Atomic Spectrometry, **26**: 2508–2518.

Pearce, J., and Cann, J. 1973. Tectonic setting of basic volcanic rocks determined using trace element analyses. Earth and Planetary Science Letters, **19**: 290-300.

Philpotts, J., and Schnetzler, C. 1970. Phenocryst-matrix partition coefficients for K, Rb, Sr and Ba, with applications to anorthosite and basalt genesis. Geochim Cosmochim Acta, **34**: 307–322.

Potter, E., Taylor, R., Jones, P., Lalonde, A., Pearse, G., and Rowe, R. 2009. Sokolovaite and evolved lithian micas from the eastern Moblan granitic pegmatite, Opatica subprovince, Quebec, Canada. The Canadian Mineralogist, **47**: 337-349.

Roda, E., Pesquera Perez, A., Velasco Roldan, F., Černý, P., and Novak, M. 1995. Micas of the muscovite-lepidolite series from the fregeneda pegmatites (salamanca, spain). Mineralogy and Petrology, **55**: 145-157.

Roda, E., Pesquera, A., Gil-Crespo, P.P., Torres-Ruiz, J., Fontan, F. 2005. Origin and internal evolution of the Li-F-Be-B-P-bearing Pinilla de Fermoselle pegmatite (Central Iberian Zone, Zamora, Spain). Am. Mineral., **90**: 1887-1899.

Roda, E., Keller, P., Pesquera, A., and Fontan, F. 2007. Micas of the muscovite-lepidolite series from karibib pegmatites, Namibia. Mineralogical Magazine, **71**: 41-62.

Ryan, J. and Williams, P. 1999. Structural evolution of the eastern Amisk collage, Trans-Hudson Orogen, Manitoba; Canadian Journal of Earth Sciences, **36**: 251–273.

Schmidt, M.W., Dugnani, M., and Artioli, G. 2001. Synthesis and characterization of white micas in the join muscovite–aluminoceladonite. Am. Mineral., **86**: 555–565.

Schmidt, C. 2018. Formation of hydrothermal tin deposits: Raman spectroscopic evidence for an important role of aqueous Sn (IV) species. Geochim. Cosmochim. Acta., **220**: 499–511.

Schneider, D., Heizler, M., Bickford, M., Wortman, G., Condie, K. and Perilli, S. 2007. Timing constraints of orogeny to cratonization: thermochronology of the Paleoproterozoic Trans-Hudson orogen, Manitoba and Saskatchewan, Canada; Precambrian Research, **153**: 65–95.

Schwartz, M.O. 1992. Geochemical criteria for distinguishing magmatic and metasomatic albite-enrichment in granitoids—examples from the Ta-Li granite Yichun (China) and the Sn-W deposit Tikus (Indonesia). Mineralium Deposita, **27**: 101–108.

Selway, J., Breaks, F. and Tindle, A. 2005. A review of rare-element (Li-Cs-Ta) pegmatite exploration techniques for the Superior Province, Canada, and large worldwide tantalum deposits; Exploration and Mining Geology, **14**: 1–30.

Siegel K., Wagner T., Trumbull R., Jonsson E., Matalin G., Wälle, M., and Heinrich C. 2016. Stable isotope (B, H, O) and mineral-chemistry constraints on the magmatic to hydrothermal evolution of the Varuträsk rare-element pegmatite (Northern Sweden). Chem. Geol. **421**: 1–16.

Stewart, D. 1978. Petrogenesis of lithium-rich pegmatites. American Mineralogist. **63**: 970–980.

Sun, S. and McDonough, W.F. 1989. Chemical and isotopic systematics of oceanic basalts: implications for mantle composition and processes; Geological Society of London, Special Publication, **42**: 313–345.

Syme, E., Lucas, S., Bailes, A., and Stern, R. 1999. Contrasting arc and MORB-like assemblages in the Paleoproterozoic Flin Flon Belt, Manitoba, and the role of intra-

arc extension in localizing volcanic-hosted massive sulphide deposits. Canadian Journal of Earth Sciences, **36**: 1767-1788.

Taylor, S. 1965. The application of trace element data to problems in petrology. Phys. Chem. Earth, **6**: 133–213.

Thomas, R., Davidson, P., and Beurlen, H. 2012. The competing models for the origin and internal evolution of granitic pegmatites in the light of melt and fluid inclusion research. Mineral. Petrol., **106**. 55–73.

Tindle, A., and Webb, P. 1990. Estimation of lithium content in trioctahedral micas using microprobe data: application to micas from granitic rocks. Eur. J. Mineral., **5**: 595–610.

Tindle, A., Breaks F., and Webb P. 1998. Wodginite group minerals from the Separation Rapids rare-element granitic pegmatite group, NW Ontario. Can. Mineral. **36**: 637–658.

Tischendorf, G., Gottesmann, B., Förster, H., and Trumbull, R. 1997. On Li-bearing micas: estimating Li from electron microprobe analyses and an improved diagram for graphical representation. Mineral. Mag., **61**: 809–834.

Tischendorf, G., Förster, H., Gottesmann, B., and Rieder, M. 2007. True and brittle micas: composition and solid-solution series. Mineralogical Magazine, **71**: 285-320.

van Hinsberg, V. 2011. Preliminary experimental data on trace element partitioning between tourmaline and silicate melt. Can. Mineral., **49**:153–163.

Van Lichtervelde, M., Salvi, S., Béziat, D., and Linnen, R.L. 2007. Textural features and chemical evolution in tantalum oxides: Magmatic versus hydrothermal origins for Ta mineralization in the Tanco Lower Pegmatite, Manitoba, Canada. Economic Geology, **102**: 257–276.

Van Litchervelde, M., Gregiore, M., Linnen, R., Beziat, D., and Salvi, S. 2008. Trace element geochemistry by laser ablation ICP-MS of micas associated with Ta mineralization in the Tanco pegmatite, Manitoba, Canada. Contrib Mineral Petrol, **155**: 791–806.

Wang, R., Hu, H., Zhang, A., and Fontan, F. 2007. Cs-dominant polylithionite in the Koktokay#3 pegmatite, Altai, NW China: in situ micro-characterization and implication for the storage of radioactive cesium. Contrib. Mineral. Petrol., **153:** 355–367.

Wise, M. 1995. Trace element chemistry of lithium-rich micas from rare-element granitic pegmatites. Mineralogy and Petrology. **55**: 203-215.

Wise, M., and Brown, C. 2010. Mineral chemistry, petrology and geochemistry of Sebago granite-pegmatite system, southern Maine, USA. Journal of Geosciences, **55**: 3-26.

Winchester, J., and Floyd, P. 1977. Geochemical discrimination of different magma series and their differentiation products using immobile elements. Chemical Geology, **20**: 325-343.

Xing, C., Wang, C., and Wang, H., 2020. Magmatic-hydrothermal processes recorded by muscovite and columbite-group minerals from the Bailongshan rare-element pegmatites in theWest Kunlun-Karakorum orogenic belt, NW China. Lithos, **364-365**.

Yang, Z., Wang, R., Che, X., Yin, R., Xie, L., and Hu, H. 2020. Formation of columbite and microlite after alteration of Nb- and Ta-bearing biotite from the Lizaizhai pegmatite (Guangning ore district, Guangdong, South China): Identification of a new potential Nb–Ta mineralization type. Journal of Asian Earth Sciences. **190**: 104154.

Zajacz, Z., Halter, W.E., Pettke, T and Guillong, M. 2008. Determination of fluid/melt partition coefficients by LA-ICPMS analysis of co-existing fluid and silicate melt

inclusions: controls on element partitioning. Geochim. Cosmochim. Acta., **72**: 2169–2197.

Zoback M.L., and Zoback M. 1980. State of Stress in the Conterminous United States. Journal of Geophysical research, **85**.

Chapter 3

3   Integrated Paper 2

3.1   Introduction

Lithium exploration is on the rise due to an increased need for Li products most notably Li-ion batteries. The majority of Li resources is hosted in two types of deposits: Li-Cs-Ta (LCT) pegmatites (e.g., Greenbushes, Australia), and brines (e.g., Salar de Atacama, Chile) (Kesler et al., 2012; Sterbia et al., 2019; Bowell et al., 2020), although clay deposits (such as hectorite and jadarite) may also be important in the future. Pegmatites contain the highest Li grades (0.5 – 1.2 wt%) and lower tonnages (<1000 Kt), brines have lower Li grades (<0.2 wt%) and larger tonnages (<6000 Kt) (Sinclair, 1995; Mohr et al., 2012, Bradley et al., 2017).

Typical LCT pegmatite exploration uses a combination of lithogeochemistry, soil geochemistry, stream sediment geochemistry, mineralogy, and mineral chemistry (Trueman and Černý, 1982; Galeschuk and Vanstone, 2005; Steiner, 2019) but other techniques such as LiDAR (Dart Mining NL, 2021) and remote sensing (Cardoso-Fernandes et al., 2021), and methods that integrate a variety of statistical approaches (e.g., Deveaud et al., 2013; Fyzollahhi et al., 2018) are also gaining traction.

Lithogeochemistry relies on trace element (mainly Li, Rb, and Cs) mobility through the host rock to produce aureoles around the dikes (Ovchkinnikov 1976, Morgan and London, 1987). The size of the aureoles is controlled by the composition and structure of the host rock (Beus et al., 1968) and the mobility of the element that is being measured (Shearer et al., 1986). This method is subject to false anomalies caused by footwall aureoles from eroded pegmatites, underestimated aureoles thicknesses of deeply buried pegmatites and metasomatic aureoles caused by alkali-rich fluids migrating through fractures (Galeschuk and Vanstone, 2005). It has been suggested that the geochemical analysis of fracture mineralization (such as chlorite) can produce a stronger aureole (Linnen et al., 2015). Geophysical techniques are not widely used although gravity has

potential because of the high density of spodumene (Trueman and Černý, 1982) and other techniques such as magnetics can show strong contrasts between pegmatites and wallrocks. An alternative to lithogeochemistry is soil chemistry, generally from the B-Horizon. These can be analysed from bulk samples (Steiner, 2019), using the MMI (Mobile Metal Ion) technique (e.g., www.foremostlithium.com) or using the Enzyme Leach method (Clark, 1993). The latter involves the preferential dissolution of amorphous manganese oxides, which are ionic traps for trace elements that migrate through the subsurface from depths (Clark, 1993; Clark, 1997), although other extraction methods have also been used (Xu et al., 2019). The Enzyme Leach method is particularly useful when exploring for pegmatites buried under the overburden (Galeschuk and Vanstone, 2005) and has produced positive anomalies for pegmatites when lithogeochemistry could not (Galeschuk, 2001). The use of mineral typomorphism and mineral chemistry becomes important when evaluating the prospective mineralization within pegmatite dikes (Trueman and Černý, 1982). Mineral typomorphism uses the occurrences and variable properties of accessory minerals to classify the evolutionary stage of the pegmatite (Trueman and Černý, 1982). Mineral chemistry is ideal for identifying fractionation trends within pegmatite fields and individual pegmatite dikes (Trueman and Černý, 1982; Selway et al., 2005; Maneta and Baker, 2019). This technique typically uses the K/Rb ratios in alkali feldspars, Li/Al, Ti/Al, B/Al, Ge/Al ratios in quartz and the K/Rb, K/Cs, and Mg/Li ratios in muscovite to distinguish between barren and fertile pegmatites (Chpt 2; Gordiyenko, 1971; Trueman and Černý, 1982; Smeds, 1992, Selway et al., 2005; Beurlen et al., 2011; Beurlen et al., 2014; Maneta and Baker, 2019).

Chapter 2 uses trace elements, notably Li, Cs and K/Rb ratios in the white micas to describe the fractionation and internal evolution of the largest studied pegmatite dike. Pegmatite zones that show a high degree of fractionation were associated with the highest concentrations of Li, Cs and Ta, and contain spodumene and columbite group minerals (CGM). White micas are also present in these zones, thus white micas may be a useful tool for identifying and distinguishing fertile and barren zones of an individual pegmatite dike. Considering the heterogenous nature of pegmatites, and the small size of an average pegmatite dike, a single drill hole may not intersect all the zones of the pegmatite, thus it

is difficult to interpret whether a pegmatite is mineralized or barren without additional drilling. An objective of this study is to determine whether it is possible to use white mica chemistry to distinguish between the wall or intermediate zones of mineralized pegmatites compared to those of a fertile pegmatite.

Related to the previous objective is whether white mica compositions can be measured using field portable techniques. The use of field portable techniques has been increasing as more laboratory techniques adapted and precision/accuracy are improved upon (Lemiere, 2015; Wise et al., 2022). This allows for real-time decision making and more flexibility during the planning phases of a project. Field analyses allow for selection of the most promising target, without fewer resources wasted on less viable targets (Galuszka et al., 2015; Zhang et al., 2017). The continuous stream of feedback leads to more effective decision making and more efficient exploration. These decrease the cost and length of the field operation.

One of most commonly used techniques since the 1990s is x-ray fluorescence (XRF) (Lemiere, 2018). The portable XRF is able to simultaneously measure elements from atomic number 11 (Al) to 82 (Pb) (Young et al., 2016; Ryan et al., 2017; Skupio, 2020). This makes XRF a powerful tool for obtaining quick elemental compositions of rock and mineral samples. However, it is unable to distinguish mineral polymorphs or measure lighter elements common in pegmatites such Li, Be, and B. The samples from Wekusko Lake in this study were analysed by two field portable techniques: laser induced breakdown spectrometer (LIBS) and the handheld Raman spectrometer to determine their utility to pegmatite exploration.

Field portable LIBS is a recently developed technique that is complimentary to portable XRF (Forte and Laserna, 2010; Connors et al., 2016). LIBS uses atomic emission spectroscopy, using a high-energy laser pulse to generate plasma on the surface of the sample. The characteristic spectral emissions from the plasma are captured on a series of spectrometers. The handheld LIBS is able to identify a wider range of elements than XRF, including elements as light as Li (Harmon et al., 2013). It has the additional benefits of requiring little to no sample preparation, requires very little sample for

analysis and is minimally destructive. It is also able to measure trace elements to ppm levels (Hark and Harmon, 2014). The handheld LIBS have been used to obtain the Li contents of a variety of minerals (Sweetapple and Tassios, 2015; Fabre et al., 2021) and specifically, the K/Rb and Li contents of micas (Wise et al., 2022). However, the novelty of this technique means it is still in need of standardized protocols and exploration-oriented standard libraries (Lemiere and Uvarova, 2019; Fabre et al., 2021).

Raman spectroscopy is a well-known laboratory technique and has been widely used in geology since the 1980s (Pasteris and Bayssac, 2020). Handheld Raman spectrometers became available in the 2010s. Raman spectroscopy is a vibrational technique that produces a spectrum with peaks corresponding to specific bonds or groups of bonds (Mernagh and Trudu, 1993). This results in a unique spectral "fingerprint" for each mineral, even those with the same chemical composition (i.e., mineral polymorphs). Raman spectroscopy is sensitive to structural changes and cation substitutions in minerals (Hope et al., 2001; Babedi et al., 2019). However, handheld Raman spectrometers are highly susceptible to interference from ambient light and cosmic rays.

Chapter 2 identifies the chemical substitutions occurring within muscovite as it becomes more Li-rich. As muscovite incorporates Li^{1+} and either Mg^{2+} or Mn^{2+} for $^{IV}Al^{3+}$ causing it to transition from a dioctahedral mica (i.e., two cations in the octahedral site) into a trioctahedral mica (i.e., three cations in the octahedral site). A second substitution occurs in which Si^{4+} and Fe^{2+} replace $^{VI}Al^{3+}$ and $^{IV}Al^{3+}$. This changes the charge balance between the tetrahedral and octahedral sites. Both these substitutions will have an effect on the vibrational bond energy in the structure of the white mica, thus it is possible that these substitutions can be documented by handheld Raman spectrometer analysis.

3.2 Wekusko Lake Pegmatite Dikes

The Wekusko Lake pegmatite field is located in the Snow Lake-Flin Flon area of west-central Manitoba. The Wekusko Lake pegmatite field are part of the Green Bay Group pegmatites (Černý et al., 1981; Benn et al., 2018a). The Zoro lithium project Foremost Lithium Resources & Technology (formerly Far Resources ltd.) is located within the

Wekusko Lake pegmatite, east-central Manitoba, Canada. This field area contains thirteen identified pegmatite dikes, eight of which are included in this study (Figure 3.1). The eight dikes were mapped in 2018 (Benn et al., 2018a), and drill core from 35 holes was logged and sampled from 6 of the dikes. Dike 3 and Dike 6 were not drilled at the time of this study.
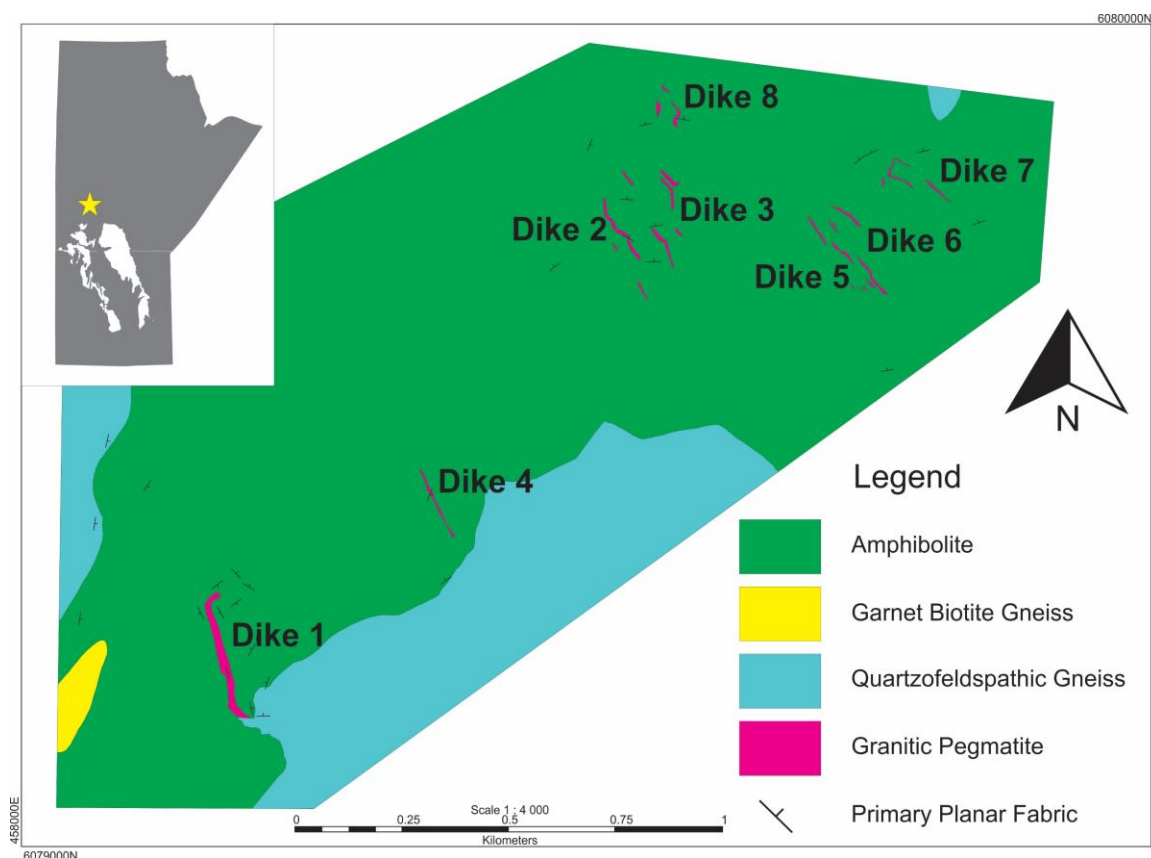
Figure 3.1: Simplified geological map of the Wekusko Lake pegmatite field (Manitoba, Canada), modified from Benn et al., 2018.

The dikes all consist of variable concentrations of albite, quartz, K-feldspars, spodumene, white mica, tourmaline with accessory apatite, Fe-Mn phosphate minerals, beryl, garnet, and trace CGM, arsenopyrite, and cassiterite (Benn et al., 2018b; Grammatikopoulos et al., 2020), and can be classified as LCT, rare-element (REL) class, REL-Li subclass, complex type, spodumene sub-type (Černý and Ercit, 2005). Metallurgical work on the largest dike, Dike 1, was conducted by Grammatikopoulos et al. (2020) and they reported

a modal composition of 29% plagioclase, 29% quartz, 21% K-feldspar, 10.5% spodumene, 5% mica, 3% tourmaline, and 0.1% Fe-Mn phosphate minerals.

All dikes consist of five zones: border, wall, intermediate, central and core. Details of the zones are provided in Chapter 2, but the highest concentration of spodumene is within the Central zone.

The dikes that have been drilled are ranked in this study based on average Li (wt% Li_2O) values from assays, intersection lengths, and dike thickness (Appendix G). The sum of the Li (wt% Li_2O) assays was divided by the intersection length to get Li (wt% Li_2O) per meter, for dikes with similar Li/m values the larger dike was ranked higher. From more prospective to least prospective, the dikes are ranked as follows: Dike 1, Dike 8, Dike 5, Dike 7, Dike 4, Dike 2. Dike 1 has the second highest average Li assay values (0.61 wt% Li_2O) but only slightly less than Dike 8 (0.62 wt% Li_2O) (Figure 3.2; Appendix G). Dike 1 is the largest dike in the field area (Benn et al., 2018a). Dike 5 and Dike 7 are moderately sized, with moderate Li assay values in Dike 5 (0.30 wt% Li_2O) and moderately low in Dike 7 (0.15 wt% Li_2O) (Figure 3.2; Appendix G). Dike 4 and Dike 2 both have low average Li assay values, 0.13 wt% Li_2O and 0.05 wt% Li_2O respectively (Figure 3.2; Appendix G).

Figure 3.2: Whole rock Li assays by (a) dike number and (b) dike zone.

3.3   Methods

Samples were obtained from quartered drill core. Thin sections were cut and polished, for transmitted light microscopy at the Earth and Planetary Materials Analysis Laboratory at
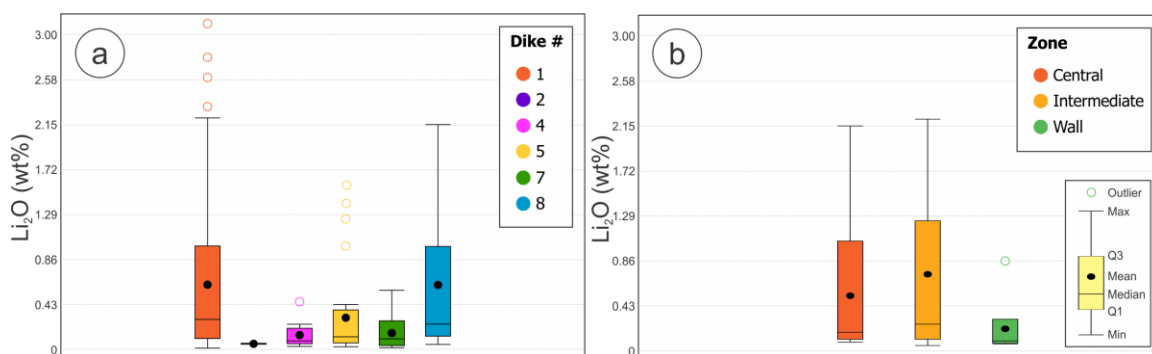
Western University. Addition petrography observations were conducted using the JEOL JMC-600 NeoScope benchtop Scanning Electron Microscope equipped with the JEOL JED-2300 energy dispersive X-ray analyser at Western University. Petrographic descriptions of all thin sections in this study are included in Appendix B.

Thin sections were carbon coated prior to single point analyses back-scatter electron (BSE) imagery and element maps were acquired using an energy dispersive spectrometer (EDS), on the JEOL JXA-8530F field-emission election probe microanalyser (EPMA) at Western University, London, ON, to determine whether individual grains were zoned. Subsequently, point analysis of major and minor elements were determined using wavelength dispersive (WDS) and EDS detectors. The microprobe operating conditions were an accelerated voltage of 15 kV and a beam current of 100 nA with a beam size of 10 µm. Analysis counting times were 60 seconds. Ten-point transects of electron microprobe analyses (EPMA) were taken from core to rim to measure intragrain variations. Mineral calibrations standards used for analysis were orthoclase (K, Al, Si), albite (Na), anorthite (Ca), olivine (Mg, Fe), pollucite (Cs), fluorite (F), rutile (Ti), and synthetic $RbTiOPO_4$ (Rb). Errors on analyses are reported on Appendix D.

Laser Ablation Inductively Coupled Plasma Mass Spectroscopy (LA-ICP-MS) of white mica was conducted at the Element and Heavy Isotope Analytical Laboratories at the University of Windsor using the Photon Machine 193 nm short pulse width Analyte Excite excimer laser ablation system coupled with an Agilent 7900 quadrupole mass spectrometer to determine trace elements and, in particular, lithium contents. Transects were taken from core to rim, as close as possible to the EPMA transects. One hundred thirty-eight traverses were completed across 67 mica grains. The data was obtained using 1.07 to 1.2 kV acceleration potential, and 4.1 mJ energy, with a beam size of 25 µm and a repetition rate of 25 hz. Background was collected for 30 seconds before an ablation time of 60 seconds. The grains were ablated with a laser fluency of ~2 J/cm^2. NIST-610 was used as the external standard. Silicon concentrations obtained from the EPMA were used as an internal standard for each grain. Errors on analyses are reported in Appendix E. Data reduction was completed using Iolite software, an add-on for Igor Pro by Wavemetrics (Paton et al., 2011). Columbite group minerals were element mapped, using

the EPMA, to determine internal zonation of Fe, Mg, Mn, Nb, Ta, Sn, Ti, U, W, and Zr. The microprobe operating conditions were an accelerated voltage of 15kV, a beam current of 100 nA, and a dwell time of 10 s.

LA-ICP-MS data collected from white micas were processed as the whole length of a traverse to obtain average values that could be used to determine the composition of the grain as a whole. Major and minor element (Si, Al, Ti, Fe, Mg, Na, K, Rb and F) data obtained from EPMA was paired to corresponding minor and trace element (Li, Ba, Mn, Cs, Be, Nb, Ta, Sn, and Tl) data obtained from LA-ICP-MS. Data points gathered from LA-ICP-MS traverses were paired with the closest EPMA spot analysis using BSE imagery.

Unpolished thin section blanks were kept for in-situ measurements using field portable instruments. The white micas targeted were from the same mica grain as the laboratory EPMA and LA-ICP-MS where possible. However, some grains were too small (<2 mm) to be manually targeted or had been completely removed during the thin section creation process. Raman measurements were performed using the DeltaNu field portable RockHound 785 nm Raman spectrometer at Western University. Samples were analysed in a low-light environment to reduce background noise in the measurements. The data was processed using PeakFit to remove background noise and to identify peaks in the spectra. Analyses were compared to reference spectra obtained from RRUFF spectral database.

Thin section blocks were also used for in-situ LIBS analysis using the handheld SciAps Z-300 LIBS Analyser at the GeoResources Laboratory at the Université de Lorraine, France. A raster of 15 analysis locations were performed on each white mica, and each analysis used four laser shots to generate one spectrum. The laser parameters cannot be modified, all spectra were obtained at a 5-6 mJ/pulse, 10 Hz repetition rate and a 1064 nm pulsed Nd-YAG laser source. The laser spot is approximately 200 μm in diameter. The Z-300 LIBS analyser produces an extended spectral range from 190 to 950 nm, and provides detection for major elements (Al, Si, O, Mg, Ca, Li, Na, K, and Fe), minor and trace elements (Be, Sr, Ba, Cs, Sn, Cs, Ta, Nd, and W) (Fabre et al., 2021). An Ar purge

is used before testing to improve precision and detection limits (Fabre et al., 2021). Spectra from the LIBS can be read and interpreted using the Profile Builder software, and elemental concentrations can be predicted using an established calibration curve.

3.4   Results

3.4.1   EPMA and LA-ICP-MS

In order to compare the Li and other elements in micas analysed by LIBS with EPMA and LA-ICP-MS, the spatial resolution of the data of the different techniques must be the same, to account for heterogeneous distribution of elements in individual mica grains. To achieve this, the EPMA and LA-ICP-MS measurements on single white mica grains were averaged, resulting in one value per grain.

Four of the eight dikes (Dike 1, Dike 5, Dike 7, Dike 8) were tested using the four techniques: EPMA, LA-ICP-MS, Raman and LIBS. The K/Rb vs Cs compositions of white micas are used to interpret the evolution of the various dikes (Figure 3.3), with increasing evolution the K/Rb ratio decreases, and the Cs abundance increases (Chpt 2). Dike 1 has a large range in both K/Rb ratio and Cs (ppm), ranging from poor to highly evolved. Dike 5 has a bimodal distribution of K/Rb ratio and Cs, with half the samples highly evolved and half poorly evolved, but the lowest Li_2O concentrations. Dike 7 has both the lowest K/Rb ratio and Cs values. Dike 8 has moderate K/Rb ratios and Cs values and follows a similar trend to Dike 1 and Dike 5. The intermediate zone, in general, has both the highest and lowest K/Rb and Cs values. Within a singular dike, the central zone tends to have higher Cs concentrations and lower K/Rb, while the wall zone has lower Cs concentrations and higher K/Rb ratios (Fig. 3.3).
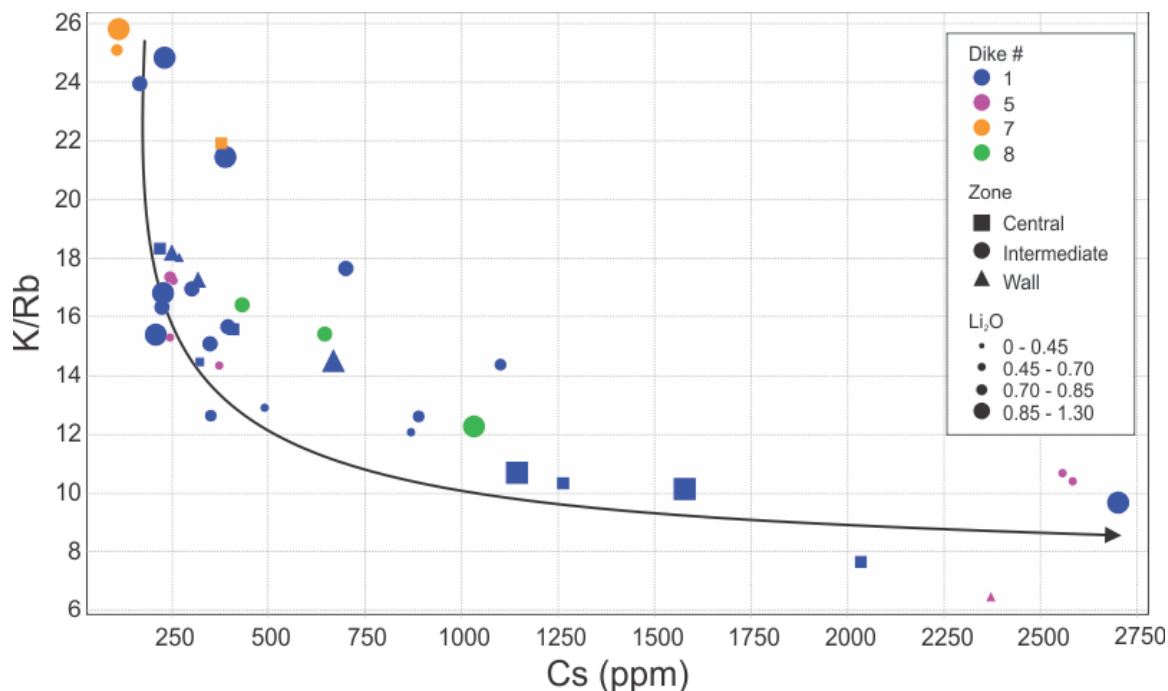
Figure 3.3: K/Rb ratio vs Cs (ppm) graph used to track the evolution of white mica. Colour represents the dike of origin, Shape represents the zone of origin, and Size represents Li contents. The black arrow dictates the general trend of evolution.

White mica grains are internally complex, and some grains have both magmatic and metasomatic portions. In chapter 2, white micas were divided into four textural groupings: poorly zoned, rimmed, patchy, and rod-shaped inclusion (RSI) hosting, based on BSE images. The brightness of BSE images is primarily caused by differences in Cs concentrations, and to a lesser extent, Fe and Mg contents. Brighter images are linked to secondary features such as fractures, and weaknesses in cleavage planes that were attributed to post-crystallization metasomatism, and the darker portions are interpreted as primary magmatic (Chpt. 2). Similar interpretations have been made by Wang et al. (2007). This can result in a large range in elemental compositions within a single grain (Figure 3.4). Patchy-textured grains have the largest chemical variation within a grain. By contrast, poorly zoned grains have very little chemical variation within a grain. The Cs content of white micas grains range from 0.01 wt% Cs_2O to 0.29 wt% Cs_2O.
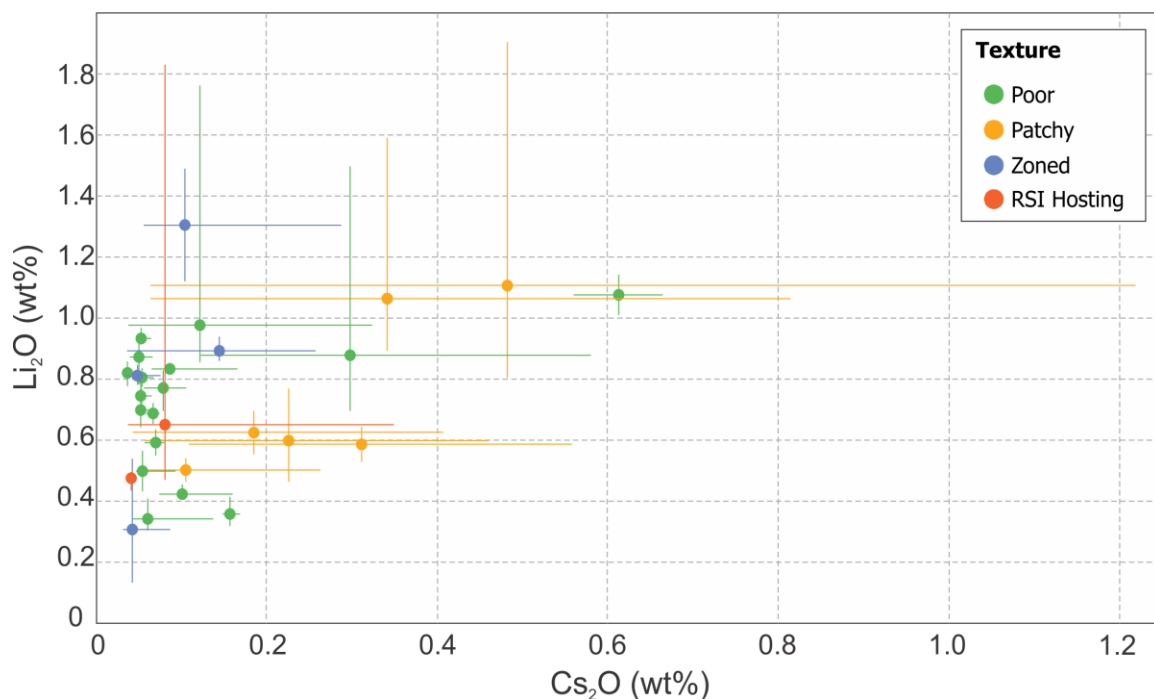
Figure 3.4: Cs_2O (wt%) vs Li_2O (wt%) graph of white mica from LA-ICP-MS analysis data. Dots represent the mean average of all the analyses on a single grain. Crosshairs extend to the highest and lowest measured concentrations on that grain.

3.4.2   LIBS

Handheld LIBS was used to determine the in-situ Li_2O concentrations of the white mica grains. A raster of 15 analysis were completed on each grain to quantify the Li_2O concentrations (Appendix H). On average, the correlation between Li_2O concentrations obtained from the LIBS and those obtained from LA-ICP-MS is relatively poor (Figure 3.5). However, this does not mean that one or both of the analyses have poor accuracy and/or precision. The two techniques sample different portions of individual grains at different scales, although the grain texture and the total Li content of the grain do not have any discernible effect on the LA-ICP-MS to LIBS Li_2O ratio. No individual dike has a LA-ICP-MS to LIBS ratio closer to 1.0 than the average of all dikes. Grains found in the wall zone appear to deviate the least from a 1:1 ratio, however, this may be due to a smaller sample size of those grains.
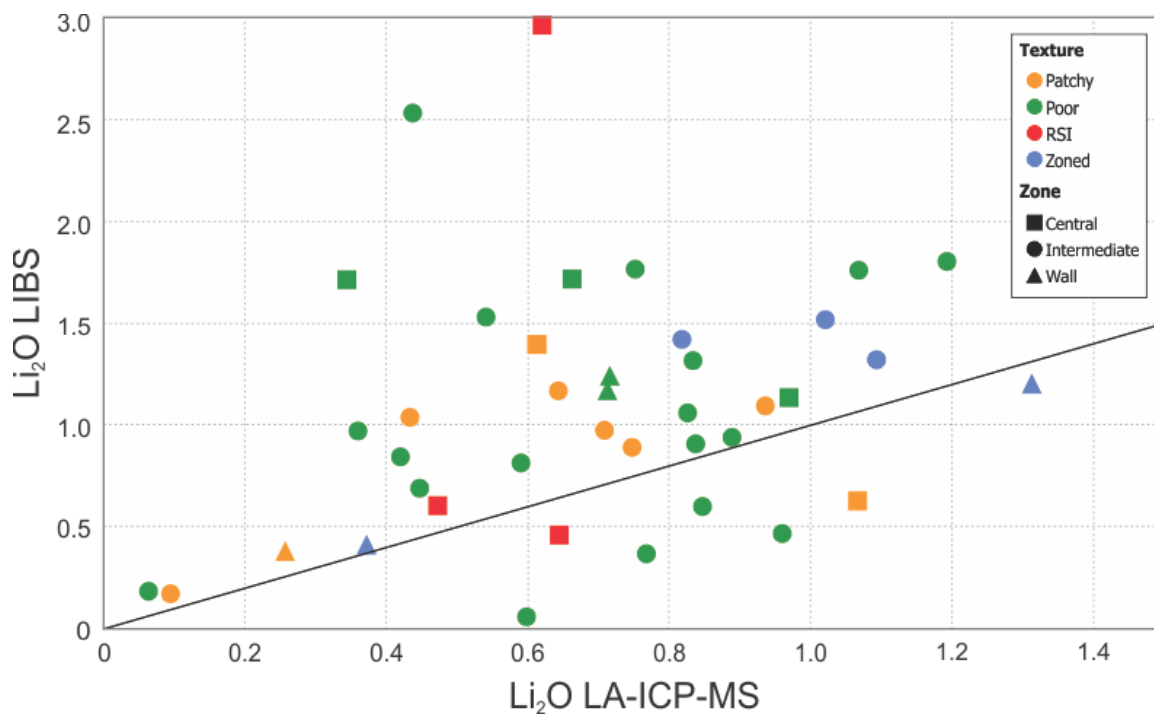
Figure 3.5: Comparison of Li_2O concentrations of white micas between LA-ICP-MS and LIBS. Black line shows slope of 1. Colour represents grain texture and shape represents zone of origin. LIBS=0.56LAICPMS+0.69 R=0.06.

The Li_2O contents of the white mica from individual dikes are compared in Figure 3.6. The LA-ICP-MS values are shown by Figure 3.6a and the LIBS values by Figure 3.6b. It is significant that the relative concentrations of Li_2O are the same using both techniques. For example, white mica from Dike 8 has the highest average content, 0.95 wt% Li_2O from LA-ICP-MS and 1.24 wt% Li_2O from LIBS. White mica from Dike 1 has the second highest Li_2O average, from both LA-ICP-MS and LIBS. Similarly white micas from Dike 5 and Dike 7 have the lowest Li_2O averages from LA-ICP-MS and LIBS analyses.
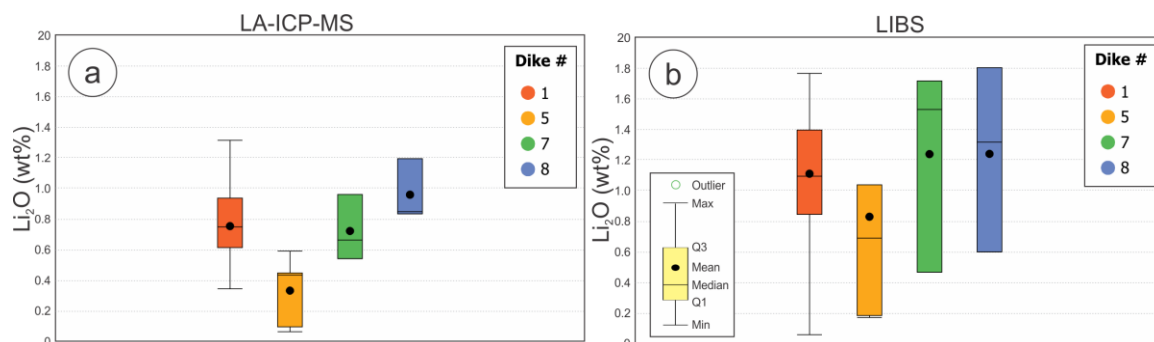
Figure 3.6: Box plots comparing Li$_2$O based on method a) LA-ICP-MS; b) LIBS.

3.4.3   Field Portable Raman spectroscopy

Raman spectroscopy is a powerful tool for identifying minerals. This study attempts to use a field portable Raman spectrometer to qualitatively distinguish between Li-rich and Li-poor muscovite grains. Muscovite forms a solid solution with polylithionite and trilithionite, with the latter as an intermediate phase. During crystallization, Li along with a divalent cation is substituted into the octahedral site for Al changing the dioctahedral muscovite into a trioctahedral polylithionite. This structural change in the mica causes peak shifts in the Raman spectra. Muscovite has three major peaks a 260, 406, and 700 cm^{-1} and three minor peaks at 193, 910 and 1112 cm^{-1} (Figure 3.7a; RRUFF, 2021a). Polylithionite has a Raman spectrum with major peaks at 182, 259, and 708 cm^{-1} and minor peaks at 401, 1056, and 1132 cm^{-1} (Figure 3.7b; RRUFF, 2021b). Trilithionite has a similar Raman spectrum to polylithionite with major peaks at 190, 263, and 711 cm^{-1} and minor peaks at 407, 1060, and 1143 cm^{-1} (Figure 3.7c; RRUFF, 2021c). The peak intensity shift between the muscovite 190 cm^{-1} and 406 cm^{-1} peaks and the polylithionite 182 cm^{-1} and 401 cm^{-1} are the most identifiable shifts in the spectra (Figure 3.7). These peaks were the focus of this study when using the field portable Raman spectrometer on Li-rich and Li-poor muscovite. Low Li muscovite grains (<0.30 wt% Li$_2$O) were compared to high Li muscovite grains (>0.30 wt% Li$_2$O) using the portable Raman spectrometer (Figure 3.8). None of the tests were able to produce spectra with the identifiable peak shift in the 190 or 406 cm^{-1} peaks (Appendix I). The resolution of the portable tool was only able to detect 264 and 700 cm^{-1} peaks above the background (Figure 3.8).
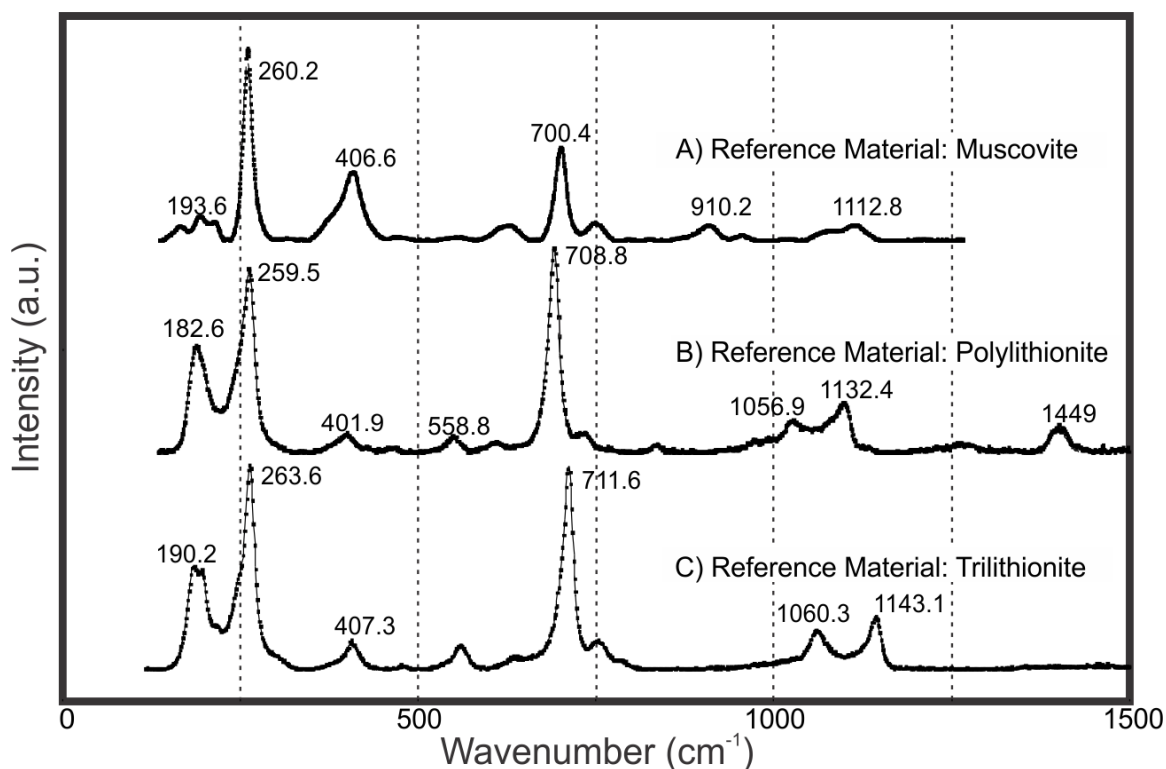
Figure 3.7: White mica reference Raman spectra comparing non-Li white mica a) Muscovite; to Li white mica b) polylithionite; c) Trilithionite.

The second Raman investigation in this study was to identify other minerals, notably feldspars. Pegmatites are host to many minerals that are easily misidentified. The pegmatite dikes in the Wekusko Lake pegmatite field have undergone hematization, causing many white minerals to appear red or pink (Figure 3.9a). This was most problematic when trying to identify albite and K-feldspar in the wall and intermediate zones. In these zones, albite is red instead of the typical white (Figure 3.9a). Raman spectroscopy uses variation in molecular bonds to distinguish minerals, thus ignoring visual anomalies in mineral identification. The Raman spectrum for microcline (K-feldspar) has major peaks at 476 and 511 cm^{-1} (Figure 3.9a; RRUFF, 2021d) whereas albite has major peaks at 289, 478 and 506 cm^{-1} (Figure 3.9b; RRUFF, 2021e). The red feldspar was tested using the field portable Raman spectrometer and major peaks were identified at 293, 479 and 506 cm^{-1} (Figure 3.9c), matching the Raman shift of albite.
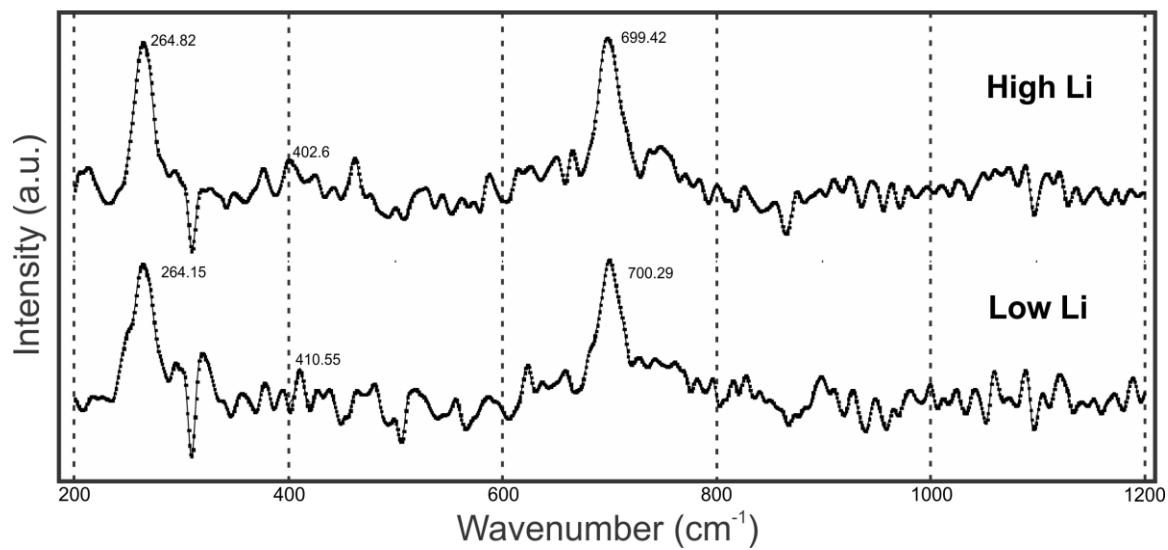
Figure 3.8: Comparison of a high Li (1.29 wt% Li$_2$O) to a low Li (0.29 wt% Li$_2$O) muscovite grain from Wekusko Lake.
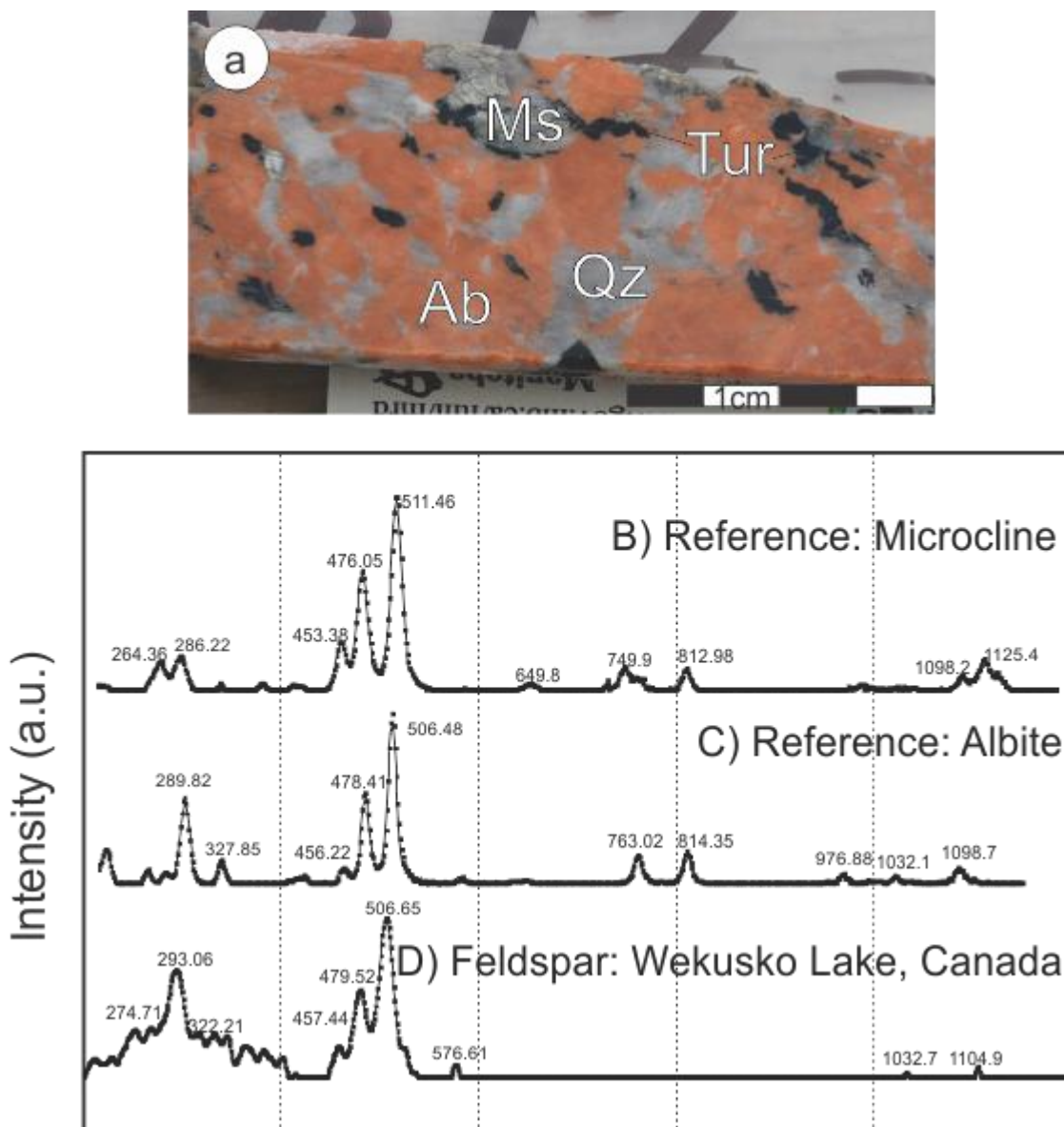
Figure 3.9: a) Photograph of hematite-stained albite from Wekusko Lake, Mb. Raman spectra of reference b) microcline; c) albite; compared to d) red albite.

3.5   Discussion

3.5.1   Mica geochemistry

The dikes in the Wekusko Lake pegmatite were ranked based on the average Li (ppm) whole rock assays and the projected thickness based on field mapping and drill core logs. These rankings were used to estimate prospectivity and may also fall victim to the

heterogeneity and nugget effect commonly found in pegmatites. Dike 1 has been drilled the most and has the most mica samples. The micas display a range in the degree of evolution (K/Rb vs Cs) and increasing evolution correlates with increasing Li (Figure 3.3). The micas for Dike 8 overlap with the evolution trend for Dike 1 and both have similar Li_2O values (Figure 3.3). These dikes also have the highest and greatest range in Li_2O contents within the white micas, which correlates with the whole rock Li assay concentrations (Figure 3.10a). Dike 7 has the similar whole rock Li assay values and the white micas Li_2O contents to Dike 1 and Dike 8. However, the white micas from Dike 7 plot as less evolved than Dike 1 and Dike 8 (Figure 3.3; Figure 3.10a). The evolution trends for Dike 4 and Dike 2 are similar and indicate a low degree of evolution and low Li_2O. Fewer samples from Dike 5 were analysed and half the samples plot as less evolved and the other half as highly evolved (Figure 3.3). Dike 5 has substantially lower Li_2O in the white micas compared to the other dikes, and it is lower than expected when compared to the whole rock Li assays (Figure 3.10). There is little change in Li_2O content of the white mica from the wall to the central zone in all the pegmatites, despite whole rock Li assay values increasing from the wall to central zone (Figure 3.2). The increased Li whole rock values are interpreted to reflect the higher spodumene content of the intermediate and central zones. The near-constant Li values in the white micas could suggest that Li is being buffered by more favourable phases such as Li-aluminosilicates (e.g., spodumene, petalite and eucryptite) in the central and intermediate zone (Stewart, 1978; Maneta et al., 2015). This could be one explanation for the low Li_2O concentrations in the white mica compared to the whole rock Li in Dike 5. Muscovite grains from Dike 5 plot among the most evolved samples on a K/Rb vs Cs graph (Figure 3.3). The crystallization of Li-aluminosilicates in pegmatites does not occur once the melt reaches supersaturation and may require supersaturation of thousands of ppm above saturation to crystallize (Maneta et al., 2015). The saturation of the melt is temperature dependent. A melt at 500°C reaches Li saturation at approximately 5000 ppm and supersaturation at approximately 6250 ppm, whereas a melt at 700°C reaches Li saturation at approximately 7000 ppm, and supersaturation at 16000 ppm (Maneta et al., 2015). Once spodumene starts to crystallize (from a supersaturated melt) the Li content will decrease, as spodumene crystallizes until the Li content of the melt reaches the Li

saturation value. If micas did not continuously crystallize with spodumene, the Li content of the mica likely reflects the Li content of the melt at the end of the spodumene crystallization and the mineral-melt partition coefficient for Li and mica. Lower Li values in mica either reflect lower temperatures, and lower concentrations of Li in melts for saturation, or Li values for melts that are not high enough to crystallized spodumene, or other lithium aluminosilicates. This may help explain why the Li content of the muscovite in Dike 5 is lower compared to other the dikes. A 50°C change in temperature would be enough to account for the 2000 ppm Li difference between Dike 5 and Dike 7 muscovite (Maneta et al., 2015). Compared to other dikes, the muscovite in Dike 5 has higher concentrations of Ta and Cs but lower abundances of Be, and Nb. The lower Be in muscovite could be due beryl having crystallized before mica (Trueman and Cerny, 1982; Smeds, 1992; Evensen and London, 2002), depleting the melt of Be. However, this is hard to determine with certainty without a more in-depth study of the beryls.
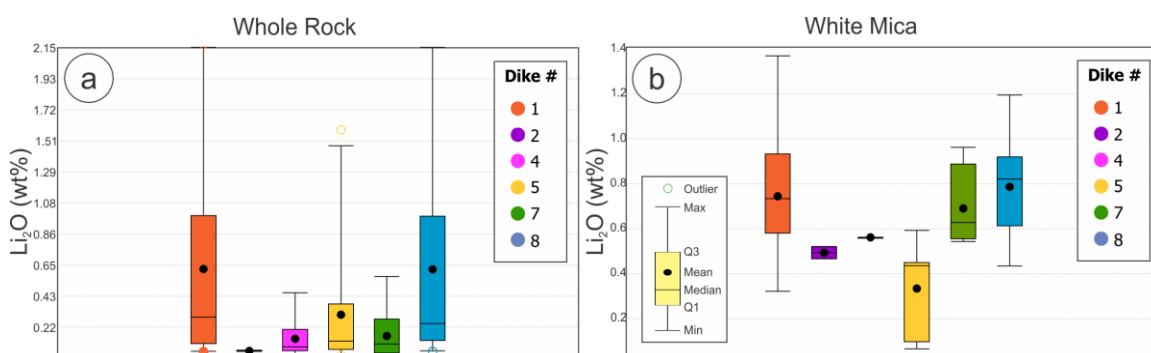

Figure 3.10: Box plot comparison of Li_2O between a) Whole rock assays; and b) White micas.

3.5.2   LIBS

The correlation between the Li concentrations obtained from the handheld LIBS and those obtained from the LA-ICP-MS is poor (Figure 3.5). Mass spectrometers quantify data by measuring the electrical flow through the faraday cups as ionized particles pass

through. On the other hand, LIBS measures the intensity of the spectral output from the plasma. This works well for comparing elements within a sample, but quantification requires special calibration. The emission spectra generated during LIBS analysis is affected by the physical and chemical matrix of the material. The physical characteristics such as, grain size, opacity, crystallinity, hardness, coherence, porosity, surface texture, moisture content, absorptivity, thermal conductivity, and reflectivity, all affect the intensity of the spectra generated (Eppler et al., 1996; Gornushkin et al., 2002; Harmon and Senesi, 2021). Chemical matrix effects occur when the emissions from one element interfere with the emissions from another element (Russo et al., 1995; Harmon and Senesi., 2021). These matrix effects make calibrating LIBS for quantification more challenging. Thus, there is an expected decoupling of quantified LIBS data from LA-ICP-MS data. Additional analyses will be needed to explain the poor correlation between LIBS and LA-ICP-MS analyses.

However, in practical terms the LIBS and LA-ICP-MS tell a similar story, despite the lack of good linear correlation. Figure 3.6 compares the Li concentrations of micas between the dikes using both LIBS and LA-ICP-MS. Both graphs show that Dike 5 has the lowest Li concentrations, Dike 8 has the highest Li concentrations and that there is a sizable overlap of values between Dike 1, Dike 7, and Dike 8. The most significant difference between the LIBS and LA-ICP-MS is the standard deviation (Figure 3.6). While standard deviation an important factor in the confidence placed in a technique, it is not reasonable to compare the standard deviation of a handheld technique to laboratory technique. Given that the relative changes in abundances from LIBS and LA-ICP-MS are the same, it can be concluded that LIBS will be an effective tool that can be used in the field to rank dikes and decide which dikes warrant more detailed exploration.

3.5.3   Field Portable Raman Spectrometer

The presence of Li rich micas is used to distinguish zones of mineralization in some pegmatites, e.g., the lepidolite zone at Tanco (Trueman and Cerny, 1982; Cerny and Ercit, 2005; Cerny, 2005). Chapter 2 has shown how white mica make changes from a dioctahredal mica to a trioctahedral mica when incorporating Li into the molecular

structure. Reference spectra (Figure 3.7; RRUFF, 2021a;b;c) of muscovite-trilithionite solid solution series show how this structural change is reflected in Raman spectra. However, the handheld device used to analyse the white mica samples in this study could not detect a noticeable difference in spectra.

Hand sample mineral identification can be problematic in many pegmatites. There are many amorphous white minerals to distinguish such as albite, microcline, spodumene, beryl, petalite, pollucite, and amblygonite. The presence of these minerals, especially albite and K-feldspar, are used for characterizing pegmatites (Trueman and Černý, 1982; Černý and Ercit, 2005). In this case study, hematization stained many of those minerals red and hid subtle characteristics. The handheld Raman spectrometer was easily able to distinguish these minerals.

3.6   Conclusion

Muscovite is a common mineral within pegmatites, which can be used to estimate the fractionation levels of the host pegmatite. In this study it was possible to use the Li content of muscovite to distinguish between high Li-bearing pegmatites and low Li-bearing pegmatites using LA-ICP-MS. However, the zones (e.g., wall, intermediate or central) within an individual pegmatite were not identifiable using the Li content of muscovite. Furthermore, the degree of undercooling present during crystallization can greatly affect the Li-content of the mica while have having minimal effect on whole rock assays (which is largely reflective of spodumene content of the rock). For the purposes of general pegmatite exploration, it is less efficient and more costly to determine the Li contents of mica by LA-ICP-MS compared to LIBS. The handheld LIBS produced higher Li-concentrations than those obtained from LA-ICP-MS and had a larger standard deviation but was still able to reproduce similar results. The practicality and applications of LIBS will increase as more calibrations and standards become widely available.

The handheld Raman was not able to distinguish between the high Li-muscovite and low Li-muscovite in the studied pegmatites. However, it may still be useful for projects with larger variations in Li content in muscovite, or hard to identify lepidolite (typically with

very high Li content). The handheld Raman is a powerful tool for identifying minerals as it is capable of identifying mineral polymorphs or minerals containing light and heavy elements. The high speed and low impact nature of the information obtained from the handheld Raman would be ideal if it were automated or couple with other techniques (e.g., Corescan).

3.7   References

Benn, D., Martins, T., Linnen, R., Ziehlke, J. and Singh, J. 2018a. Bedrock geology of the Wekusko Pegmatite field (northeastern block), central Manitoba (parts of NTS 63J13); Manitoba Growth, Enterprise, and Trade, Preliminary Map PMAP2018-2, scale 1:4000.

Benn, D., Linnen, R.L. and Martins, T. 2018b. Geology and bedrock mapping of the Wekusko Lake pegmatite field (northeastern block), central Manitoba (part of NTS 63J13); *in* Report of Activities 2018, Manitoba Growth, Enterprise and Trade, Manitoba Geological Survey,: 79–88.

Beurlen, H., Müller, A., Silva, D., and da Silva, M.R.R. 2011. Petrogenetic significance of LAICP-MS trace-element data on quartz from the Borborema Pegmatite Province, northeast Brazil. Mineral. Mag., **75**: 2703–2719.

Beurlen, H., Thomas, R., da Silva, M.R.R., Müller, A., Rhede, D., and Soares, D.R., 2014. Perspectives for Li-and Ta-mineralization in the Borborema Pegmatite Province, NE Brazil: a review. J. S. Am. Earth Sci., **56**: 110–127.

Beus, A.A., Berengilova, V.V., Grabovskaya, L.I., Kochemasov, L.A., Leontéva, L.A. and Sitnin, A.A., 1968. Geochemical prospecting for endogenous ore deposits of rare elements (e.g. for tantalum): Academy of Science USSR, Dept. of Geology of USSR, Institute of Mineralogy, Geochemistry and Crystal Chemistry of Rare Elements, Moscow, USSR. (translated by the Department of the Secretary of State, Ottawa, Canada, 429 p.).

Bowell, R.J., Lagos, L., de los Hoyos, C., and Declercq, J. 2020. Classification and characteristics of natural lithium resources. Elements, **16**: 259-264.

Bradley, D.C., McCauley, A.D., and Stillings, L.M. 2017. Mineral-Deposit Model for Lithium-Cesium-Tantalum Pegmatites. U.S. Geological Survey, Scientific Investigations Report 2010–5070–O,: 48.

Cardoso-Fernandes, J., Silva, J., Perrotta, M.M., Lima, A., Teodoro, A.C., Ribeiro, M.A., Dias, F., Barrès, O., Cauzid, J., and Roda-Robles, E. 2021. Interpretation of the Reflectance Spectra of Lithium (Li) Minerals and Pegmatites: A Case Study for Mineralogical and Lithological Identification in the Fregeneda-Almendra Area. Remote Sens., **13**: 3688.

Černý, P. 1989. Characteristics of pegmatite deposits of tantalum. In Lanthanides, Tantalum and Niobium; Černý, P., Möller, P., Saupe, F.,Eds.; Springer: Berlin/Heidelberg, Germany,: 195–239.

Černý, P. and Ercit, T. 2005. The classification of granitic pegmatites revisited; The Canadian Mineralogist, **43**: 2005–2026.

Clark, J.R. 1993. Enzyme-induced leaching of B-horizon soils for mineral exploration in areas of glacial overburden: Transactions of Institution of Mining and Metallurgy (Sect. B: Applied Earth Sciences), **102**: B19-29.

Clark, J.R. 1997. Concepts and Models for Interpretation of Enzyme LeachSMEnzyme Leach Data for Mineral and Petroleum Exploration: Enzyme LeachSM Enzyme Leach, Model, Sampling Protocol and Case Histories, Activation Laboratories, Toronto,: 62.

Connors, K., Ansdell, K. and Lucas, S. 2002. Development of a transverse to orogen parallel extension lineation in a complex collisional setting, Trans-Hudson Orogen, Manitoba, Canada; Journal of Structural Geology, **24**: 89–106.

Connors, B. Somers, A. and Day, D. 2016. Application of handheld laser-induced breakdown spectroscopy (LIBS) to geochemical analysis. Appl. Spectrosc., **70**: 810–815.

Darbyshire, F., Bastow, I., Petrescu, L., Gilligan, A., and Thompson, D. 2017. A tale of two orogens: Crustal processes in the Proterozoic Trans-Hudson and Grenville Orogens, eastern Canada. Tectonics, **36**: 1633–1659.

Dart Mining NL, 2021: LiDAR Mapping of the Dorchap Dyke Swarm Points Towards Increase in Lithium Pegmatites. https://www.listcorp.com/asx/dtm/dart-mining/news/lidar-points-towards-increase-in-lithium-pegmatites-2619048.html, [Accessed March 2022]

Deveaud, S., Gumiaux, C., Gloaguen, E., and Branquet, Y. 2013. Spatial statistical analysis applied to rare-element LCT-type pegmatite fields: an original approach to constrain faults–pegmatites–granites relationships, Journal of Geosciences. **58**: 163-182.

Eaton, D., and Darbyshire, F. 2010. Lithospheric architecture and tectonic evolution of the Hudson Bay region. Tectonophysics, **480**: 1-22.

Eppler, A.S., Cremers, D.A., Hickmott, D.D., Ferris, M.J., and Koskelo, A.C., 1996. Matrix effects in the detection of Pb and Ba in soils using laser-induced breakdown spectroscopy. Appl. Spectrosc., **50**: 1175–1181.

Fabre, C., Ourti, N., Mercadier, J., Cardoso-Fernandes, J., Dias, F., Perrotta, M., Koerting, F., Lima, A., Kaestner, F., Koellner, N., Linnen, R., Benn, D., Martins, T., and Cauzid, J., 2021. Analyses of Li-rich minerals using handheld LIBS tool. Data, **6**: 68.

Fortes, F.J., and Laserna, J.J. 2010. The development of fieldable laser-induced breakdown spectrometer: No limits on the horizon. Spectrochimica Acta Part B: Atomic Spectroscopy, **65**: 975–990.

Fyzollahhi, N., Torshizian, H., Afzal, P., and Jafari, M.R. 2018. Determination of lithium prospects using fractal modeling and staged factor analysis in Torud region, NE Iran. Journal of geochemical Exploration, **189**: 2-10.

Galeschuk, C.R. 2001. Report on 2000-2001 diamond drill report, Separation Lake, Ontario (52 L/8 SW): Ontario Assessment Report, Tantalum Mining Corporation of Canada Limited, Lac du Bonnet, Manitoba,: 17.

Galeschuk, C.R., and Vanstone, P.J. 2005. Exploration for buried rare-element pegmatites in the Bernic Lake area of southeastern Manitoba; *in* Rare-Element Geochemistry and Mineral Deposits, R.L. Linnen and I.M. Samson (ed.), Geological Association of Canada, Short Course Notes, **17**: 153–167.

Gałuszka, A., Migaszewski Z.M., and Namieśnik, J. 2015. Moving your laboratories to the field – Advantages and limitations of the use of field portable instruments in environmental sample analysis. Environmental Research, **140**: 593–603.

Gordiyenko, V.V. 1971. Concentrations of Li, Rb, and Cs in potash feldspar and muscovite as criteria for assessing the rare-metal mineralization in granite pegmatites. Int. Geol. Rev., **13**: 134–142.

Gornushkin, S.I., Gornushkin, I.B., Anzano, J.M., Smith, B.W., and Winefordner, J.D. 2002. Effective normalization technique for correction of matrix effects in laser-induced breakdown spectroscopy detection of magnesium in powdered samples. Appl. Spectrosc., **56**: 433–436.

Grammatikopoulos, T., Aghamirian, M., Fedikow, M. and Mayo, T. 2020. Mineralogical Characterization and Preliminary Beneficiation of the Zoro Lithium Project, Manitoba, Canada. Mining, Metallurgy & Exploration **38,** 329–346.

Hammer, P., Clowes, R., Cook, F., Van Der Velden, A., and Vasudevan, K. 2010. The Lithoprobe trans-continental lithospheric cross sections: imaging the internal structure of the North American continent. Can. J. Earth Sci., **47**: 821-857.

Hark, R. R., and Harmon, R. S. 2014. Geochemical Fingerprinting Using LIBS, in Musazzi, S., and Perini, P., eds., Laser-Induced Breakdown Spectroscopy - Theory and Applications, **182**: Berlin Heidelberg, Springer, 309-348.

Harmon, R.S., Russo, R.E., and Hark, R.R. 2013. Applications of laser-induced breakdown spectroscopy for geochemical and environmental analysis: A comprehensive review. Spectrochimica Acta Part B: Atomic Spectroscopy, **87**: 11-26.

Harmon, R.S., Khashchevskaya, D., Morency, M., Owen, L.A., Jennings, M., Knott, J.R., and Dortch, J.M. 2021. Analysis of rock varnish from the Mojave Desert by handheld laser-induced breakdown spectroscopy. Molecules, **26**: 5200.

Hoffman, P. 1988. United Plates of America, the birth of a craton: Early Proterozoic assembly and growth of Laurentia; Annual Review of Earth and Planetary Sciences, **16**: 543–603.

Hoffman, P. 1989. Precambrian geology and tectonic history of North America; *in* The Geology of North America—an overview, A.W. Bally and A.R. Palmer (ed.); Geological Society of America, The Geology of North America, **A**, 447–512.

Hope, G.A., Woods, R., and Munce, C.G. 2001. Raman microprobe mineral identification: Minerals Engineering, **14**: 1565–1577.

Kesler, S.E., Gruber, P.W., Medina, P.A., Keoleian, G.A., Everson, M.P., and Wallington, T.J. 2012. Global lithium resources: Relative importance of pegmatite, brine and other deposits. Ore Geology Reviews, **48**: 55-69.

Lemière, B. 2015. Field Analytical Techniques for Geochemical Surveys. Keynote conference, 27th International Applied Geochemistry Symposium, Tucson, Azrizona, USA

Lemière, B. 2018. A review of applications of pXRF (field portable X-ray fluorescence) for applied geochemistry. Journal of Geochemical Exploration, **188**: 350–363.

Lemière, B., and Uvarova, YA, 2019. New developments in field portable geochemical techniques and on-site technologies and their place in mineral exploration. Geochemistry Exploration Environment Analysis. **20**: 205- 216.

Lewry, J., Hajnal, Z., Green, A., Lucas, S., White, D., Stauffer, M., Aston, K., Weber, W., and Clowes, R. 1994. Structure of Paleoproterozoic continent-continent collision zone: LITHOPROBE seismic reflection profiles across the Trans-Hudson orogen. Tectonophysics, **232**: 143–160.

Linnen, R.L., Galeschuk, C. and Halden, N.M. 2015. The use of fracture minerals to define metasomatic aureoles around rare-metal pegmatites; 27th International Applied Geochemistry Symposium, Tucson, Arizona,

Maneta, V., Baker, D.R., and Minarik, W. 2015. Evidence for lithium-aluminosilicate supersaturation of pegmatite-forming melts. Contrib. Mineral. Petrol., **170**: 4.

Maneta, V., and Baker, D. 2019. The potential of lithium in alkali feldspars, quartz, and muscovite as a geochemical indicator in the exploration for lithium-rich granitic pegmatites: A case study from the spodumene-rich Moblan pegmatite, Quebec, Canada. Journal of geochemical exploration. **205**: 106336.

Maurice, S., Wiens, RC., Bernardi, P., Caïs, P., Nelson, T., Gasnault, O., Reess, JM., et al. 2021. The SuperCam Instrument Suite on the Mars 2020 Rover: Science Objectives and Mast-Unit Description. Space Sci Rev., **217**: 47.

Mernagh, T.P., and Trudu, A.G. 1993. A laser Raman microprobe study of some geologically important sulphide minerals: Chemical Geology, **103**: 113–127.

Mohr, S., Mudd, G., and Giurco, D. 2012. Lithium Resources and Production: Critical Assessment and Global Projections. Minerals., **2**: 65-86

Morgan VI, G.B., and London, D. 1987. Alteration of amphibolitic wallrocks around the Tanco rare-element pegmatite, Bernic Lake, Manitoba. Am. Mineral., **72**: 1097–1121.

Ovchinnikov, L.N. 1976. Lithochemical methods of prospecting rare metal pegmatites: Academy of Science USSR, Dept. of Geology of USSR, Institute of Mineralogy, Geochemistry and Crystal Chemistry of Rare Elements, Moscow, USSR. (translated by the Department of the Secretary of State, Ottawa, Canada, 96 p.).

Pasteris, JD., and Beyssac, O. 2020. Welcome to Raman Spectroscopy: Successes, Challenges, and Pitfalls. Elements, **16**: 87-92.

Paton, C., Hellstrom, J., Paul, B., Woodhead, J., and Hergt, J. 2011. Iolite: Freeware for the visualisation and processing of mass spectrometric data. Journal of Analytical Atomic Spectrometry, **26**: 2508–2518.

RRUFF[TM]. 2021a. *Muscovite R040104*. URL <http://rruff.info/muscovite/display=default/R040104> [March 2021]

RRUFF[TM]. 2021b. *Polylithionite R050132*. URL <http://rruff.info/polylithionite/display=default/R050132> [March 2021]

RRUFF[TM]. 2021c. *Trilithionite R040101*. URL <http://rruff.info/trilithionite/display=default/R04010> [March 2021]

RRUFF[TM]. 2021d. *Microcline R040154*. URL <https://rruff.info/Microcline/R040154> [March 2021]

RRUFF[TM]. 2021e. *Albite R040068*. URL < https://rruff.info/Albite/R040068> [March 2021]

Russo, R.E., Chan, W.-T., Bryant, M.F., and Kinard, W.F. 1995. Laser ablation sampling with ICP-AES for the analysis of prototypic glasses. J. Anal. At. Spectrom., **10**: 295–301.

Ryan J.G., Shervais, J.W., Li, Y., Reagand, M.K., Li, H.Y., Heaton, D., Godard, M., Kirchenbaur, M., Whattami, S.A., Pearce, J.A., Chapman, T., Nelson, W., Prytulak, J., Shimizu, K., Petronotis, K. and the IODP Expedition 352 Scientific Team, 2017. Application of a handheld X-ray fluorescence spectrometer for real-time, high-

density quantitative analysis of drilled igneous rocks and sediments during IODP Expedition 352. Chemical Geology, **451**: 55–66.

Schneider, D., Heizler, M., Bickford, M., Wortman, G., Condie, K. and Perilli, S. 2007. Timing constraints of orogeny to cratonization: thermochronology of the Paleoproterozoic Trans-Hudson orogen, Manitoba and Saskatchewan, Canada; Precambrian Research, **153**: 65–95.

Selway, J.B., Breaks, F.W., Tindle, A.G. 2005. A review of rare-element (Li-Cs-Ta) pegmatite exploration techniques for the Superior Province, Canada, and large worldwide tantalum deposits. Explor. Min. Geol., **14**: 1–30.

Shearer, C.K., Papike, J.J., Simon, S.B. and Laul, J.C. 1986. Pegmatite wallrock interactions, Black Hills, South Dakota: interaction between pegmatite-derived fluids and quartz-mica schist wallrock; American Mineralogist, **71**: 518–539.

Sinclair, W.D. 1995. Granitic pegmatites. In: Eckstrand OR, Sinclair WD, Thorpe RI (eds) Geology of Canadian Mineral Deposit Types. Geological Survey of Canada,: 503-512.

Skupio, R. 2020. Portable XRF spectrometer with helium flow as a tool for lithological interpretation. Geology, Geophysics and Environment, **46**: 315-320.

Smeds, S.A. 1992. Trace elements in potassium-feldspar and muscovite as a guide in the prospecting for lithium- and tin-bearing pegmatites in Sweden. J. Geochem. Explor., **42**: 351–369.

Steiner, B.M. 2019. Tools and Workflows for Grassroots Li–Cs–Ta (LCT) Pegmatite Exploration. Minerals. **9**: 499.

Sterba, J., Krzemień, A., Fernández, R.R., García-Miranda, C.E., Valverde, G.F. 2019. Lithium mining: accelerating the transition to sustainable energy. Resources Policy, **62**: 416-426.

Stewart, D.B. 1978. Petrogenesis of lithium-rich pegmatites. Am. Mineral., **63**:970–980.

Sweetapple M.T., and Tassios, S. 2015. Laser-induced breakdown spectroscopy (LIBS) as a tool for in situ mapping and textural interpretation of lithium in pegmatite minerals. American Mineralogist. **100**: 2141-2151.

Trueman, D. L., and Černý, P. 1982. Exploration for rare-metal granitic pegmatites, *in* Černý, P., ed., Granitic Pegmatites in Science and Industry, Mineralogical Association of Canada, Short Course Handbook, **8**: 463-493.

Wang, R., Hu, H., Zhang, A., and Fontan, F. 2007. Cs-dominant polylithionite in the Koktokay#3 pegmatite, Altai, NW China: in situ micro-characterization and implication for the storage of radioactive cesium. Contrib. Mineral. Petrol., **153**: 355–367.

Wise, M.A., Harmon, R.S., Curry, A., Jennings, M. Grimac, Z., and Khashchevskaya, D. 2022. Handheld LIBS for Li Exploration: An Example from the Carolina Tin-Spodumene Belt, USA. Minerals, **12**: 77.

Xu, Z., Liang, B., Geng, Y., Liu, T., and Wang, Q. 2019: Extraction of soils above concealed lithium deposits for rare metal exploration in Jiajika area: A pilot study. Applied Geochemistry. **107**: 142-151.

Young, K.E., Evans, C.A., Hodges, K.V., Bleacher, J.E., and Graff, T.G. 2016. A review of the handheld X-ray fluorescence spectrometer as a tool for field geologic investigations on Earth and in planetary surface exploration. Applied Geochemistry, **72**: 77-87.

Zhang, W., Lentz, D.R., and Charnley, B.E. 2017. Petrogeochemical assessment of rock units and identification of alteration/mineralization indicators using portable X-ray fluorescence measurements: Applications to the Fire Tower Zone (W-Mo-Bi) and the North Zone (Sn-Zn-In), Mount Pleasant deposit, New Brunswick, Canada. Journal of Geochemical Exploration, **177**: 61–72.

Chapter 4

4   Conclusion

White micas are a useful mineral for determining the degree of evolution in pegmatites. This was achieved using K/Rb ratios paired with an incompatible element such as Cs. Decreasing K/Rb and increasing Cs is a sign of increasing evolution. The modelling of fractional crystallization of white micas in pegmatites using these trace elements determined that the pegmatites are a result of 99% to 99.99% crystallization of a granitic melt. These models were not able to account for the highest levels of Cs observed in the white micas. This Cs enrichment was coupled with textural variations observed in backscatter imagery. This suggests that Cs-enrichment is a result of post-magmatic interaction with a secondary fluid. The increased evolution of the white mica was also linked to increased Li contents. Lithium is enriched in white micas through a combination of octahedral Li-fixation and phengitic substitution.

The link between increased evolution and increased Li content makes white mica a potential indicator mineral for Li-bearing pegmatites. Dike 1 and Dike 8 show the greatest potential for Li-mineralization, based on whole rock Li content from assays. The white micas from these dikes have the greatest Li-content. The micas from the Li-rich central zone were not identifiable from the micas in the wall or intermediate zone. These observations were made using both LA-ICP-MS and LIBS. While the LA-ICP-MS data had more precision than the LIBS, the same conclusions could be made from both data sets. It can be difficult to quantify Li data from LIBS analyses due to limited calibration curves. However, in an exploration setting quantification may not be necessary if the LIBS is being used to comparatively. Distinguishing between high and low Li white mica, based on intensity, may be sufficient for the majority of samples and final Li values can be obtained through standard methods. It was not possible to distinguish between a high Li mica and a low Li mica in this study using Raman spectroscopy. However, Raman spectroscopy can be used to identify other minerals and it may have a role in

some petalite-bearing pegmatites. However, it would not be practical in the majority of Li-exploration projects.

4.1 Future works

To further the understanding of Li substitution into white micas a Fe^{2+}/Fe^{3+} micro-XANES study. This can provide further support for the potential deprotonation theorized in Chapter 2. There is little literature in fluid-mica recrystallization outside of equilibrium with the melt. Potential fluid-mineral partition coefficients for mica-fluid outside of equilibrium with the melt would make it possible to create a model to explain the Cs enrichment presently unexplained by traditional Rayleigh's crystal fractionation models. Further investigation into disequilibrium partitioning of Li in supersaturated melts would explain the high Li in whole rock and low Li in micas observed in Dike 5. Techniques like LIBS would benefit from the continued work on calibration curves and expanded standards libraries.

Curriculum Vitae

Name: David Benn

Post-secondary   University of Ottawa
Education and   Ottawa, Ontario, Canada
Degrees: 2014-2018 HB.Sc.

                     The University of Western Ontario
                     London, Ontario, Canada
                     2018-Present M.Sc.

Related Work   Student Geologist
Experience   FAR Resource Ltd.
                     July-August 2018

                     Graduate Teaching Assistant
                     Western University
                     2018-2019

Publications:

Benn, D., Linnen, R.L. and Martins, T. 2018. Geology and bedrock mapping of the Wekusko Lake pegmatite field (northeastern block), central Manitoba (part of NTS 63J13); in Report of Activities 2018, Manitoba Growth, Enterprise and Trade, Manitoba Geological Survey,: 79–88.

Benn, D., Martins, T., Linnen, R.L., Ziehlke, J. and Singh, J. 2018. Bedrock geology of the Wekusko Lake pegmatite field (northeastern block), central Manitoba (part of NTS

63J13); Manitoba Growth Enterprise and Trade, Preliminary Map PMAP2018-2, scale 1:4000.

Benn, D., Linnen, R.L., and Martins, T. 2018. Geology and bedrock mapping of the Wekusko Lake pegmatite field, central Manitoba. Central Canada Mineral Exploration Convention (CCMEC), (Poster).

Benn, D., Martins, T. and Linnen, R.L. 2019. Interpretation of U-Pb isotopic dates of columbitegroup minerals in pegmatites, Wekusko Lake pegmatite field, central Manitoba (part of NTS 63J13); in Report of Activities 2019, Manitoba Agriculture and Resource Development, Manitoba Geological Survey,: 52–59.

Benn, D., Linnen, R.L, and Martins, T. 2019. Evaluating portable Raman spectrometers for use in exploration of pegmatite dikes, Wekusko Lake, Manitoba. The Canadian Mineralogist, **57**: 711–713.

Benn, D., Linnen, R.L, and Martins, T. 2019. Evaluating Portable Raman Spectrometers for use in Exploration of Pegmatite Dikes, Wekusko Lake, Manitoba, Canada. Pegmatite Symposium (PEG), (Poster).

Martins, T., Benn, D. and McFarlane, C. 2019. Laser ablation-inductively coupled plasma-mass spectrometry (LA-ICP-MS) analyses of columbite grains from Li-bearing pegmatites, Wekusko Lake pegmatite field (northeastern block), central Manitoba (part of NTS 63J13); Manitoba Growth, Enterprise and Trade, Manitoba Geological Survey, Data Repository Item DRI201900#, Microsoft® Excel® file.

Benn, D., Linnen, R.L, and Martins, T. 2019. Evaluating Muscovite as an indicator mineral for lithium bearing pegmatites, Wekusko Lake, central Manitoba. Central Canada Mineral Exploration Convention (CCMEC), (Technical Speaker).

Benn, D., Linnen, R.L, and Martins, T. 2020. Evaluating Muscovite as an indicator mineral for lithium bearing pegmatites, Wekusko Lake, central Manitoba. AME RoundUp, (Poster).

Benn, D., Linnen, R.L, and Martins, T. 2020. Evaluating Muscovite as an indicator mineral for lithium bearing pegmatites, Wekusko Lake, central Manitoba. Prospectors & Developers Association of Canada (PDAC), (Poster).

Benn, D., Linnen, R.L, and Martins, T. 2020. Evaluating Muscovite as an indicator mineral for lithium bearing pegmatites, Wekusko Lake, central Manitoba. GAC-MAC GeoConvention, (Technical Speaker).

Fabre, C., Ourti, N., Mercadier, J., Cardoso-Fernandes, J., Dias, F., Perrotta, M., Koerting, F., Lima, A., Kaestner, F., Koellner, N., Linnen, R., Benn, D., Martins, T., and Cauzid, J.,2021. Analyses of Li-rich minerals using handheld LIBS tool. Data, **6**: 68.

Benn, D., Martins, T., and Linnen, R. 2022. Fractionation and enrichment patterns in white mica from Li pegmatites of the Wekusko Lake pegmatite field, Manitoba, Canada. The Canadian Mineralogist, *Under review.*